A NEW MULTISCALE APPROACH FOR DYNAMIC MODELING AND SIMULATION OF MICRO-NANO BIOMOLECULAR SYSTEMS CHARACTERIZED BY A LOW REYNOLDS NUMBER

by

MAHDI HAGHSHENAS-JARYANI

Presented to the Faculty of the Graduate School of
The University of Texas at Arlington in Partial Fulfillment
of the Requirements
for the Degree of

DOCTOR OF PHILOSOPHY

THE UNIVERSITY OF TEXAS AT ARLINGTON

May 2014

Copyright © by MAHDI HAGHSHENAS-JARYANI 2014

All Rights Reserved

To Ghazaleh, and my parents.

Acknowledgements

I would like to thank my advisor Dr. Alan Bowling for giving me this opportunity to join his group, and also his invaluable advice during the course of my doctoral studies. I wish to thank my dissertation committee members, Dr. Ashfaq Adnan, Dr. Dereje Agonafer, Dr. Daejong Kim, and Dr. Hyejin Moon for their interest in my research and their valuable time to serve in the committee.

I would also like to extend my appreciation to Dr. Samarendra Mohanty and his doctoral student Bryan Black for providing the experimental results in chapter 2. Thanks to Dr. Daniel Flickinger, my former colleague, for his technical advice about using scientific softwares, Linux, and server in our lab, which help me a lot during my research.

I am especially grateful to my parents, Nasrin and Parviz, and my brothers, Alireza, Hamid and Mohammad Hussein, for constantly motivating, encouraging, and supporting me in all my endeavours.

Finally, I would like to express my deepest gratitude to my wife, Ghazaleh, for her sacrifice, encouragement, patience, and support during the past five years.

April 14, 2014

Abstract

A NEW MULTISCALE APPROACH FOR DYNAMIC MODELING AND SIMULATION OF MICRO-NANO BIOMOLECULAR SYSTEMS CHARACTERIZED BY A LOW REYNOLDS NUMBER

MAHDI HAGHSHENAS-JARYANI, Ph.D.

The University of Texas at Arlington, 2014

Supervising Professor: Alan P. Bowling

In this dissertation, a new multiscale computational framework was developed in order to model and simulate motility of micro-nano-sized objects in fluid environments, characterized with a low Reynolds number. Especially, it has been used for studying the dynamic behavior of biomolecular systems such as motor proteins inside cells.

Long simulation run time is one of the most important issues in modeling of cellular and biomolecular systems at the nanoscale due to the multiple time and length scales involved in the dynamics of these systems. These multiscale features are caused by either structure-structure (e.g. flexibility in biological structure or contact) or structure-fluid interactions (e.g. biological structure and surrounding fluid environment) which appear as disproportionality between physical parameters involved in their dynamics. In order to address this issue, the mostly used models, based on the famous overdamped Langevin equation, omit inertial properties in the equations of motion; that leads to a first order model which is inconsistent with the

Newton's second law. However, a new dynamic multiscale approach was proposed that uses the concept of the method of multiple scales (MMS) and brings all terms of the equations of motion into proportion with each other that helps to retain the inertia terms. This holds consistency of the model with the governing physical laws, Newton's second law, and experimental observations. In addition, numerical integration's step-size can be increased from commonly used sub-femto seconds to sub-milli seconds. Therefore, simulation run time is reduced significantly in compared with other approaches.

The proposed approach was examined in different cases including the dynamics of small objects (microbeads) in an optical trapping process, and locomotion of motor proteins likes myosin V and kinesin-1 in cells. The experimental observations, obtained from the study of trapped small beads in optical tweezers, verify the new multiscale model and show the proposed model can correctly predict the physical characteristics at the nanoscale. In addition, the simulation run-time using the proposed multiscale models was significantly reduced in compared with the original and the first order models. Then, the multiscale model was used for modeling and simulation of motor proteins. The simulation results obtained by the proposed multiscale model show a dynamic behavior of myosin V and kinesin which is more consistent with experimental observations in compared with other overdamped models.

In this dissertation, a new online constraint embedding method was invoked in order to facilitate numerical simulation of motor proteins mechanical model, as a multibody system, with on-fly constraints including, 1) holonomic constraints due to use of Euler parameters for describing configuration of proteins and 2) non-holonomic constraints because of contact-impact between proteins and the substrates.

Table of Contents

List of Illustrations

List of Tables

Chapter 1

Introduction

1.1 Multiscale Analysis at the Micro-Nano Scales

This dissertation presents a new multiscale approach for modeling, analysis, and simulation of physical and biological phenomena at the micro-nano scale [1–10]. Development of nanotechnology during the recent decades led to a new challenge for invention of nanosystems with the capabilities of sensing, controlling, and actuating. In addition, based on recent progress in diverse scientific fields such as molecular biology, biophysics, and nanofabrication, the idea of using biological machines for building hybrid nanoscale organic/inorganic devices has been considered [11–14]. One of the interesting biological phenomena at small scales, which has been studied extensively in this work, is the locomotion and functionality of special proteins inside cells called motor proteins. Processive motor proteins such as myosin, kinesin and dynein are nanoscale proteins that "walk" unidirectionally along the cytoskeletons (actins and microtubules), similar to a biped, transporting intracellular cargoes around the cell, participating in cell division, cell migration, and muscles contraction [15]. Their locomotion are fueled by conversion of chemical energy of Adenosine triphosphate (ATP)-hydrolysis into mechanical work. Experimental and theoretical studies have shown interesting characteristics of these biological machines, including robustness, parallel working, nanoscale size, high energy efficiency and their potentially cheap applications [11]. Therefore, several applications of motor proteins in nanotechnology, such as transportation, sorting, self-assembly, and detection, have been suggested [11–14, 16–33].

Despite several experimental studies on motor proteins using different single-molecule techniques with high temporal and spatial resolutions [34–37], these experimental measurements and observations can not visualize the detailed motion and dynamic behaviors of motor proteins [38]. Theoretical models have been developed to cover the gap of experimental studies in this field [1–6, 8, 9, 39–44]. Theoretical modeling and computer-aided simulation of biological systems are essential for understanding and prediction of all processes in living organisms and designing new technologies in biomedical fields. Most of interested biological phenomena take place in different length and time scales ranging from atomistic (*nm,ns*) to macroscopic (*mm,ms*) [5,6,8–10]. Multiscale features of physical and biological phenomena caused by: 1) *different structural length scales of these phenomena* and 2) *external interactions of these systems with environment*. Thus, several computational and analytical multiscale approaches have been developed for modeling and simulation of biological and bionic systems [45–47]. Widely used methods are based on molecular dynamics (MD) which model these systems in atomistic resolution [48, 49]. However, considering all atoms reactions and sub-femto seconds integration step size make these methods non-efficient in time and computational cost. Also, simulation time rarely can be beyond microseconds while most of biological phenomena occur in milliseconds [45]. In addition, many important biological and bionic systems are too large to be simulated using MD. Therefore, hybrid molecular and continuum modeling methods, which span sub-nanoscopic to macroscopic time and length scales, have been developed over the past two decades. However, concurrent methods such as MAAD (Macroscopic, Atomistic, Ab initio Dynamics) [50], CGMD (Coarse-Grained Molecular Dynamics) [51, 52], QC (Quasi-Continuum) [53], and Bridging Domain [54], just consider effect of multiscale characteristics caused by connections between different length scales for modeling internal interactions, strain and stress, of structures.

Still, the disproportionality between inertial and viscous forces, yields a multiple time scale model. Thus, development of an approach, that can handle coupling of phenomena from atomistic to macroscopic temporal/spatial domains, is still a fundamental challenge [45,46,48,55]. In order to address this issue, several approaches isolate the dynamics of the larger time scales, resulting in a model that retains only low frequency modes, [56], uses only low order perturbations [57–59], or omits the mass-acceleration terms altogether [41, 42, 60]. In particular, omitting the mass yields a reduced order model, described by the well-known over damped Langevin and Fokker-Planck equations. Table 1.1 shows the list of references that use the massless and the proposed massive models for describing locomotion of motor proteins.

Table 1.1. Massless and Massive Mechanical Models.

model	equation	references
massless	$\mathbf{0} = (\mathbf{F} - \beta\dot{\mathbf{x}})$	[39, 41–43, 61–83] [40, 44, 60, 84–109] [47, 110–128]
massive	$m\ddot{\mathbf{x}} = a_2\,(\mathbf{F} - \beta\dot{\mathbf{x}})$	[1–10]

This work presents a new multiscale dynamic modeling approach that considers external interactions, structure-structure (contact and impact) or fluid-structure (viscosity), between molecular motors and surrounding environment at different scales, in contrast to other approaches that do not [47, 55]. These interactions occur during a number of biological phenomena including viral infections, immune response, cell membrane ingress and egress, and hormone and chemical signaling. The new concept is based on the trade off between the order of magnitude of external active forces, such as viscous forces, with the relevance of mass properties at different length scales. Particularly, small viscous forces at nanoscale leads to retaining mass in the equations

of motion describing motion at the nanoscale [1–10]. However, widely-used models ignore the mass properties of motor proteins and just consider force-velocity relationship [41, 42, 95, 120]. The proposed approach brings all terms of equations of motion in proportion with each other that helps to increase time step size of numerical integration from commonly used sub-femto seconds to sub-milli seconds. Simulation run time will be order of magnitude less than ones based on the other approaches.

One of the key aspect of this work is that many of the insights discussed above apply to the particle model developed in chapter 2. The theory presented there applies to sole nanoscale particles and predicts the nanoviscosity experimentally examined for nano-sized particles in [129, 130]. Others have noticed a transition zone for particles in low Reynolds number flow between the micro and nano scale where the idea of a continuum fluid breaks down and the more discrete forces associated with Brownian motion become more prominent [131, 132], although not dominant. This is also predicted by the second order particle model proposed in section 2.3.

Although the focus of this dissertation is on mechanical modeling of the macromolecular motors, there is a general benefit in understanding the multiscale dynamics of molecular and nanoscale systems and the proposed theory can also be applied to analysis of the dynamics of nano-sized particles in varied applications. Many of the features present in the proposed model exist in other molecular systems. The reduction in run time using the new model allows theoretical exploration of a large number of biological phenomena. These include the interactions between different types of molecules including ligands, receptors, hormones, antibodies, enzymes, viruses, neurotransmitters and other molecular structures. Beyond cellular simulation, there are several medical devices which involve multiscale phenomena in a fluid environment, including lab-on-a-chip applications. Some of these devices include functionalized nanopores lined with ligands and other protein receptors that bind with other

molecules whose function can be simulated and investigated using the new model. The proposed approach has a broad set of possible applications that make its study worthwhile.

1.2 Microbead in Optical Tweezers

However the motor proteins models were intended to examine the proposed multiscale approach for modeling motion of small scale systems in fluid environments characterized by a low Reynolds number but because of the difficulties involved in obtaining the experimental evidences, a simpler case-study, motion of micro-nano beads under influence of optical tweezers, has been considered for validation of the new theory [7,10]. Optical tweezers (OTs) use radiation pressure from a focused laser beam to manipulate microscopic objects as small as atoms [133]. This technique has been used for about 40 years in the physical sciences to study behaviors and physical properties of micron and submicron size particles [134]. Free-space as well as fiber-optic versions [135, 136] of OTs have been used in the biological sciences to cause nanometer-range displacements of, and to apply picoNewton-range forces to objects ranging from $10nm$ to over $100\mu m$. Optical forces have been used to measure the mechanical properties of DNA, cell membranes, whole cells [137], and microtubules; and much research has been conducted on motor proteins such as kinesin, dynein, myosin, and RNA polymerase using optical forces [138–146]. Therefore, the selection of this case-study for validation of the proposed approach is reasonable.

Most works in this field have studied the behavior of microbeads around the focal line of the optical trap to determine important properties including, the radial and axial trap strengths, spring constants, and force profiles [147]. However, the physical interaction of particles with their environment and its effect on their dynamic behavior during this trapping process at different length scales, micro and nano, have

not been adequately studied. This issue leads to inaccurate inferences about the dynamic behavior of particles, living cells, and proteins at the micro and nanoscales [1–3,5,6,8–10]. For example, overdamped behavior was observed for micrometer sized objects, and was extrapolated to predict that even smaller particles would behave similarly [148].

Novel experimental studies have been carried out by our collaborator, Prof. Samarendra Mohanty and his group, on a series of beads at different length scales using OTs [7, 10]. The results show an interesting transition from overdamped to underdamped motion of particles at the micro and submicron scales. These unconventional results call into question the widely accepted notion of overdamped motion of small particles in fluids characterized by a low Reynolds number and imply the relevance of inertial effects at the submicron scale. In other words, the mass properties should be retained in the equations of motion.

The observed underdamped behavior is confirmed using a planar dynamic model of a microsphere, under the influence of a Gaussian-beam OT. The beads' motions from an initial position to the trap's focal line are simulated. A multiscale modeling approach [1,2,5,6,8–10], based on a concept from the method of multiple scales [57], is used to generate a model that closely reproduces experimental observations of the microsphere's motion. Herein a ray-optics approach is used for modeling the optical forces of laser beams.

1.3 Theoretical Modeling of Motor Proteins

After verification of the approach using micro-nano beads in optical trapping process, now it can be implemented in the dynamic modeling of other similar scale systems like motor proteins. Motor proteins have been modeled in different ways in terms of their chemical kinetics, mechanics, and mechanochemical interactions.

Chemical kinetic models describe motor proteins as a set of chemical states that correspond to different positions along the filament upon which they walk [92, 120]. These models are stochastic and discrete and ignore the structural and mechanical aspects of motor proteins.

The combination of mechanics with the kinetics of ATP hydrolysis has been used to model motor proteins in mechanochemical models [43, 95, 119]. In contrast to the pure chemical kinetics, in mechanochemical models each chemical state is associated with a particular strain energy in the neck domains considered as elastic lever-arms [95, 119] or semiflexible partitioned rigid bodies [43]. These models allow simulation of the simultaneous effects of chemical reactions and strain energy on the protein's stepping.

This work considers a purely mechanical model of the motor protein which omits chemical kinetics. These models have several variations including atomistic, particle, molecular, and rigid body models. The most common modeling approach represents the protein using a small number of particles, oftentimes 2 or 4 [41, 60, 149] or a large network of particles, referred to as an elastic network model (ENM) [43,44,47,95,103]. The former cannot model all inter-particle interactions, while the latter addresses this issue by modeling all particles at atomistic level. However, ENM has three main disadvantages: 1) *huge computational efforts to determine all internal forces between particles*, 2) *spatial and temporal limitations of simulation*, and 3) *not desired for contact and impact analysis*. Many analytic methods have been developed which focus on reducing molecular system's degrees-of-freedom by grouping particles into rigid bodies, called coarse-graining. These models have been invoked to explore more complex, multiparticle interactions between the protein and the substrate upon which they walk [1–3, 38, 43, 51, 55, 56, 150–152], including contact and impact.

This research presents a 3D, coarse-grained, motor protein model which is an extension of the 2D model studied in [1,2]. Most of 3D coarse-grained models of motor proteins consider spatial position of rigid bodies in an elastic-network; however, 3D rotational properties of them are omitted or replaced by a simple rotation [38, 43, 153]. The proposed model is unique because it retains the mass properties usually omitted in most models. Comparisons between the 2D model in [2] and the 3D one examined here show significant differences in the effect of the random forces associated with Brownian motion on the movement of the protein. Brownian motion is less pronounced in the 3D model.

The proposed model uses Euler parameters to describe 3D rotations. Other 3D Euler parameter models have been proposed based on quaternion algebra in [154–156]. The proposed modeling and simulation approach does not depend on quaternion algebra, but uses a constraint-based algorithm to eliminate the extraneous coordinates. This is a new approach to simulating models involving Euler parameters that easily allows the inclusion of other conditions such as contact and impact, non-penetration constraints.

1.4 Flexibility in Motor Proteins

In the next step, the original idea introduced in [1–5] was extended into a new mechanical model for investigating flexibility in molecular motors, especially in myosin V. Experimental studies on myosin V have shown that its neck domain can be considered as three pairs of tandem elements called IQ motifs which can bend at junctures between them [157, 158]. This fact, the flexibility of myosin V, has been considered in few theoretical works such as [43, 95, 119]. Craig and Henke [43] have used three semi-flexible segments with ability of bending and stretching for modeling flexibility in neck domain. The neck domain of myosin V has been

modeled as six stretchable segments with only bending between the whole neck and the head [95]. Vilfan [119] has modeled the neck of myosin V as an elastic lever beam (cylindrical rod). He shows that the stretching stiffness ($k_L = 230pN/nm$) is so larger than the equivalent bending stiffness ($k_b = 0.25pN/nm$); therefore, the longitudinal extensibility is negligible. Notice that all of the mentioned theoretical works have used overdamped Langevin equation that omits the inertial properties of the myosin V's model. The persistence length, l_p of myosin V's neck domain varies over a wide range ($100nm \leq l_p \leq 400nm$) in literatures [43]. This means the elastic stiffness ($k \sim 2l_p k_B T/L$ where k_B, T, and L are Boltzmann constant, temperature, and the length of each neck's segment, respectively) is in the range of ($4 \times 10^{13} ag.nm^2/(ms^2.rad) \leq k \leq 4 \times 10^{14} ag.nm^2/(ms^2.rad)$) which is orders of magnitude larger than the viscous damping coefficient ($\beta = 10^8 ag/ms$) and mass of myosin V ($m_{tot} = 0.48ag$). Thus, adding flexible elements to the mechanical model of molecular motors, myosin V, creates an extra disproportionality between terms in the equations of motion which cannot be handled by the original multiscale approach.

This dissertation proposes a modification to the original multiscale dynamic modeling approach that addresses this issue. The approach was initially examined by using a planar model of myosin V [6]. Then, in order to obtain more realistic behavior of myosin V, a 3D finite segment model was developed [8, 9]. The deformable neck domain is modeled by three rigid bodies connected by flexible spherical joints (i.e. spherical joints and torsional springs) together, rather than a single rigid body used in the previous works [1–5]. The modified multiscale approach has an extra scaling factor, in compared with the original approach, that brings all generalized active forces, with different orders of magnitude, into proportion with inertial terms. Thus, the speed of simulation of flexible myosin V will be increased drastically. The resulting

motion predicted by the model of myosin V is more realistic in compared with other models.

1.5 Numerical Simulation

After developing and verifying the proposed multiscale approach, now it is the time to implement the theoretical approach in a numerical simulation in order to model the locomotion and dynamic behaviors of motor proteins. Herein, the equations of motion, represented as a second order differential equation, was expressed as a system of first order differential equations in order to integrate them. Nominally at each time step, the derivative of generalized coordinates and speeds are calculated and used to increment the current coordinates yielding the new coordinates for the next time step. This calculation must be modified here to enforce the constraints involved in the dynamic modeling of proteins. The constraints are including holonomic and no-holonomic due the use of Euler parameters and non-penetration-docking condition, respectively.

This dissertation presents a new computational strategy for handling holonomic and non-holonomic constraints involved in the dynamics of three dimensional (3D) rigid multibody systems. This work focuses on holonomic constraints due to use of Euler parameters and non-holonomic constraints because of contact and impact. Despite the fact that quaternions were introduced by Hamilton over a 100 years ago, they have just been practically used during the last three decades [154, 156, 159–163]. Quaternions have been used in spatial kinematic analysis, rigid body dynamics [154, 156], robot trajectory planning, control of aircraft and space craft [159, 161], and recently describing the configuration of molecules, protein structures, and bio-polymers [160]. Euler parameters are used to model the orientation of bodies in order to eliminate singularities in the description of orientation. In addition, a frictionless

contact and impact are considered during simulation of multibody systems that leads to on the fly non-holonomic constraints.

However, it is difficult to address the normality constraint of Euler parameters during numerical integration. This issue has been addressed in several ways, where the most frequently used techniques are the method of Lagrange multipliers [154,156, 162,164,165], projecting constraints [166], and symbolic constraint embedding [164, 165,167,168]. The first two methods are based on simultaneous solving equations of motion and algebraic constraints equations as differential algebraic equations (DAEs). The DAE solvers have issues with drifting and stabilization [169,170]. Therefore, an extra procedure, such as renormalization, is required for correcting the quaternions after integration [169–171].

Here, a numerical and online constraint embedding method is used to address these issues by reducing equations of motion to a minimal form [164, 165, 167] using constraints. Thus, the constraints are implicitly satisfied during the numerical integration, in contrast to the other approaches which do this explicitly. The constraint embedding procedure is based on the coordinate partitioning method which has been originally introduced by Wehage and Huag [164]. The success of this method depends on the choice of independent coordinates. Undesirable choice may lead to ill-conditioned matrices or singularities [165,169,170]. This issue has been addressed by partitioning coordinates into dependent and independent groups using the singular value decomposition (SVD) [169, 170, 172, 173], LU factorization [173], QR decomposition [169, 170, 174], and a projective criterion introduced by Blajer [165, 175]. Although using SVD, LU factorization and QR decomposition leads to the best conditioned dynamic equations but they are computationally inefficient [165]. The projective criterion has less computational cost and provides optimal partitioning that reduces the constraint violation [165, 175]. Based on the projective method [165],

coordinates which have larger projection along the tangent direction are chosen as the independent coordinates. However, the implementation of the method requires the inverse of the original (not reduced) mass matrix and the mass matrix obtained using Euler parameters is not invertible.

The proposed approach has a smaller computational cost than the SVD and the other decompositions, and does not require the mass matrix inverse. Here a partitioning of the generalized speeds is carried out in order to provide a nonsingular square submatrix of the constraint Jacobian matrix which relates the dependent speeds. This is a necessary condition for reduction of the equations of motion [165, 169, 170]. Three algorithms are explored to determine which creates the least error in the motion predicted by the simulation. The best of these can facilitate the use of the constraint embedding approach to address the extraneous coordinates in the Euler parameters in a dynamically consistent manner. Moreover, the splitting procedure for the non-holonomic constraints will be done by using the *qr decomposition* method. This method assures nonsingular partitioning of generalized coordinates, and consequently the contact Jacobian, into the dependent and independent groups in order to enforce non-holonomic constraints. The effectiveness of the proposed numerical constraint embedding and the different selection algorithms are examined on dynamic simulation of a 3D double pendulum with ball-and-socket joints. The results show ability of the proposed strategy to handle drifting and singularity issues involved in other approaches.

1.6 Overview

In chapter 2, a new multiscale particle dynamics is developed in order to model and simulate dynamic behavior of small objects (e.g. micro and nano sized beads) moving in an fluid environment often characterized by a low Reynolds number. The

proposed approach, in contrast to the well-known overdapmed Langevin model, provides new insights into physical characteristics of motion of particles at the nanoscale such as the relevance of inertia, underdapmed behaviors, and reduction of frictional forces. In addition, the simulation run-time is reduced significantly in compared with the conventional, and overdamped models. The model and simulation results are verified by experimental observations.

In chapter 3, the proposed multiscale approach is extended into a rigid multibody dynamic model for modeling and simulation of biomolecular systems, especially, locomotion and functionality of motor proteins inside cells. A new 3D coarse-grained mechanical model of myosin V, a type of motor proteins, is developed in order to show the differences in the dynamic behaviors predicted by the second order, massive, and first order, massless, models.

In chapter 4, the effect of flexibility involved in biological structure of motor proteins is studied. Adding flexibility into the dynamic model of these proteins creates an extra disproportionality which cannot be handled by the original multiscale approach, developed in chapters 2 and 3; therefore, a new multiscale approach is developed in order to address this issue; that brings generalized active forces with different orders of magnitude into the same order as generalized inertia forces. This helps to use larger integration step size which improves the speed of simulation.

In chapter 5, numerical simulation of the developed multiscale particle and rigid multibody models is discussed. A new online constraint embedding technique is developed in order to address holonomic and non-holonomic constraints involved in the dynamic modeling of motor proteins. The holonomic constraints are related to the use of Euler parameters for describing rotation of multibody systems. The non-holonomic constraints are due to contact and impact between the motor proteins

and cytoskeletons. The proposed technique requires low computational efforts and addresses the drifting and stabilizing issues involved in other approaches.

Chapter 2

New Multiscale Approach for Single Body Model

2.1 Introduction

This chapter introduces a new multiscale approach using particle dynamics for modeling physical phenomena at small scales commonly characterized by a low Reynolds number. The multiscale particle dynamics was presented for motion of a small size particle in a fluid environment without any flexible term in the equations of motion. However the developed multiscale particle approach can be applied to a particle model of motor proteins [1–5], approximated by a few particles, but because of difficulties in acquisition of experimental data for motor proteins, the new theory was implemented for a planar model of microbead under influence of optical tweezers (OTs) [7, 10]. The results were obtained for three different sizes of beads $500nm$, $990nm$, and $1950nm$. Then, the proposed approach were validated by comparison of theoretical results with the experimental observations [10].

OTs' simulations can be found on the Internet, such as [176] (a Java applet used for teaching purposes), [177] (a simple animation of a trapped bead), and [178] (an illustration of a DNA stretching experiment in the Rayleigh regime), and a few theoretical works such as [145]. These simulations model the system using a first-order differential equation, the overdamped Langevin equations, which ignore the mass and acceleration terms thereby implying overdamped motion. However, some issues arise when the mass is omitted concerning the violation of Newton's second law [1–10]. In this work, a multiscale modeling approach, following that derived

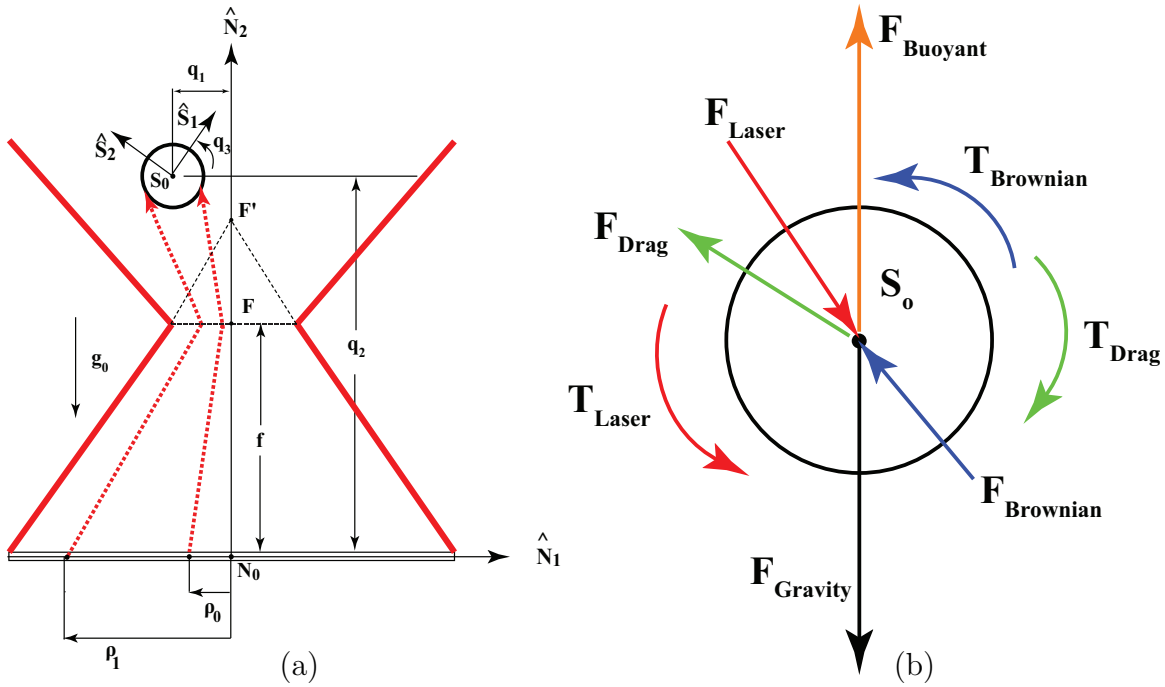

Figure 2.1. Overall model setup: (a) coordinates, points, and frames, (b) forces and moments on the bead. .

in [1–10], yields a second order model that retains the mass properties and thus can predict the experimentally observed underdamped motions.

2.2 Dynamic Model of Microbead

The simulations are based on a simple dynamic model of a planar bead in a fluid environment. The model was developed using Newton's Second Law and Euler's equations for rigid body dynamics. Figure 2.1a shows the general setup for the simulation model. The inertial reference point, N_o, is defined as the center of the objective lens. The inertial reference frame, defined by the unit vectors $\widehat{\mathbf{N}}_1$ and $\widehat{\mathbf{N}}_2$, is composed of a right-handed, orthogonal set of axes. The virtual point F′ indicates

the true point of convergence of the laser beam. The focal line is located at point $(0, f)$, with respect to the inertial reference frame:

$$f = \frac{n_g R_{obj}}{NA} \tag{2.1}$$

where n_g, R_{obj}, and NA are the index of refraction of glass, the radius of objective lens, and the numerical aperture of objective lens, respectively. The microparticle is defined as a body, S, with a center of mass, S_o, and a body-attached frame, frame $\mathbf{S}$. The generalized coordinates and speeds are defined as $\mathbf{q} = \{q_1, q_2, q_3\}$, and $\dot{\mathbf{q}} = \{\dot{q}_1, \dot{q}_2, \dot{q}_3\}$, respectively. The dashed red (gray) line in Fig. 2.1 shows a sample of the laser beam, originating at distance ρ from N_o, that intersects the bead.

The translational motion is defined by

$$\sum \mathbf{F} \;=\; m\,\ddot{\mathbf{x}} \;=\; m \begin{bmatrix} \ddot{q}_1 \\ \\ \ddot{q}_2 \end{bmatrix} \tag{2.2}$$

where m is the total mass of the system, the vector $\ddot{\mathbf{x}}$ is the translational acceleration of the mass center, and the coordinates q_1 and q_2 are defined in Fig. 2.1a. The translational active forces are:

$$\sum \mathbf{F} \;=\; \mathbf{F}_g + \mathbf{F}_{drag} + \mathbf{F}_{buoy} + \mathbf{F}_{laser} + \mathbf{F}_{Brownian} \tag{2.3}$$

where $\mathbf{F}_g$, $\mathbf{F}_{drag}$, $\mathbf{F}_{buoy}$, $\mathbf{F}_{laser}$, and $\mathbf{F}_{Brownian}$ are gravity, viscous drag, buoyancy, optical, and random thermal forces, respectively. These forces are depicted in Fig. 2.1b and discussed in sections A.2 and A.3.

Euler's equation describes rotational motion as,

$$\sum M \;=\; I_{33}\,\ddot{q}_3 \tag{2.4}$$

where I_{33} is the moment of inertia of the bead about the $\widehat{\mathbf{N}}_3 = \widehat{\mathbf{N}}_1 \times \widehat{\mathbf{N}}_2$ direction, and $\ddot{q}_3$ is the angular acceleration of the bead corresponding to the q_3 coordinate shown in Fig. 2.1a. The sum of moments acting on the bead is defined as

$$\sum M = T_{laser} + T_{drag} + T_{Brownian} \tag{2.5}$$

where T_{laser}, T_{drag} based on [179], and $T_{Brownian}$ are beam, viscous drag, and random thermal moments, respectively. These moments are depicted in Fig. 2.1b and explicitly defined in section A.3.

The combined system model can be expressed as

$$\begin{bmatrix} m & 0 & 0 \\ 0 & m & 0 \\ 0 & 0 & I_{33} \end{bmatrix} \begin{bmatrix} \ddot{q}_1 \\ \ddot{q}_2 \\ \ddot{q}_3 \end{bmatrix} = A\ \ddot{\mathbf{q}} = \begin{bmatrix} \sum \mathbf{F} \\ \sum M \end{bmatrix} \tag{2.6}$$

where A is the mass matrix. The terms on the left-hand-side of (2.6) depend on mass and thus are referred to as *generalized inertia forces*. The forces on the right-hand-side of (2.6), are called *generalized active forces*.

2.3 Multiscale Particle Dynamics

A key issue with the physical model of small objects like micro-nano beads, presented in (2.6), is that a very small body moves through a fluid environment yielding a situation which is characterized by a small Reynolds number, (e.g. $10^{-9} \leq Re \leq 10^{-4}$ for a $500nm$ diameter bead), depending on the velocity. This number describes the relative importance of inertia versus drag forces. A small Reynolds number should indicate that the inertia forces have minimal impact on the bead's motion. This implies that the inertia forces can be omitted from the model, as several simulations have done [177]. However, recent work has suggested that this approach may violate Newton's second law, and offers an alternative modeling approach that

retains the inertia forces [1–10]. Herein it will be shown that this new model closely predicts the bead's behavior.

In order to investigate this model it is necessary to examine the relationship between the generalized inertia forces and viscous drag forces and moments:

$$m\ddot{\mathbf{x}} = \mathbf{F} - \beta_v \dot{\mathbf{x}} \tag{2.7}$$

$$I_{33}\ddot{q}_3 = M - \beta_\omega \dot{q}_3 \tag{2.8}$$

where $\mathbf{F}$ and M contain all forces and moments other than those related to viscous drag. The inertia properties for the $500nm$ bead used herein are $m = 0.0687pg$ and $I_{33} = 0.00173 \times 10^{-6} pg \cdot mm^2$. In order to determine the viscous drag properties it is necessary to consider the characteristics of the fluid.

This can be accomplished using the Knudsen number, Kn, which indicates whether the fluid must be considered as a continuum, or as discrete, individual molecules. It is the ratio of the fluid mean free path and the characteristic length of system. For the $500nm$ bead in water, the mean free path is, $\lambda_{mfp} = 0.3nm$, and therefore $Kn = 0.0006$. Since the Knudsen number is less than 0.001 the fluid is considered as a continuum. Thus, it should be reasonable to use Stoke's Law to calculate drag coefficients. However, because the bead is small, it is unclear how its surface interacts with the surrounding fluid to create drag. This is referred to as the *no-slip boundary condition*, which indicates whether the fluid sticks to the bead's surface creating larger drag forces, or slipping occurs between the fluid and the bead, creating less drag. This phenomena has been verified experimentally and theoretically [180]. This condition can be checked by calculating a slip correction factor [180], here $C_c = 1/(1 + 2.52Kn) = 0.99995$, that multiplies the drag coefficients; this correction is negligible and thus is not used.

Based on these arguments the translational drag coefficient in (2.7) is obtained using Stokes' Law as $\beta_v = 4.722 \times 10^3 pg/ms$. The rotational drag coefficient in (2.8) is obtained from an analysis of rotational diffusion [179] yielding $\beta_\omega = 8\pi\mu_m r_S^3 = 3.935 \times 10^{-4} pg \cdot mm^2/ms$ where μ_m is the viscosity of the fluid medium and r_S is the radius of the bead. Dividing through (2.7) and (2.8) by the drag coefficients yields

$$(1.46 \times 10^{-5} ms)\ \ddot{\mathbf{x}} \ = \ \frac{m}{\beta_v}\ \ddot{\mathbf{x}} \ = \ \frac{\mathbf{F}}{\beta_v} - \dot{\mathbf{x}} \tag{2.9}$$

$$(0.44 \times 10^{-5} ms)\ \ddot{q}_3 \ = \ \frac{I_{33}}{\beta_\omega}\ \ddot{q}_3 \ = \ \frac{M}{\beta_\omega} - \dot{q}_3 \tag{2.10}$$

The disproportionality between the mass and the viscous drag coefficients, $O(10^{-5})$, creates large accelerations that require a small time step, yielding a long numerical integration time.

In order to reduce the run time, it has been suggested that the small coefficient of the acceleration terms in (2.9) and (2.10) implies that these terms can be omitted, yielding a first order model. A second approach uses the multiscale analysis, discussed in [1–10], that begins by determining a characteristically small number from the model in (2.9) and (2.10), $m/\beta_v \approx 1.46 \times 10^{-5}\ ms$. Using this in (2.7) and (2.8) yields,

$$\begin{aligned} \mathbf{0} \ &= \ \varepsilon\ (1ms)\ddot{\mathbf{x}} - \frac{\mathbf{F}}{\beta_v} + \dot{\mathbf{x}} \ = \ \varepsilon\ddot{\mathbf{x}} - \frac{\mathbf{F}}{\beta_\mathbf{v}} + \dot{\mathbf{x}} \\ 0 \ &= \ \varepsilon\ (0.3ms)\ddot{q}_3 - \frac{M}{\beta_\omega} + \dot{q}_3 \ = \ \varepsilon\ddot{q}_3 - \frac{M}{\beta_\omega} + \dot{q}_3 \end{aligned} \tag{2.11}$$

such that $\varepsilon = 1.46 \times 10^{-5}$ is unitless. The small parameter ε is used to decompose time into different scales: $T_i = \varepsilon^i t$. This yields

$$\begin{cases} \dot{\mathbf{x}} = \dfrac{d\mathbf{x}}{dt} = \varepsilon^0 \dfrac{\partial \mathbf{x}}{\partial T_0} + \varepsilon^1 \dfrac{\partial \mathbf{x}}{\partial T_1} + \varepsilon^2 \dfrac{\partial \mathbf{x}}{\partial T_2} + \cdots \\ \\ \dot{q}_3 = \dfrac{dq_3}{dt} = \varepsilon^0 \dfrac{\partial q_3}{\partial T_0} + \varepsilon^1 \dfrac{\partial q_3}{\partial T_1} + \varepsilon^2 \dfrac{\partial q_3}{\partial T_2} + \cdots \end{cases} \tag{2.12}$$

$$\begin{cases} \ddot{\bar{\mathbf{x}}} = \dfrac{d^2\bar{\mathbf{x}}}{dt^2} = \displaystyle\sum_{i=0}^{\infty}\sum_{j=0}^{\infty} \varepsilon^i \varepsilon^j \frac{\partial^2 \bar{\mathbf{x}}}{\partial T_i \partial T_j} \\ \\ \ddot{\bar{q}}_3 = \dfrac{d^2\bar{q}_3}{dt^2} = \displaystyle\sum_{i=0}^{\infty}\sum_{j=0}^{\infty} \varepsilon^i \varepsilon^j \frac{\partial^2 \bar{q}_3}{\partial T_i \partial T_j} \end{cases} \tag{2.13}$$

When (2.12) and (2.13) are substituted into (2.11), and the terms are arranged in order of increasing power of ε, (2.11) becomes:

$$\begin{aligned} \mathbf{0} &= \varepsilon^0 \left(-\frac{\mathbf{F}}{\beta_v} + \frac{\partial \mathbf{x}}{\partial T_0} \right) + \varepsilon^1 \left(\frac{\partial^2 \bar{\mathbf{x}}}{\partial T_0^2} + \frac{\partial \mathbf{x}}{\partial T_1} \right) + \cdots \\ 0 &= \varepsilon^0 \left(-\frac{M}{\beta_\omega} + \frac{\partial q_3}{\partial T_0} \right) + \varepsilon^1 \left(\frac{\partial^2 \bar{q}_3}{\partial T_0^2} + \frac{\partial q_3}{\partial T_1} \right) + \cdots \end{aligned} \tag{2.14}$$

The difference between $\varepsilon^0 = 1$ and $\varepsilon^1 = 1.46 \times 10^{-5}$ is fairly large, so it is likely that the generalized active forces in (2.11) must cancel to some extent in order for the sum in (2.14) to equal zero. From a multibody dynamics standpoint, if a system of forces cancel then they produce no motion and can be omitted from the equations of motion. *The effort here is to remove these canceled forces from the model.*

Here this is accomplished by decomposing the generalized active forces into large and small parts,

$$\begin{aligned} -\frac{\mathbf{F}}{\beta_v} + \frac{\partial \mathbf{x}}{\partial T_0} &= (a_1 + a_2) \left(-\frac{\mathbf{F}}{\beta_v} + \frac{\partial \mathbf{x}}{\partial T_0} \right) \\ -\frac{M}{\beta_\omega} + \frac{\partial q_3}{\partial T_0} &= (a_1 + a_2) \left(-\frac{M}{\beta_\omega} + \frac{\partial q_3}{\partial T_0} \right) \end{aligned} \tag{2.15}$$

where $a_1 + a_2 = 1$ and $a_1 \gg a_2$. Substituting (2.15) back into (2.14) yields

$$\begin{aligned} \mathbf{0} &= a_1 \left(-\frac{\mathbf{F}}{\beta_v} + \frac{\partial \mathbf{x}}{\partial T_0} \right) + a_2 \left(-\frac{\mathbf{F}}{\beta_v} + \frac{\partial \mathbf{x}}{\partial T_0} \right) + \varepsilon^1 \left(\frac{\partial^2 \bar{\mathbf{x}}}{\partial T_0^2} + \frac{\partial \mathbf{x}}{\partial T_1} \right) + \cdots \\ 0 &= a_1 \left(-\frac{M}{\beta_\omega} + \frac{\partial q_3}{\partial T_0} \right) + a_2 \left(-\frac{M}{\beta_\omega} + \frac{\partial q_3}{\partial T_0} \right) + \varepsilon^1 \left(\frac{\partial^2 \bar{q}_3}{\partial T_0^2} + \frac{\partial q_3}{\partial T_1} \right) + \cdots \end{aligned} \tag{2.16}$$

Here it is assumed that the large forces, defined as,

$$\mathbf{\Gamma} = \begin{bmatrix} \mathbf{\Gamma}_F \\ \Gamma_M \end{bmatrix} = \begin{bmatrix} a_1 \left(-\dfrac{\mathbf{F}}{\beta_v} + \dfrac{\partial \mathbf{x}}{\partial T_0} \right) \\ \\ a_1 \left(-\dfrac{M}{\beta_\omega} + \dfrac{\partial q_3}{\partial T_0} \right) \end{bmatrix} \tag{2.17}$$

cancel to the extent that they can be removed from (2.16), yielding a second order model of the form

$$\begin{aligned} \mathbf{0} &= a_2 \left(-\frac{\mathbf{F}}{\beta_v} + \frac{\partial \mathbf{x}}{\partial T_0} \right) + \varepsilon^1 \left(\frac{\partial^2 \bar{\mathbf{x}}}{\partial T_0^2} + \frac{\partial \mathbf{x}}{\partial T_1} \right) + \cdots \\ &= m\ddot{\mathbf{x}} + a_2 \ \beta_v \ \dot{\mathbf{x}} - a_2 \ \mathbf{F} \\ 0 &= a_2 \left(-\frac{M}{\beta_\omega} + \frac{\partial q_3}{\partial T_0} \right) + \varepsilon^1 \left(\frac{\partial^2 \bar{q}_3}{\partial T_0^2} + \frac{\partial q_3}{\partial T_1} \right) + \cdots \\ &= I_{33}\ddot{q}_3 + a_2 \ \beta_\omega \ \dot{q}_3 - a_2 \ M \end{aligned} \tag{2.18}$$

assuming $\dfrac{d\mathbf{x}}{dt} = \dfrac{\partial \mathbf{x}}{\partial T_0}$ and $\dfrac{dq_3}{dt} = \dfrac{\partial q_3}{\partial T_0}$.

The scaling factor a_2 is determined by matching the characteristics of the simulation with the experimental observations in section 2.4.1; typically $a_2 \geq \epsilon$. Since all of the terms in (2.18) will be in proportion, they can be numerically integrated in *drastically* less time. The results are used to check whether the forces in $\mathbf{F}$ sufficiently cancel, which provides a measure of the quality of (2.18) as a model of the system's dynamics. This check should produce $O(\Gamma_i) \leq O(a_2)$ so that one may conclude that the forces in $\mathbf{\Gamma}$ do not create significant motions beyond those produced by the a_2 scaled forces.

2.3.1 Simulation Results

In order to investigate the proposed approach, the different models for the $500nm$ bead were coded in the C programming language and numerically integrated using a high speed computer, a DELL PowerEdge 2900 III Server with two quad-core,

2.33 GHz processors, running the Ubuntu (Linux) operating system, using an *adaptive* Runge-Kutta 45 algorithm. Numerical integration of the Newton-Euler model in (2.7) and (2.8) yields the overdamped motion shown in Fig. 2.2, which took approximately $73hrs$, in order to obtain $100ms$ of simulation time; (at $40ms$ the laser is turned on.) In order to obtain any results it was necessary to reduce the tolerance of the simulation, `AbsTol`=10^{-6}, and `RelTol`=10^{-5}. The lengthy run time stems from a reduction in the time step by the adaptive integrator in order to obtain the requested accuracy. Investigation of the step size reductions showed that the numerical integrator was proceeding with a picosecond step size.

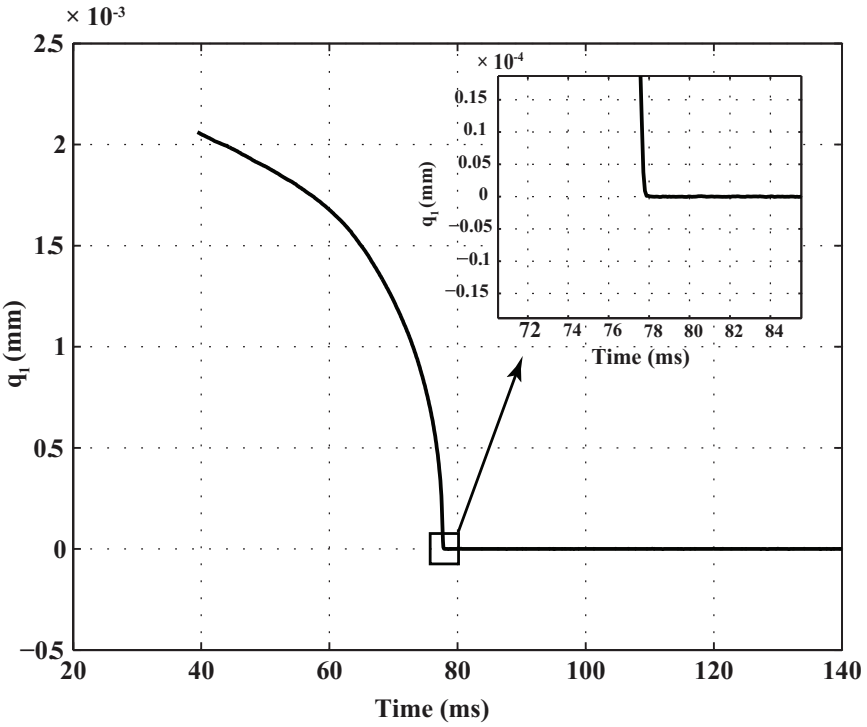

Figure 2.2. Simulation data for q_1 coordinate of microparticle using the Newton-Euler model (CPUtime $\approx 73hrs$, `AbsTol`=10^{-6}, `RelTol`=10^{-5}, $\Delta t = 0.001ms$) .

The first order model can be represented by (2.17) which yields the results shown in Fig. 2.3. The simulation run time is reduced to $45mins$, with an increased

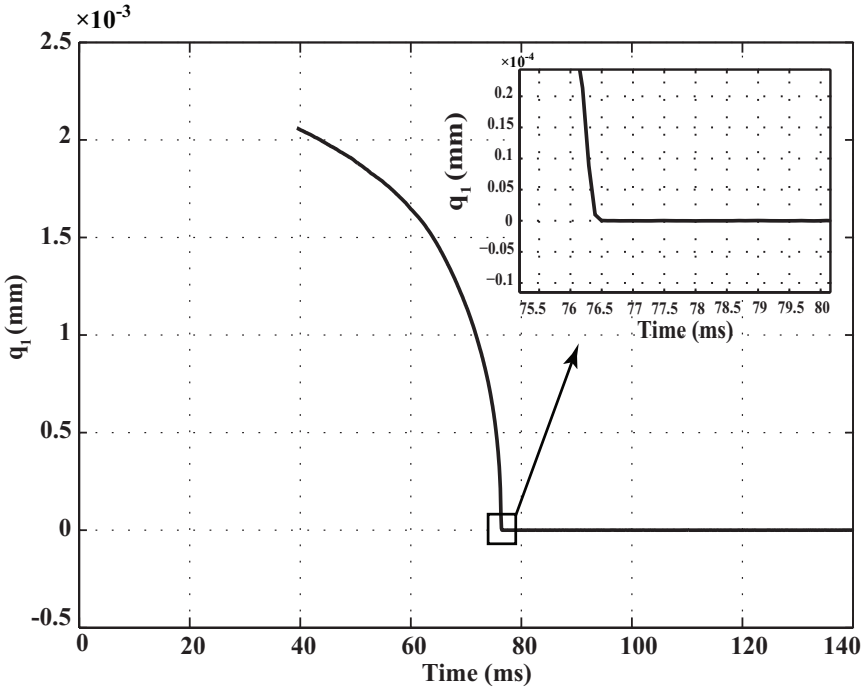

Figure 2.3. Simulation data for q_1 coordinate of microparticle using the first order model (CPUtime $\approx 45mins$, `AbsTol`=10^{-8}, `RelTol`=10^{-7}, $\Delta t = 0.001ms$) .

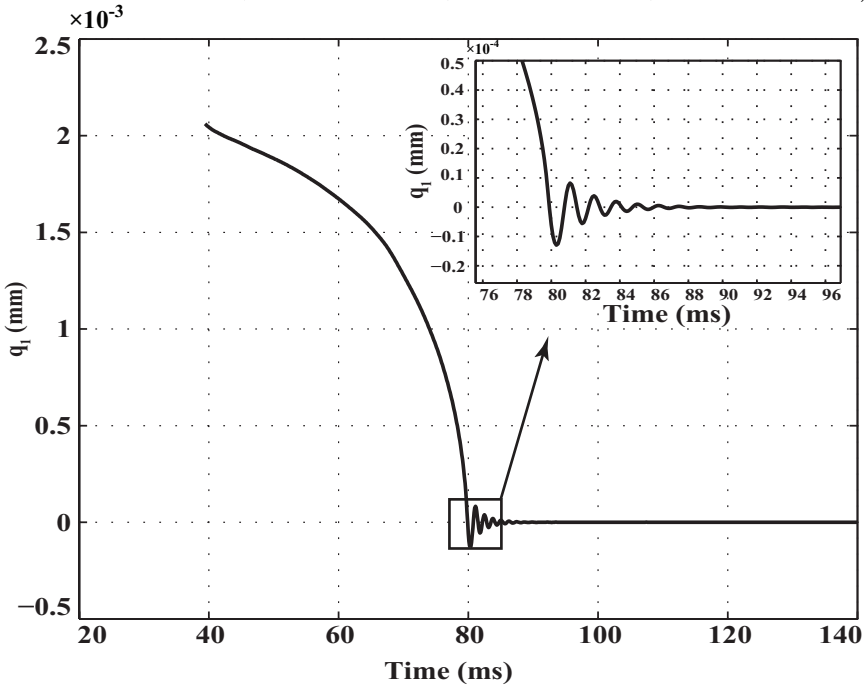

Figure 2.4. Simulation data for q_1 using the multiscale model (CPUtime=$21mins$, `AbsTol`=10^{-8}, `RelTol`=10^{-7}, $\Delta t = 0.001ms$) .

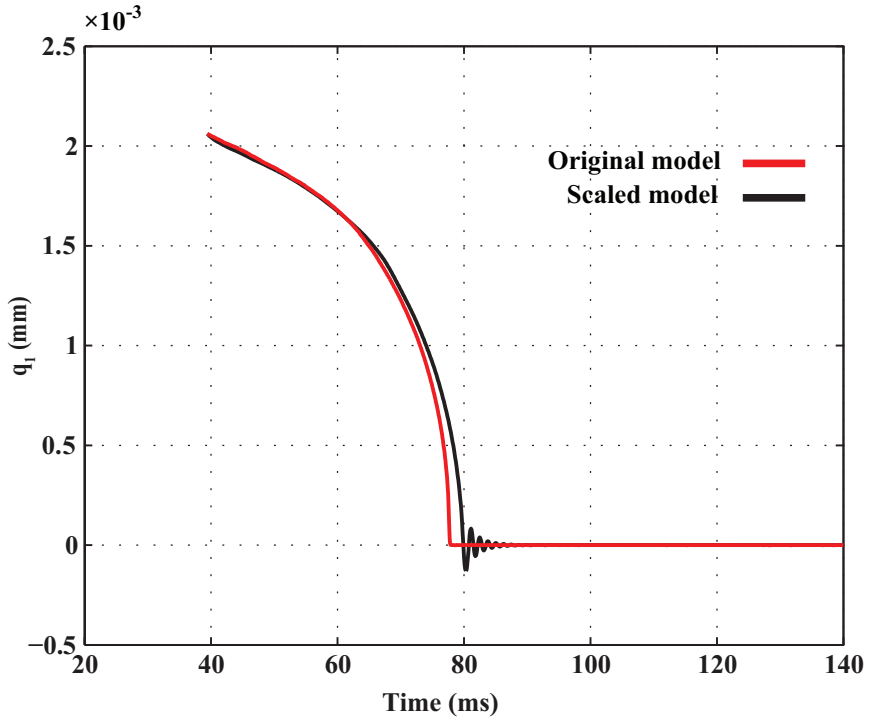

Figure 2.5. Overlap of simulation data for q_1 using the Newton-Euler model and the multiscale model .

tolerance `AbsTol`=10^{-8}, and `RelTol`=10^{-7}. Finally, the multiscale model in (4.13) is numerically integrated yielding the results in Fig. 2.4. The simulation run time is reduced to $21 mins$ using the same tolerance. A comparison of the results from the Newton-Euler approach and the multiscale approach are shown in Fig. 2.5.

The key thing to notice is the oscillations that appear in Fig. 2.4, when the bead reaches the focal line, that are absent from the simulation of the Newton Euler model in Fig. 2.2 and the first order model in Fig. 2.3. In addition, there is a significant reduction in the simulation run time of the multiscale model in compared with the original and the first order models, as presented in Table 2.2. The bulk of the simulation is spent resolving the situation when the bead reaches the focal line because of the alternating forces that occur as it overshoots the focal line. *The experimental*

Table 2.1. Physical Parameters Used in Simulation

			Bead Diameter (nm)		
	Definition	Units	1950	990	500
m	Mass	pg	4.08	0.533	0.0687
I_{33}	Moment of inertia	$pg \cdot mm^2$	1.5378×10^{-6}	5.2223×10^{-8}	1.73×10^{-9}
Kn	Knudsen number	-	1.54×10^{-4}	3×10^{-4}	6×10^{-4}
C_c	Stokes drag slip correction factor	-	0.99997	0.9992	0.99995
β_v	Translational drag coefficient	$\frac{pg}{ms}$	1.84×10^4	9.349×10^3	4.722×10^3
β_ω	Rotational drag coefficient	$\frac{pg \cdot mm^2}{ms}$	2.33×10^{-2}	3.054×10^{-3}	3.935×10^{-4}
a_2	Scaling factor	-	8×10^{-3}	2×10^{-4}	1.5×10^{-5}

Table 2.2. Comparison of Simulation Run-Time of Different Simulation Methods

	Bead Diameter (nm)		
Quantity	1950	990	500
Simulation time (ms)	140	140	140
Simulation run time (min)	4320	45	21

data in section 2.4.1 imply that the multiscale model represents the actual physical behavior of the $500nm$ *bead observed under the microscope.*

2.4 Experimental Verification

In order to verify the proposed multiscale approach, the bead's motion is investigated using an OTs experiment for the three different sizes of bead. These experiments observed the oscillations predicted by the multiscale model. The set up for these experiments is discussed in appendix A.

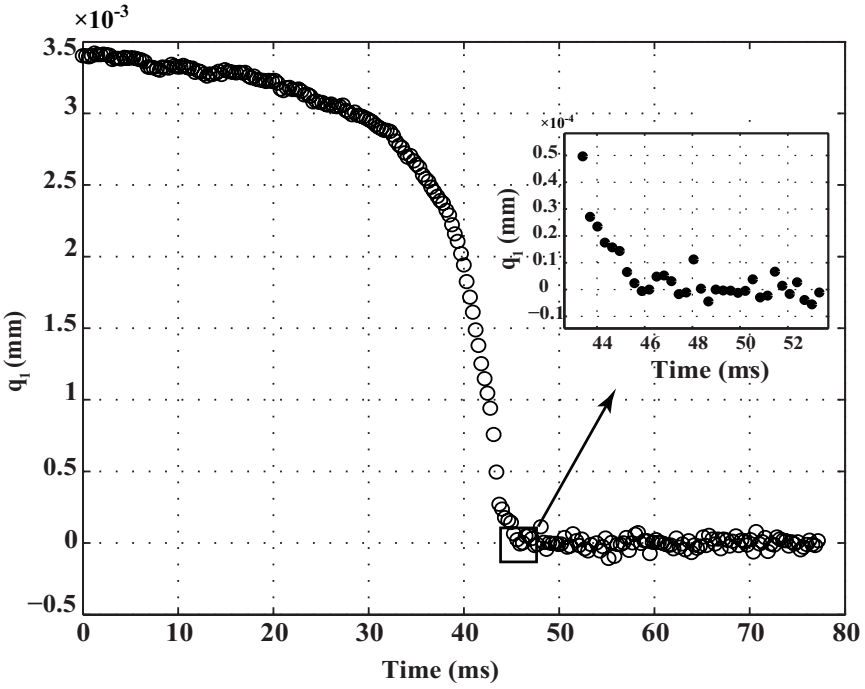

Figure 2.6. Experimental data for the motion of $1950nm$ microparticle in the horizontal direction. The data was captured at 2134 frames per second using OTs with $149mW$ power. The result is generated by Bryan Black in department of physics.

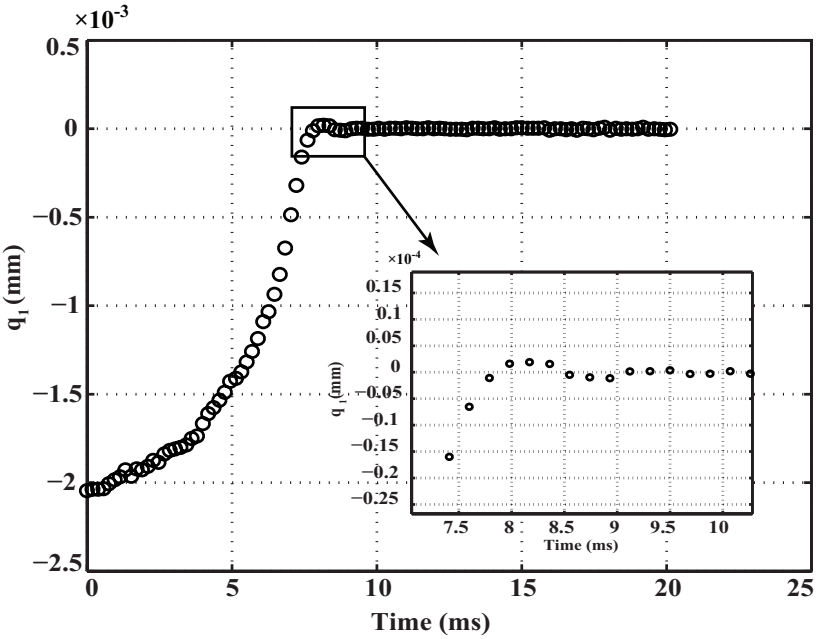

Figure 2.7. Experimental data for the motion of $990nm$ microparticle in the horizontal direction. The data was captured at 5132 frames per second using OTs with $156mW$ power. The result is generated by Bryan Black in department of physics .

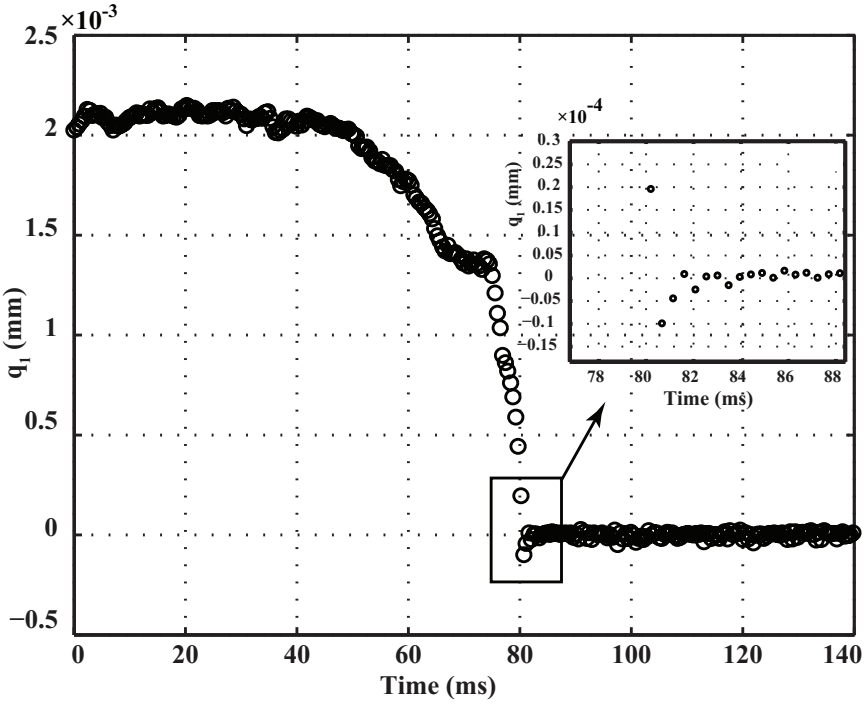

Figure 2.8. Experimental data for the motion of $500nm$ microparticle in the horizontal direction. The data was captured at 3214 frames per second using OTs with $156mW$ power. The result is generated by Bryan Black in department of physics .

2.4.1 Experimental Results

In order to examine the effect of size in the dynamic behavior of objects in a trapping process, three beads with different diameters, $500nm$, $990nm$, $1950nm$ were used. Three experiments were carried out for each bead size for the reported laser/optical parameters, yielding a total of nine experiments. This investigation begins by considering the largest diameter bead, $1950nm$, in Fig. 2.6. The circles mark the experimental results which show the overdamped behavior of microbead in response to the laser and viscous friction forces. This behavior has been observed for micrometer sized objects and was extrapolated to predict that even smaller particles would exhibit overdamped behavior [148].

The underdamped behavior, oscillations, begin to show for the $990nm$ diameter bead in Fig. 2.7. The bead overshoots the focal line and oscillates a small amount

before settling. The smallest bead $500nm$ bead, discussed in section 2.3, shows a much larger overshoot of the focal line with larger oscillations in Fig. 2.8. These observations are corroborated using a new approach to multiscale modeling discussed in section 2.3.

2.4.2 Comparison of Experimental and Simulation Results

The results obtained from the experimental and theoretical studies on three different sizes of microbeads are compared in Figs. 2.9 through 2.13. The largest bead, $1950nm$, displays the overdamped behavior predicted by the first order model. The simulation data shows that the multiscale model can predict this overdamped behavior with an appropriate choice of the scaling factor; the data for each of the simulations in Figs. 2.9 through 2.13 is given in Table 2.1. Figures 2.10, 2.12,and 2.14 show the transient motion of $1950nm$, $990nm$, and $500nm$ beads from the initial to the final positions, the trap point, in a 2D plane.

This overdamped behavior becomes underdamped in the experimental results of the smaller beads. The $990nm$ bead overshoots the focal line and oscillates a small amount before settling. The simulation result, solid line, shows that tuning of the scaling parameter, a_2, allows the multiscale model to predict the small oscillations that cannot be predicted by the first order model. The smallest bead $500nm$ bead, discussed in section 2.3, shows a much larger overshoot of the focal line with larger oscillations; see Fig. 2.13. *The successively smaller beads show the increasingly more oscillatory behavior predicted by the proposed multiscale model.* Note that recent ray-optics simulations of non-spherical, micro-sized objects predict underdamped behavior of a cubic object [181].

Thus, there is a general agreement between the experimental and computational results, which proves the presence of a transition in the dynamic behavior of

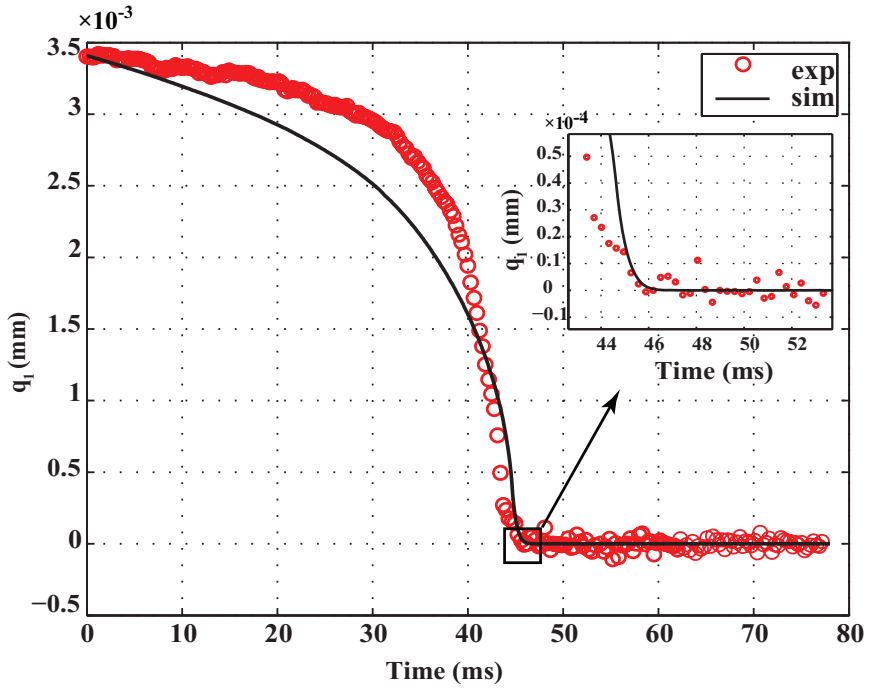

Figure 2.9. Comparison of experimental data (open circles) and simulation data (line) for q_1 coordinate of $1950nm$ microparticle using the multiscale model (CPUtime=$13mins$, `AbsTol`=10^{-8}, `RelTol`=10^{-7}, $\Delta t = 0.001ms$). The experimental result is generated by Bryan Black in department of physics.

objects under a trapping process at different length scales. However, the simulation results, especially for the $990nm$ and $1950nm$, show a deviation from corresponding experimental results, mostly in the transition from the initial position to the focus line. Possible reasons for these differences are:

1. Uncertainties in the physical parameters used for the computational modeling; for example, the actual diameter of the microbeads may vary.
2. Approximations of the initial velocity of the microbead, required for the simulation, from the observed position data, may contain some error.
3. A three-dimensional bead model may more accurately capture the physical phenomena than the planar model used here.

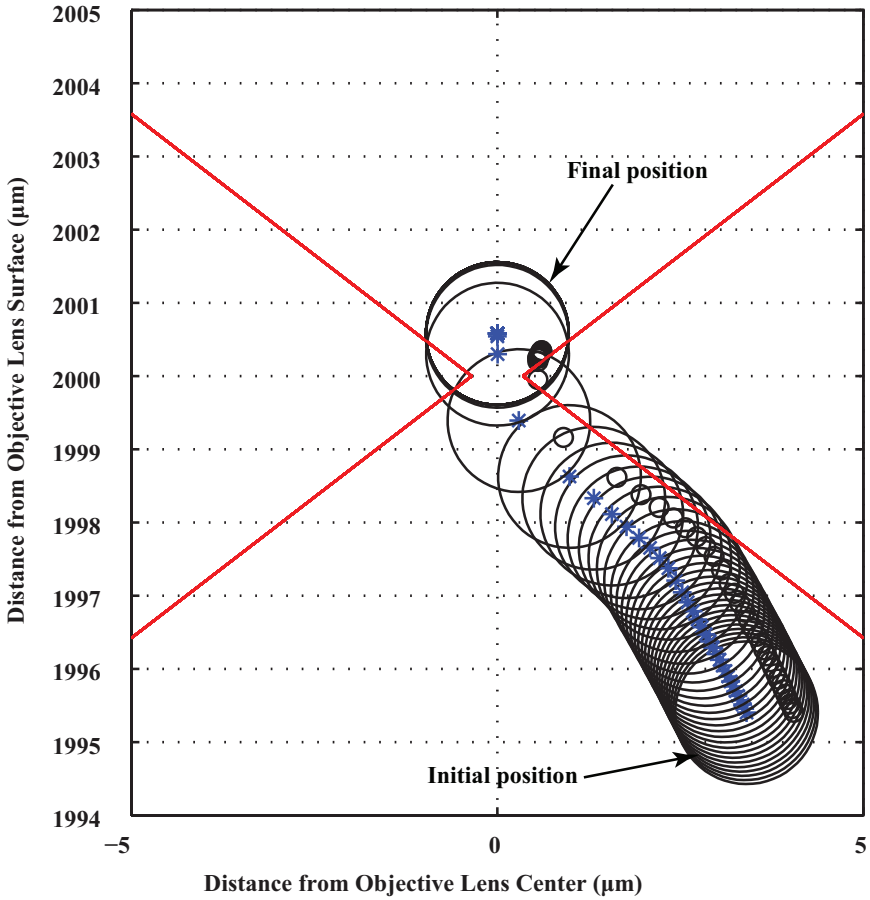

Figure 2.10. A few snapshots of the simulation result for the transient motion of $1950nm$ bead from the initial to final position. The time interval of the snapshots is $0.4ms$. (CPUtime=$13mins$, `AbsTol`=10^{-8}, `RelTol`=10^{-7}, $\Delta t = 0.001ms$) .

4. Discretization of the laser beam into only 15 laser rays may introduce some error; however, this approximation is more accurate when the bead is near the focal line.
5. The force produced by the laser on the $500nm$ bead may be better modeled using Mie scattering theories, rather than the ray-optics approach.
6. The scaling factor, introduced in the section 2.3 for the simulation, may need finer tuning.
7. General numerical integration errors.

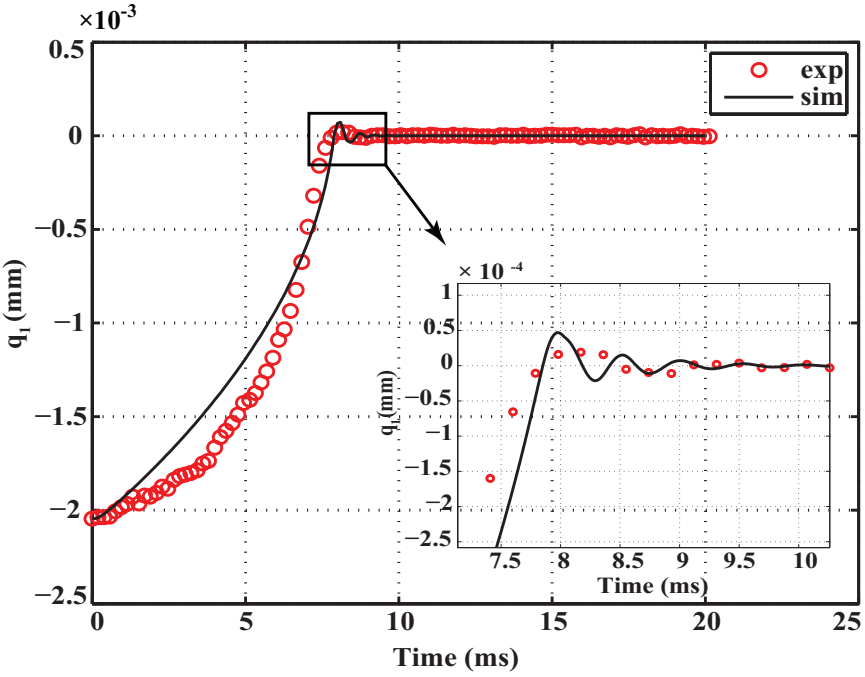

Figure 2.11. Comparison of experimental data (open circles) and simulation data (line) for q_1 coordinate of $990nm$ microparticle using the multiscale model (CPUtime=$2.5mins$, `AbsTol`=10^{-8}, `RelTol`=10^{-7}, $\Delta t = 0.001ms$). The experimental result is generated by Bryan Black in department of physics .

Still, this simple model does capture the key aspect of oscillatory behavior which was sought.

2.4.3 Check Order of the First Term

The quality of the estimate provided by the multiscale model can be assessed by checking the assumption of small first terms in the relations of (2.17). This is done by calculating (2.17) during simulation. The simulation results in Figs. 2.15a and 2.15b for the $1950nm$ bead show that the order of the first term, both translational and rotational terms, is small, as expected to be on the order of the scaling value of $a_2 = 8 \times 10^{-3}$.

A similar conclusion can be drawn for the simulation of the translational coordinates of $990nm$ bead in Fig. 2.16a; however, the rotational term is not small, as

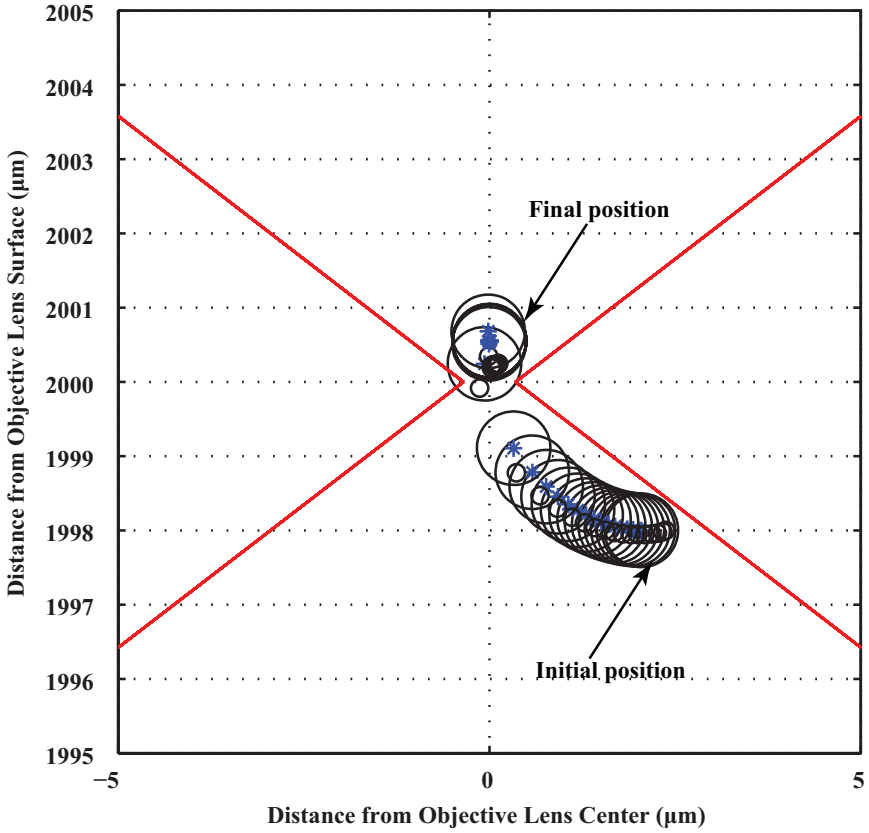

Figure 2.12. A few snapshots of the simulation result for the transient motion of $990nm$ bead from the initial to final position. The time interval of the snapshots is $0.5ms$. (CPUtime=$2.5mins$, `AbsTol`=10^{-8}, `RelTol`=10^{-7}, $\Delta t = 0.001ms$) .

illustrated in Fig. 2.16b. The scaling factor for this case is $a_2 = 2\times10^{-4}$. Some further investigation is necessary to explain this discrepancy. Similar results are obtained for the $500nm$ bead, Fig. 2.17, with a scaling factor of $a_2 = 1.5 \times 10^{-5}$.

These checks indicate that some refinement of the method for choosing the scaling factor is necessary. Still, it is interesting that the multiscale model can come quite close to predicting the behavior of these beads in the horizontal, q_1, direction, and it also still interesting that the behavior predicted by the multiscale model can be observed experimentally.

Experimental results in the vertical direction are not examined in detail here because of time-scale disagreements between simulation and experiments, though

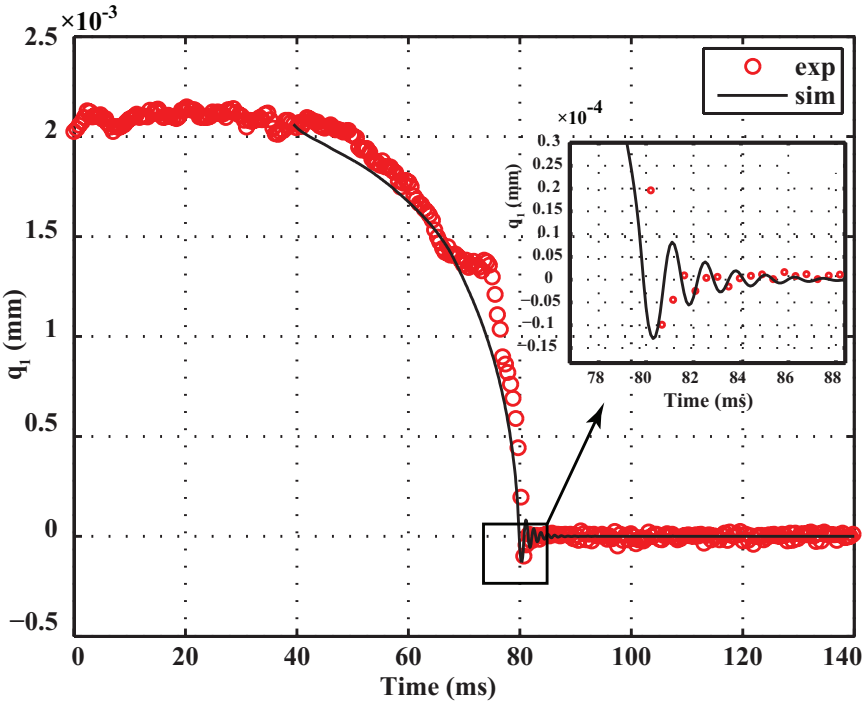

Figure 2.13. Comparison of experimental data (open circles) and simulation data (line) for q_1 coordinate of $500nm$ microparticle using the multiscale model (CPUtime=$21mins$, `AbsTol`=10^{-8}, `RelTol`=10^{-7}, $\Delta t = 0.001ms$). The experimental result is generated by Bryan Black in department of physics .

spatial agreement is acceptable. One possible reason for this is that with decreasing particle size, the mathematical treatment of light-particle interactions using ray optics becomes less accurate. Interactions on the scale of the $500nm$ particles may be better treated with Mie scattering theories, but are significantly more complex. Secondly, the method used to track these fluorescent particles in the horizontal direction cannot be used for the vertical measurements. Work is underway on new methods which will more accurately track the particle's vertical position. Simulation data for the vertical and rotational directions are discussed in appendix A.

2.5 Conclusions

Another key aspect of this work is that many of the insights discussed above apply to the particle model developed in section 2.3. The theory presented there

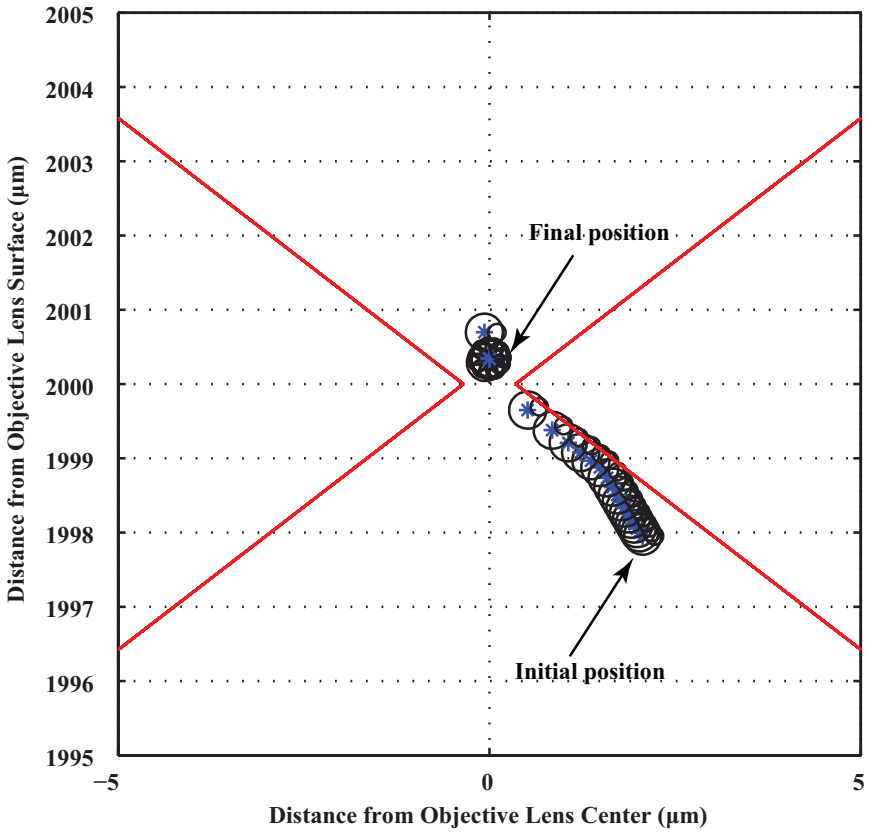

Figure 2.14. A few snapshots of the simulation result for the transient motion of $500nm$ bead from the initial to final position. The time interval of the snapshots is $2.4ms$. (CPUtime=$21mins$, `AbsTol`=10^{-8}, `RelTol`=10^{-7}, $\Delta t = 0.001ms$) .

applies to sole nanoscale particles and predicts the nanoviscosity experimentally examined for nano-sized particles in [129, 130]. Others have noticed a transition zone for particles in low Reynolds number flow between the micro and nano scale where the idea of a continuum fluid breaks down and the more discrete forces associated with Brownian motion become more prominent [131, 132], although not dominant. This is also predicted by the second order particle model proposed in section 2.3. Thus, although the focus of this article is on the behavior of a multibody system, the proposed theory can also be applied to analysis of the dynamics of nano-sized particles in varied applications.

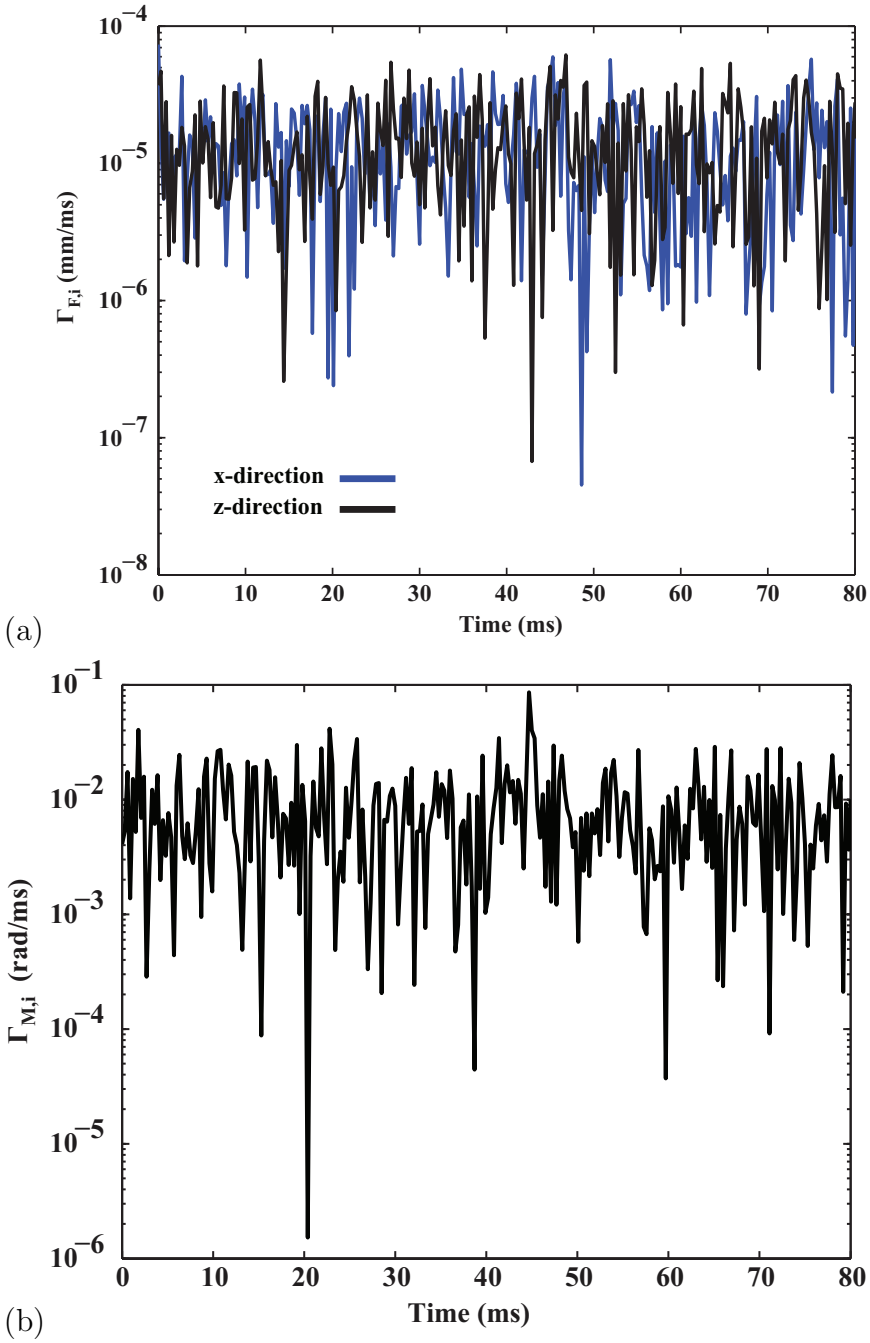

Figure 2.15. Checking the assumption of force and moment cancellation for $1950nm$. (a) The first term of forces (corresponding to the translational coordinates) in the asymptotic expansion, and (b) the first term of moment in the asymptotic expansion, (2.14).

This work focuses on the behavior of the beads as they approach the trap. It is equally interesting to study the dynamics of the particle after it is trapped as

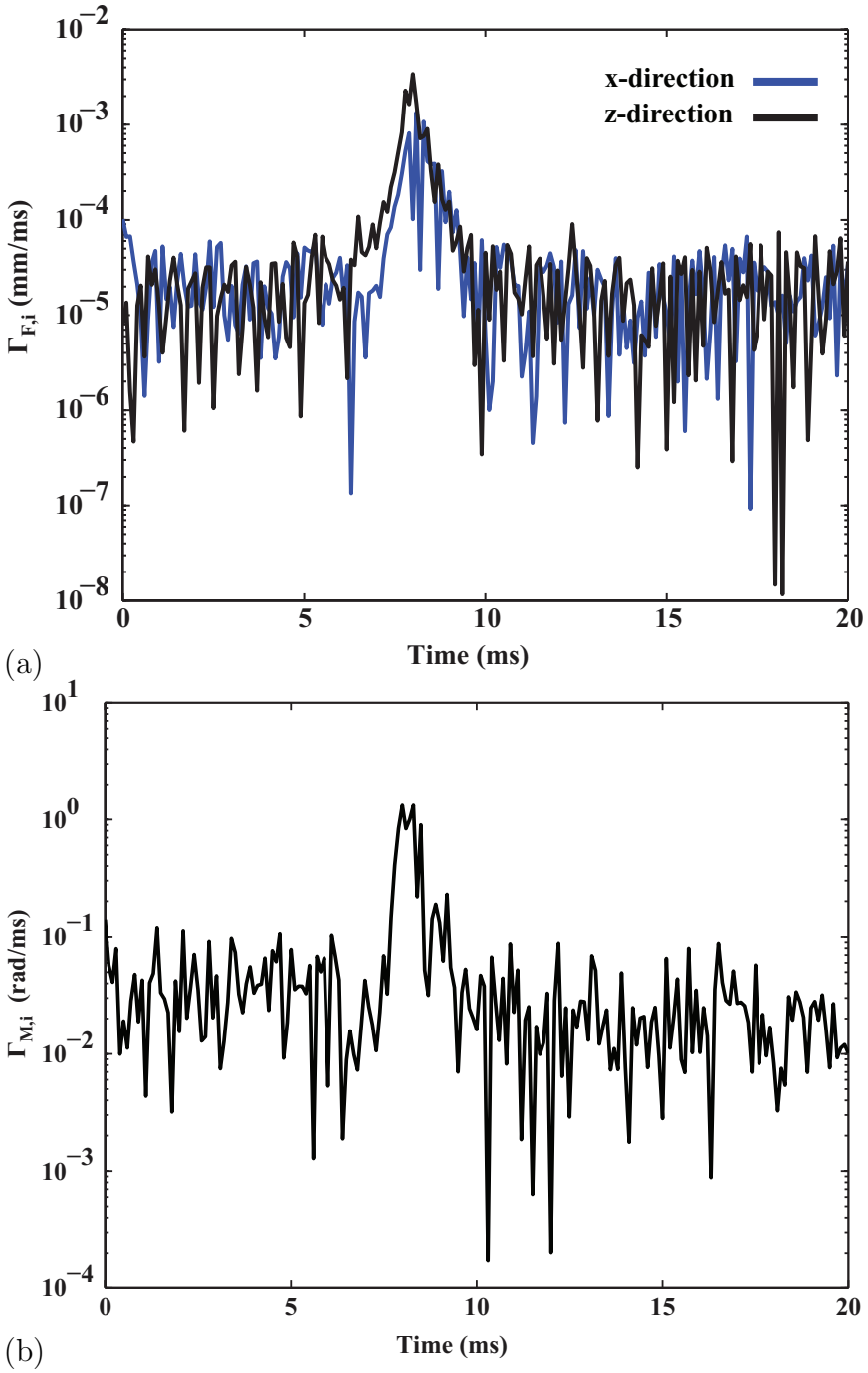

Figure 2.16. Checking the assumption of force and moment cancellation for $990nm$. (a) The first term of forces (corresponding to the translational coordinates) in the asymptotic expansion, and (b) the first term of moment in the asymptotic expansion, (2.14).

most of the prior work discussed in section 1.2 have done. The retention of mass properties in the model used herein suggests a power spectrum of the trapped beads

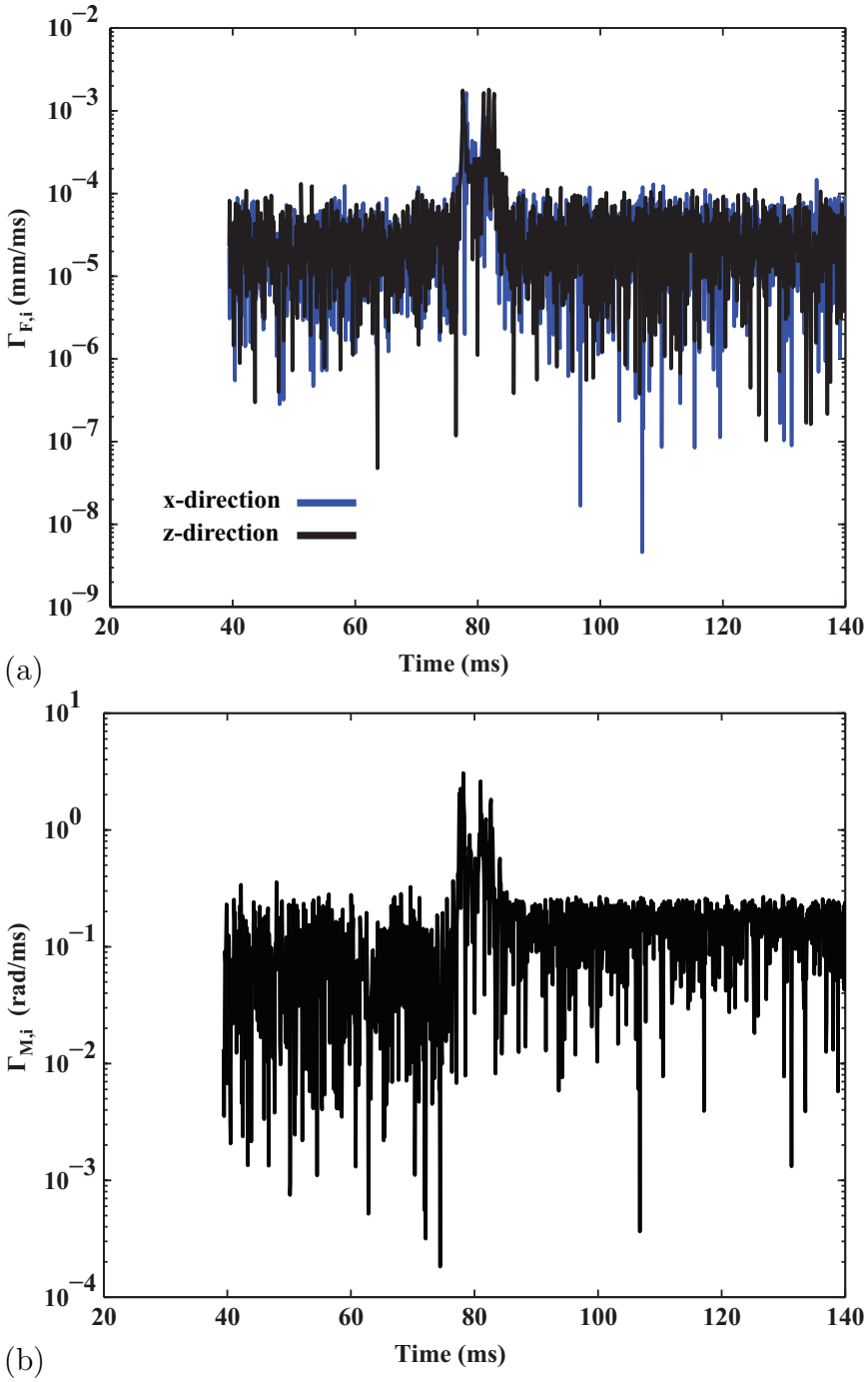

Figure 2.17. Checking the assumption of force and moment cancellation for $500nm$. (a) The first term of forces (corresponding to the translational coordinates) in the asymptotic expansion, and (b) the first term of moment in the asymptotic expansion, (2.14).

that will deviate from the Lorentzian profile predicted by the overdamped Langevin equations [182].

Chapter 3

New Multiscale Approach for Articulated Multi Rigid Body Model

3.1 Introduction

This chapter presents the extension of the proposed multiscale particle dynamics, introduced in chapter 2, into a multiscale rigid multibody dynamics. The multiscale multibody approach was implemented into mechanical modeling of biological structure of motor proteins, illustrated in Fig. 3.1, represented by a three dimensional (3D) articulated multi rigid bodies, shown in Fig. 3.2. This is a coarse-grained model generated by grouping atoms into rigid bodies that leads to eliminate unnecessary high frequency and small amplitude vibrational motions in atomistic levels. This is rational due to this fact that the interested biological phenomena, motor proteins walking process, occur with larger conformations and in longer time scales in compare to atomistic level motions.

The first (*massless*) and second (*massive*) order models were examined in order to sufficiently illustrate the differences in behavior predicted by both models. Model parameters are chosen in a manner to be close to the reality and there is an effort to match the experimentally observed pattern and speed of locomotion with ones obtained by simulation. In addition, the difference between the dynamic behaviors of the proposed 3D mechanical model with the two dimensional (2D) model developed in [1, 2] are highlighted.

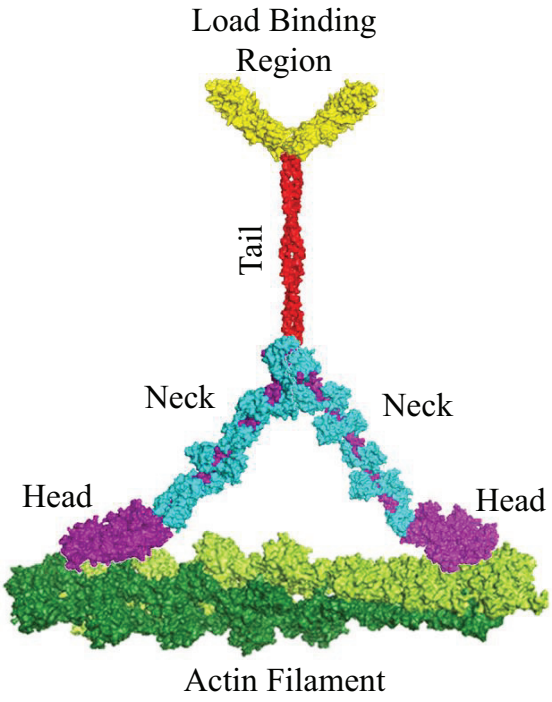

Figure 3.1. A picture of biological structure of myosin V [1, 2].

3.2 Multiscale Rigid Multibody Dynamics

Rigid body models are based on particle models, but include a larger number of particles. Thus the behavior predicted by the particle model in section 2.3 can also be valid for the rigid body model. The particle models are combined using Lagrange's equation, Kane's method, D'Alemberts principle, or any other techniques. Many rigid multibody techniques have been introduced, to address the computational issues involved in conventional molecular dynamic simulation methods, which focus on reducing the molecular system's degrees-of-freedom (DOF) by grouping particles into either beads (*bead based coarse-graining*) [183] or rigid bodies [150, 184–189](*rigid body based coarse graining*). Although in the bead based techniques, group of atoms are modeled as a rigid spheres, no inertia terms are considered in the equations of motion. In rigid body based models, the inertia terms related to the mass distribution, the Coriolis, and centripetal terms are retained in order to remain true to the original

molecular dynamic model [186]. Here, a coarse-grained 3D mechanical model is used, having the features shown in Fig. 3.2, which is not drawn to scale.

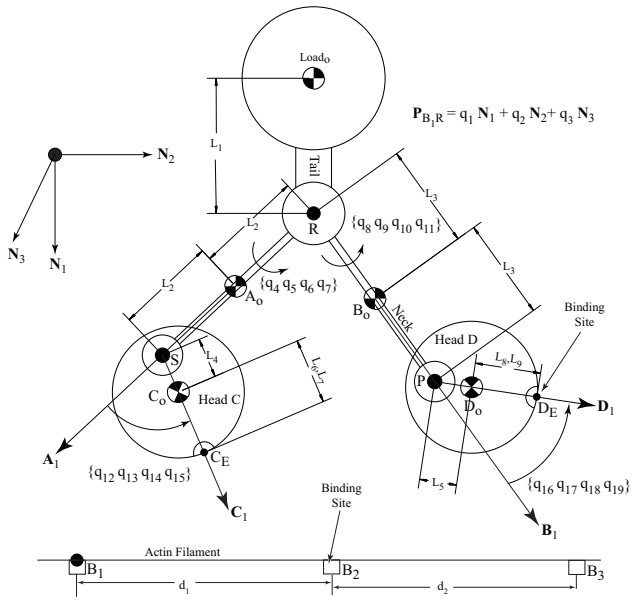

Figure 3.2. Schematic representation of myosin V. The schematic shows the different rigid bodies in the model. The 3D model is shown as a planar sketch for the sake of simplicity. Note the difference between the point 'B_1', defining an actin binding site, and the vector $\mathbf{B}_1$. $\mathbf{P}_{B_1R}$ is the position vector from point 'B_1' to point 'R' .

The mechanical model is comprised of ball-and-socket connected rigid bodies in Fig. 3.2. The connections between the tail, necks, and heads are at points 'R', 'S', and 'P' in Fig. 3.2. Euler parameters are used to model the orientation of bodies in order to eliminate singularities in their mathematical description [5, 6, 190, 191]. They are shown as sets of 4-tuple generalized coordinates, i.e. $\{q_4, q_5, q_6, q_7\}$ in Fig. 3.2. The load and tail are modeled as a single rigid body which is prohibited from rotating about point 'R'.

The objectives of this dissertation can be sufficiently met using a simplified model of the necks. They are modeled as single rigid bodies, 'A' and 'B', in order to

eliminate the complexity of the model. Experimental studies of the necks' stiffness have shown that the stretching stiffness ($k_L = 230pN/nm$) is much larger than the equivalent bending stiffness ($k_b = 0.25pN/nm$); therefore, the longitudinal extensibility in neck domain will be neglected [119, 192, 193]. However, the flexibility, bending, of the neck domain will be considered in chapter 4. The heads' shape is approximated by ellipsoids, bodies 'C' and 'D', because they simplify determination of the contact points and forces. The binding sites on each head and the actin filament are indicated in Fig. 3.2. The mass centers of each body are represented by the small half-filled circles. The vectors $\mathbf{N}_1$, $\mathbf{N}_2$ and $\mathbf{N}_3$ in Fig. 3.2 define the *inertial reference frame*. All other reference frames are attached to the different bodies.

The multibody mechanical model has the form

$$M(\mathbf{q})\ \ddot{\mathbf{q}}\ +\ \mathbf{C}(\dot{\mathbf{q}}, \mathbf{q})\ =\ \sum \mathbf{\Gamma}(\dot{\mathbf{q}}, \mathbf{q}) \tag{3.1}$$

$$\mathbf{C}(\dot{\mathbf{q}}, \mathbf{q})\ =\ \frac{dM(\mathbf{q})}{dt}\ \dot{\mathbf{q}}\ -\ \frac{\partial}{\partial \mathbf{q}}\left(\dot{\mathbf{q}}^T M(\mathbf{q})\ \dot{\mathbf{q}}\right) \tag{3.2}$$

where $\mathbf{q} = [\mathrm{q}_1 \cdots \mathrm{q}_{19}]^T$ contains the generalized coordinates in Fig. 3.2, and $\dot{\mathbf{q}}$ and $\ddot{\mathbf{q}}$ are its time derivatives of generalized speeds and accelerations. The term $M(\mathbf{q}) \in \mathbb{R}^{19\times 19}$ is the mass matrix. The forces on the left of (3.1) are referred to as *generalized inertia forces* since they depend on mass.

The forces on the right of (3.1) are referred to as *generalized active forces* defined as

$$\sum \mathbf{\Gamma}\ =\ \mathbf{\Gamma}_{contact} + \mathbf{\Gamma}_{friction} + \mathbf{\Gamma}_{charge} + \mathbf{\Gamma}_{conform} + \mathbf{\Gamma}_{Brown} \tag{3.3}$$

$$\mathbf{\Gamma}_{friction}\ =\ -\beta\ D(\mathbf{q})\ \dot{\mathbf{q}} \tag{3.4}$$

where β is the viscous damping coefficient and $D \in \mathbb{R}^{19\times 19}$ is a function of $\mathbf{q}$ which transforms friction forces and moments applied at the mass center of each body into generalized active forces. The vectors $\mathbf{\Gamma}_{charge}$, $\mathbf{\Gamma}_{contact}$, $\mathbf{\Gamma}_{conform}$, and $\mathbf{\Gamma}_{Brown}$ contain

forces related to Coulomb point charges, contact and impact, conformational changes, and Brownian motion. These forces are discussed in detail in section 3.2.1.

The unit of mass, the *attogram* (ag) is chosen so that the mass values are on the order 10^0, and the length and time units, the nanometer (nm) and millisecond (ms), are chosen for similar reasons. These masses and inertias are contained in the mass matrix $M(\mathbf{q})$ in (3.1) which is symmetric, positive definite and non-diagonal.

3.2.1 Forces

3.2.1.1 Viscous Friction

Each body has a force and moment applied at and about its mass center to approximate the viscous friction of the fluid through which the motor protein moves, as shown in Fig. 3.3.

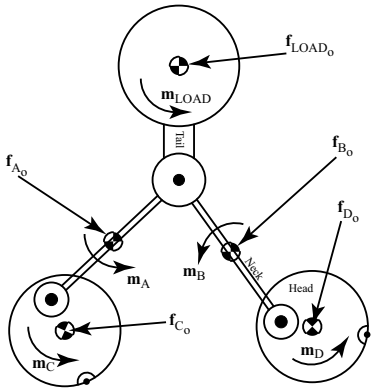

Figure 3.3. Viscous friction forces acting on myosin V .

In order to truly assess the effects of viscous friction on a rigid body, one should consider drag which depends on its shape and orientation, but here a simple coefficient of viscous friction is used.

Each body has a force and moment applied at and about its mass center to approximate the viscous friction of the fluid through which the motor protein moves, as shown in Fig. 3.3. For example, the friction force and moment on body 'A' are

$$\mathbf{f}_{A_o} = -\beta_2 \, \boldsymbol{v}_{A_o} \quad \text{and} \quad \mathbf{m}_A = -\beta_2 \, \bar{L}_A^2 \, \boldsymbol{\omega}_A \tag{3.5}$$

where $\mathbf{f}_{i_o}$ and $\mathbf{m}_i$ are the force and moment acting on body i while $\mathbf{v}_{i_o}$ and $\boldsymbol{\omega}_i$ are the translational and rotational inertial velocities associated with body i. The term $\bar{L}_i$ is a characteristic length for rotational friction; the value used is half the length of the body. The values of these coefficients are listed in Table B.1. The friction forces for each body comprise $\mathbf{\Gamma}_{friction}$.

3.2.1.2 Conformational Changes and External Forces

Several forces contribute to protein locomotion, including the conformational changes due to ATP hydrolysis. Regardless of their source and application, their resultant can be transformed into equivalent forces at the protein's joints. At this point in the development of the multibody model, it is not critical to model all of the forces contributing to protein locomotion in detail. The equivalent forces provide a simple means for generating stepping which allow examination of contact and impact between the heads and substrate.

The viscous friction, binding charge, contact, and random forces are excluded from the equivalent forces because they are modeled explicitly. The equivalent forces are modeled as three moments, one acts between the necks, and two act between the heads and necks, see Fig. 3.4. They are loosely associated with the neck linker force and power strokes at each head; however, they may have several sources beyond ATP hydrolysis. These equivalent forces comprise $\mathbf{\Gamma}_{conform}$ in (3.1).

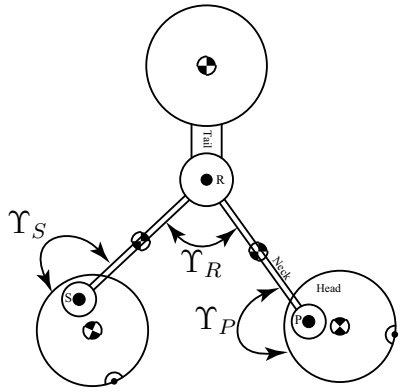

Figure 3.4. Forces emulating conformational changes and external forces .

A combination of constant neck linker [194,195] and power stroke forces is used here to produce locomotion. This is done so that the same forces can be applied to the massless and massive models. The motors are activated when both heads have docked, only one power stroke is active at any given time. Both forces are deactivated when the stepping head's binding site is $5nm$ from the actin binding site. Allowing the actin binding site to pull the head in to bind and dock, yields a more robust control, as opposed to steering the head all the way in. In addition, the power stroke is deactivated when the angle between a head and its neck is 90° assuming this is the maximum travel of the power stroke. The neck linker force is deactivated if the angle between the necks is greater than 75°. The motors apply a constant torque when activated. The equivalent moments acting on the proteins to achieve the step are listed in Table 3.1. These moments are separated into large and small components as,

$$\mathbf{\Gamma}_{conform} \;=\; G^T \begin{bmatrix} \Upsilon_R \\ \Upsilon_S \\ \Upsilon_P \end{bmatrix} \;=\; G^T \; \mathbf{\Upsilon} \tag{3.6}$$

where Υ_i is the moment associated with point 'i' and G^T transforms the moments into generalized active forces.

Table 3.1. Equivalent Joint Moments

Moment	Small Force	Large Force
Υ_R	$\pm 107 \frac{ag \cdot nm^2}{ms^2}$	$\pm 107 \times 10^8 \frac{ag \cdot nm^2}{ms^2}$
Υ_P, Υ_S	$53 \frac{ag \cdot nm^2}{ms^2}$	$53 \times 10^8 \frac{ag \cdot nm^2}{ms^2}$
Υ_R	$\pm 107 \times 10^{-9}_{pN \cdot pm}$	$\pm 10.7_{pN \cdot pm}$
Υ_P, Υ_S	$53 \times 10^{-9}_{pN \cdot pm}$	$5.3_{pN \cdot pm}$

Motors Υ_P and Υ_S are never used simultaneously.

3.2.1.3 Binding Charges

In the literature, there are charge potentials proposed which attempt to model the repulsion required to keep the head from penetrating the actin filament. Since the repulsion forces are addressed using contact forces, herein the binding potential only models the attraction between the binding sites using a simple Coulomb-like charge model. The attractive forces resulting from these charges are shown in Fig. 3.5.

The interaction of the motor protein with the actin filament involves docking of the heads at the binding sites [196, 197]. Here, this docking is assumed to completely immobilize the bound head and only occurs when the point binding sites on a head and the actin filament closely align. Modeling the head as an ellipse ensures that the head must achieve a particular configuration before docking is allowable, as would occur for the actual protein.

When a head docks, it is assumed that the charges involved sum and are neutralized; the charges at the docking site do not affect the undocked head. This is accomplished by setting the charges involved equal to zero. These charges remain zero until the head detaches, after which only the charge on the binding site is set back to its original value.

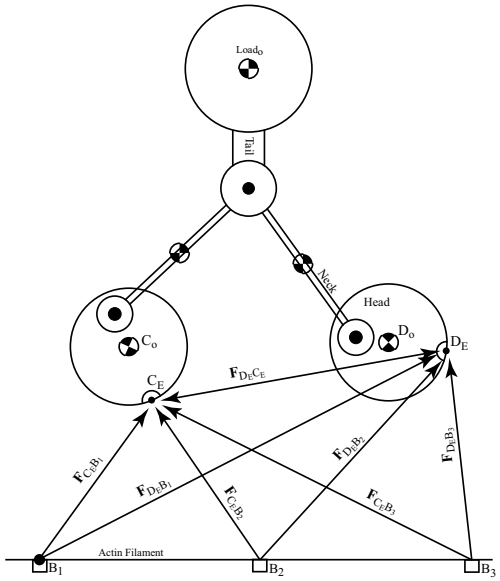

Figure 3.5. Binding charges on myosin V .

After detaching, the head must recharge at some point during its motion in order to achieve the step. The head charge is switched back on when its binding site has passed mid step and is 2/3 of the way to the targeted binding site on the actin filament. The head needs to be closer to the new binding site than to the old since the binding charges are a function of distance. If not, the head will be pulled back to the original binding site.

The position vectors from the heads' mass centers to their binding sites are expressed as

$$\mathbf{P}_{\mathrm{C_oC_E}} \;=\; L_6\,\mathbf{C}_1 \;+\; L_7\,\mathbf{C}_2 \tag{3.7}$$

$$\mathbf{P}_{\mathrm{D_oD_E}} \;=\; L_8\,\mathbf{D}_1 \;+\; L_9\,\mathbf{D}_2\;. \tag{3.8}$$

The force on a head's binding site, '$\mathrm{C_E}$' due to site '$\mathrm{B_1}$' for example, is

$$\mathbf{F}_{\mathrm{C_EB_1}} \;=\; \mathrm{f}_{\mathrm{C_EB_1}}\,\frac{\mathbf{P}_{\mathrm{C_EB_1}}}{\|\mathbf{P}_{\mathrm{C_EB_1}}\|}\;. \tag{3.9}$$

There are a number of charge potentials investigated in the literature for defining the attractive force $\mathrm{f}_{\mathrm{C_E B_1}}$. These include ratchet potentials [195] and Coulomb-like potentials [41]. A Coulomb-like charge potential [41], is used here:

$$V(r) \;=\; \frac{C_{\mathrm{C_E}}\; C_{\mathrm{B_1}}\; e^{k(a-r)}}{4\pi\epsilon_0\epsilon_r(1+ka)\;(r+k_o)} \tag{3.10}$$

where ϵ_0, ϵ_r, k, and a are the permittivity of free space, relative electric permittivity, inverse of the Debye length, and excluded volume radius; the values for these constants are given in Table B.1. The term r is the distance between the binding sites and k_o is a penetration depth used to keep the potential from becoming infinite. The terms $C_{\mathrm{C_E}}$ and $C_{\mathrm{B_1}}$ are the charges on the binding sites of head 'C' and '$\mathrm{B_1}$' on the actin fiber; these values are given in Table B.1. The absolute value of this potential as a function of radial distance is illustrated in Fig. 3.6.

The force can be found as

$$\mathrm{f}_{\mathrm{C_E B_1}} \;=\; -\frac{dV(r)}{dr} \;=\; \frac{C_{\mathrm{C_E}}\; C_{\mathrm{B_1}}\; e^{k(a-r)}}{4\pi\epsilon_0\epsilon_r(1+ka)}\;\frac{k(r+k_o)+1}{(r+k_o)^2} \tag{3.11}$$

where $r = \|\mathbf{P}_{\mathrm{C_E B_1}}\|$ is the distance between the head and actin binding sites at points '$\mathrm{C_E}$' and '$\mathrm{B_1}$' in Fig. 3.2. Similar forces can be defined between the other binding sites. These charge forces comprise $\mathbf{\Gamma}_{charge}$ in (3.1) and are separated into small and large components,

$$\mathbf{\Gamma}_{charge} \;=\; \mathrm{Q}\;\mathbf{f}_{charge} \tag{3.12}$$

where the matrix Q transforms the charges into generalized active forces. The force $\mathrm{f}_{\mathrm{C_E B_1}}$ generated by the charge potential as a function of radial distance is illustrated in Fig. 3.6.

These charges are electrostatic and only depend on the relative positions of the binding sites. They are conservative forces whose values are always known. Thus it

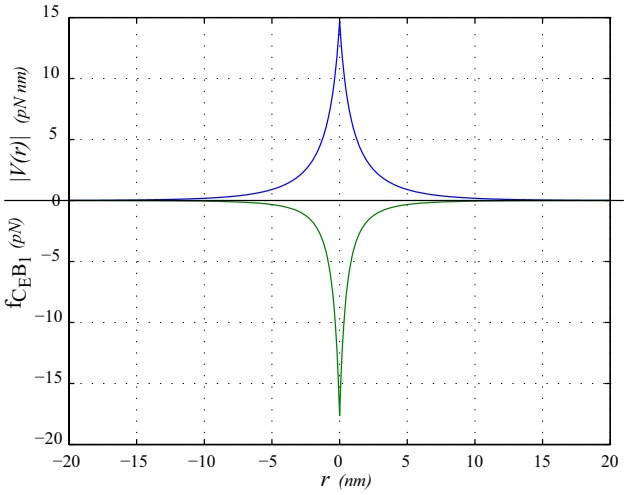

Figure 3.6. Absolute value of the charge potential and the associated force .

is necessary to ensure that their computed values and the decomposed values match up. This is accomplished by defining f_{ij}

$$\mathbf{f}_{charge} \;=\; [\; \mathrm{f}_{\mathrm{C_EB_1}} \quad \mathrm{f}_{\mathrm{C_EB_2}} \quad \cdots \quad \mathrm{f}_{\mathrm{D_EB_5}} \quad \mathrm{f}_{\mathrm{D_EB_6}} \;]^T \tag{3.13}$$

where $\mathrm{f}_{\mathrm{C_EB_1}}$ is determined from (3.11).

3.2.1.4 Contact Forces

Here it is assumed that contact between the heads and the actin filament occurs in a localized region which can be approximated as point contact. Modeling the heads as ellipsoids aligns with this assumption. In this work the heads and actin are assumed to be frictionless, for the sake of simplicity, thus the horizontal forces illustrated in Fig. 3.7 do not represent tangential friction. They are used to enforce an immobilization of the head when it docks.

As stated, the heads are modeled as ellipsoids:

$$\frac{x_C^2}{r_{head_1}^2} \;+\; \frac{y_C^2}{r_{head_2}^2} + \frac{z_C^2}{r_{head_3}^2} \;=\; 1 \tag{3.14}$$

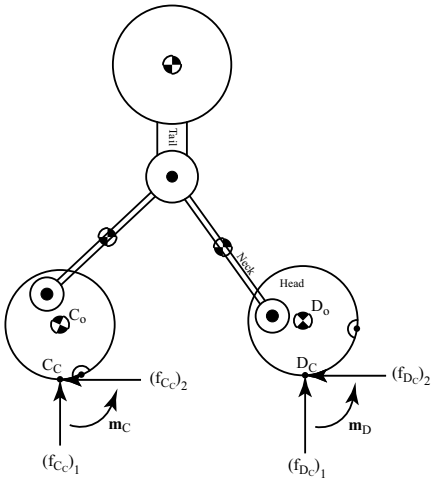

Figure 3.7. Contact forces on myosin V. .

where the position vector between point 'C_o' and any point 'C_C' on the surface of the head is expressed as

$$\mathbf{P}_{C_oC_C} \;=\; x_C\;\mathbf{C}_1 \;+\; y_C\;\mathbf{C}_2 \;+\; z_C\;\mathbf{C}_3 \tag{3.15}$$

and likewise for head 'D'. Table .1 gives the values of r_{head_1}, r_{head_2} and r_{head_3} assuming both heads are identical.

The contact forces are shown in Fig. 3.7 and defined as

$$\mathbf{\Gamma}_{contact} = J_p^T\;\mathbf{F}_{contact} = J_p^T \begin{bmatrix} \mathbf{f}_{\mathrm{C_C}} \\ \mathbf{m}_{\mathrm{C}} \\ \mathbf{f}_{\mathrm{D_C}} \\ \mathbf{m}_{\mathrm{D}} \\ \mathbf{f}_{\mathrm{R}} \end{bmatrix} \tag{3.16}$$

$$\boldsymbol{v}_p = \begin{bmatrix} \boldsymbol{v}_{\mathrm{C_C}} \\ \boldsymbol{v}_{\mathrm{D_C}} \\ \boldsymbol{v}_{\mathrm{R}} \end{bmatrix} = J_p\;\dot{\mathbf{q}} \tag{3.17}$$

where $\boldsymbol{v}_p$ contains the inertial velocities of the contact points, 'C_C' and 'D_C', as well as that of point 'R'. Although all possible contacts are shown in (3.17), only the ones actually contact/impact are selected using the impact Jacobian, J_p.

The contact forces are calculated as

$$\mathbf{F}_{contact} = -\left(J_p A^{-1} J_p^T\right)^{-1} \left(\dot{J}_p \dot{\mathbf{q}} + J_p A^{-1} \left(\mathbf{\Gamma}_{fccB} - \mathbf{b}\right)\right) \tag{3.18}$$

$$\mathbf{\Gamma}_{fccB} = \mathbf{\Gamma}_{friction} + \mathbf{\Gamma}_{charge} + \mathbf{\Gamma}_{conform} + \mathbf{\Gamma}_{Brown} \ . \tag{3.19}$$

Since $\mathbf{F}_{contact}$ depends on the other forces, its large portion is found by substituting the other large forces into (3.18) and solving.

3.2.1.5 Brownian Motion

Random forces and moments in the model, representing Brownian motion, are implemented as Gaussian white noise. They act at and about the mass center of each body, as shown in Fig. 3.8.

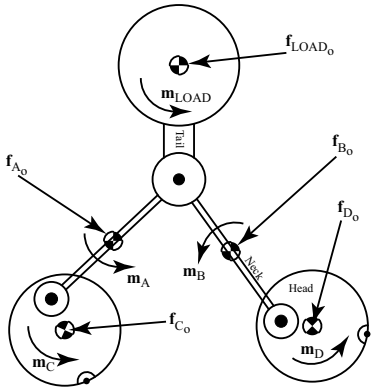

Figure 3.8. Brownian motion for myosin V. .

The random forces and moments shown in Fig. 3.8 representing Brownian motion, are defined, for example, as

$$\begin{aligned} \mathbf{f}_{Co} &= C_{o1}(t)\ \mathbf{N}_1 + C_{o2}(t)\ \mathbf{N}_2 + C_{o3}(t)\ \mathbf{N}_3 \\ \mathbf{m}_C &= \bar{L}_C\ C_{o1}(t)\ \mathbf{N}_1 + \bar{L}_C\ C_{o2}(t)\ \mathbf{N}_2 + \bar{L}_C\ C_{o3}(t)\ \mathbf{N}_3 \end{aligned} \tag{3.20}$$

where $\bar{L}_C$ is a characteristic length of body 'C'. Similar forces act on the other bodies. The $C_{oi}(t)$ represent forces produced by randomly fluctuating thermal noise. Each component of the random force and moment is treated independently as a normally distributed random variable [195]. They have the following *expectations*, $E[\cdot]$, or weighted average values,

$$E\,[\ C_{oi}(t)\ ]\ =\ \langle\ C_{oi}(t)\ \rangle\ =\ 0\ =\ \mu \tag{3.21}$$

and are governed by a fluctuation-dissipation relation expressed as

$$E\,[\ C_{oi}(t_1)\ C_{oj}(t_2)\ ] = 2\ \beta\ k_B\ \mathrm{T}\ \delta(t_1 - t_2)\delta_{i,j} \tag{3.22}$$

where k_B and T are the Boltzmann constant and absolute temperature [195, 198]. The relation in (3.22) implies that there is no time dependency between the random process over time; the random sequence of forces does not repeat regularly.

In addition, (3.21) and (3.22) imply

$$E[C_{oi}^2(t)]\ =\ 2\ \beta\ k_B\ \mathrm{T}\ =\ \mathrm{Var}(C_{oi}(t))\ =\ \sigma^2 \tag{3.23}$$

which is the variance of C_{oi}. Thus the C_{oi} can be generated using the Matlab function `normrnd`$(\mu, \sigma, \ldots)$ which generates random variables with a normal distribution.

The collection of random forces comprise $\mathbf{\Gamma}_{Brown}$. These randomly fluctuating discontinuous functions slow numerical integration so each random variable is held constant during a single integration step; the random variable is updated at the

beginning of each step. Thus the value of each random variable is known before the integration step, and the decomposed value of the random force must equal it. This is accomplished by defining

$$\mathbf{\Gamma}_{Brown} = \mathrm{R}_{nd}\ \mathbf{r}_{nd} = \mathrm{R}_{nd} \begin{bmatrix} C_{o1} \\ C_{o2} \\ C_{o3} \\ \vdots \end{bmatrix} \tag{3.24}$$

where R_{nd} transforms the random forces into generalized active forces. An example of the random forces used is given in Fig. 3.9.

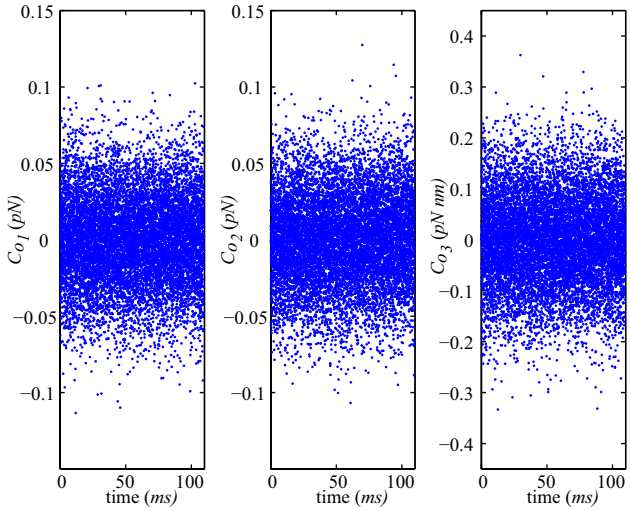

Figure 3.9. Random forces acting on head 'C' in Fig. 3.15. .

3.2.2 The First Order Model

Dividing (3.1) by the viscous damping coefficient yields an equivalent to (4.2),

$$\mathbf{0} \;=\; \frac{M(\mathbf{q})\ \ddot{\mathbf{q}} \;+\; \mathbf{C}(\dot{\mathbf{q}}, \mathbf{q})}{\beta} \;=\; \frac{\mathbf{\Gamma}_{cccB}}{\beta} \;-\; D\ \dot{\mathbf{q}} \tag{3.25}$$

where $\mathbf{\Gamma}_{cccB}$ includes all generalized active forces in (3.4) except the friction force. Since all particles in the first order model (4.2) are massless, combining them into rigid body model yields a first order model where velocity is directly proportional to force,

$$\dot{\mathbf{q}} \;=\; D^{-1}\;\frac{\mathbf{\Gamma}_{cccB}}{\beta} \tag{3.26}$$

matrix D is a function of the generalized coordinates which transforms viscous friction forces and moments applied at the mass center of each body into generalized active forces. It is a real symmetric matrix which may be positive definite or semi-positive definite (partially damped) [199], therefore it is not invertible all the time. However, invertibilty issue have never been experienced during the integration of the first order model in (3.26). The first order model has a highest derivative of smaller order than the original model in (3.1), referred to as *reduction of order*, which yields a *singular perturbation problem* [57].

3.2.3 The Second Order Model

Herein, the multiscale rigid multibody approach will be derived based on the proposed multiscale particle dynamics, introduced in section 2.3, that leads to a second order rigid multibody model. First, (3.1) is rewritten as below

$$m_{tot}\;\bar{M}(\mathbf{q})\;\ddot{\mathbf{q}}\;+\;m_{tot}\;\bar{\mathbf{C}}(\dot{\mathbf{q}},\mathbf{q})\;+\;\beta\;D(\mathbf{q})\;\dot{\mathbf{q}}\;=\;\mathbf{\Gamma}_{cccB} \tag{3.27}$$

where m_{tot} is the total mass of protein extracted from $M(\mathbf{q})$ and $\mathbf{C}(\dot{\mathbf{q}},\mathbf{q})$ as the characteristic parameter of inertia. $\mathbf{\Gamma}_{cccB}$ was defined in section 3.2.2. Now, dividing both sides of (3.27) by β yields

$$\frac{m_{tot}}{\beta}\;\bar{M}(\mathbf{q})\;\ddot{\mathbf{q}}\;+\;\frac{m_{tot}}{\beta}\;\bar{\mathbf{C}}(\dot{\mathbf{q}},\mathbf{q})\;+\;D(\mathbf{q})\;\dot{\mathbf{q}}\;=\;\frac{\mathbf{\Gamma}_{cccB}}{\beta} \tag{3.28}$$

By defining $\varepsilon = \dfrac{m_{tot}}{\beta}$ and using this in (3.28) given

$$\varepsilon\ \bar{M}(\mathbf{q})\ \ddot{\mathbf{q}}\ +\ \varepsilon\ \bar{\mathbf{C}}(\dot{\mathbf{q}},\mathbf{q})\ +\ D(\mathbf{q})\ \dot{\mathbf{q}}\ =\ \frac{\mathbf{\Gamma}_{cccB}}{\beta} \tag{3.29}$$

Based on the MMS [57], for the details of MMS refer to appendix E, the Small parameter ε is used in order to decompose the first and second derivatives of the generalized coordinates into different timescales $T_i = \varepsilon^i\ t$ as follow

$$\begin{cases} \dot{\mathbf{q}}\ =\ \dfrac{d\mathbf{q}}{dt}\ =\ \displaystyle\sum_{i=0}^{\infty} \epsilon^i\ \frac{\partial \mathbf{q}}{\partial T_i} \\ \\ \ddot{\mathbf{q}}\ =\ \dfrac{d^2\mathbf{q}}{dt^2}\ =\ \displaystyle\sum_{i=0}^{\infty}\sum_{j=0}^{\infty} \epsilon^i\epsilon^j \frac{\partial^2 \mathbf{q}}{\partial T_i \partial T_j} \end{cases} \tag{3.30}$$

Substituting (3.30) into (3.29) and arranging the terms in the order of increasing power of ε gives

$$\mathbf{0} = \varepsilon^0\ \left(\frac{\mathbf{\Gamma}_{cccB}}{\beta} -\ D(\mathbf{q})\ \frac{\partial \mathbf{q}}{\partial T_0}\right) + \varepsilon^1\ \left(\bar{M}(\mathbf{q})\ \frac{\partial^2 \mathbf{q}}{\partial T_0^2}\ +\ \bar{\mathbf{C}}_{00} + \cdots\right) + \cdots \tag{3.31}$$

where

$$\begin{aligned} \bar{\mathbf{C}}_{00}\ &=\ \frac{\partial \bar{M}(\mathbf{q})}{\partial T_0}\frac{\partial \mathbf{q}}{\partial T_0}\ -\ \left(\frac{\partial \mathbf{q}^T}{\partial T_0}\bar{M}(\mathbf{q})\frac{\partial \mathbf{q}}{\partial T_0}\right) \\ \bar{\mathbf{C}}_{ij}\ &=\ \varepsilon^i\varepsilon^j\left(\frac{\partial \bar{M}(\mathbf{q})}{\partial T_i}\frac{\partial \mathbf{q}}{\partial T_j}\ -\ \frac{\partial}{\partial \mathbf{q}}\left(\frac{\partial \mathbf{q}^T}{\partial T_i}\bar{M}(\mathbf{q})\frac{\partial \mathbf{q}}{\partial T_j}\right)\right) \end{aligned} \tag{3.32}$$

Now the first term is split into small and large parts by using scaling factors a_1 and a_2 as below

$$\begin{aligned} \mathbf{0}\ =\ & a_1\ \left(\frac{\mathbf{\Gamma}_{cccB}}{\beta} -\ D(\mathbf{q})\ \frac{\partial \mathbf{q}}{\partial T_0}\right)\ +\ a_2\ \left(\frac{\mathbf{\Gamma}_{cccB}}{\beta} -\ D(\mathbf{q})\ \frac{\partial \mathbf{q}}{\partial T_0}\right)\ + \\ & \varepsilon^1\ \left(\bar{M}(\mathbf{q})\ \frac{\partial^2 \mathbf{q}}{\partial T_0^2}\ +\ \bar{\mathbf{C}}_{00} + \cdots\right) + \cdots \end{aligned} \tag{3.33}$$

where $a_1 + a_2 = 1$ and $a_1 \gg a_2$. The same discussion, presented in 2.3, is invoked here in order to remove the large part of the active forces involved in the first term of (3.33),

$$\mathbf{0}\ =\ a_1\ \left(\frac{\mathbf{\Gamma}_{cccB}}{\beta} -\ D(\mathbf{q})\ \frac{\partial \mathbf{q}}{\partial T_0}\right) \tag{3.34}$$

yielding

$$\begin{aligned}\mathbf{0} &= a_2 \left(\frac{\mathbf{\Gamma}_{cccB}}{\beta} - D(\mathbf{q}) \frac{\partial \mathbf{q}}{\partial T_0} \right) + \varepsilon^1 \left(\bar{M}(\mathbf{q}) \frac{\partial^2 \mathbf{q}}{\partial T_0^2} + \bar{\mathbf{C}}_{00} + \cdots \right) + \cdots \\ &= a_2 \frac{\mathbf{\Gamma}_{cccB}}{\beta} - \varepsilon \bar{M}(\mathbf{q}) \ddot{\mathbf{q}} - \varepsilon \bar{\mathbf{C}}(\dot{\mathbf{q}}, \mathbf{q}) - a_2 D(\mathbf{q}) \dot{\mathbf{q}} \end{aligned} \tag{3.35}$$

By rearranging (3.35), similar to (2.18), the rigid body model with scaled generalized active forces has the form,

$$M(\mathbf{q}) \ddot{\mathbf{q}} + \mathbf{C}(\dot{\mathbf{q}}, \mathbf{q}) = a_2 \mathbf{\Gamma}_{cccB} + a_2 \mathbf{\Gamma}_{friction} \tag{3.36}$$

The parameter a_2 is chosen empirically to match experimentally observed motions, but should be small to avoid the original proportionality problem. The rigid multibody model should admit under damped motion and predicts reduced viscosity similar to (2.18).

3.3 Results

Here the behaviors of the first and second order models, referred to as the massless and massive models, in section 3.2 are compared in simulation for three different cases: (1) the docking process, (2) deterministic stepping, and (3) Brownian stepping. Matlab's `ode45.m`, an adaptive ODE solver, was used to perform the numerical integration of (3.26) and (3.36). Contact and impact are handled using the new numerical constraint embedding method developed [190, 191]. The details of the constraint embedding will be discussed in chapter 5.

3.3.1 Checking The Order of the First Term

The equivalence of the first term of the asymptotic expansion, (2.14), in the rigid body model was examined during stepping which has the form,

$$\frac{1}{\beta}\begin{bmatrix}\mathbf{F}\\ \boldsymbol{\tau}\end{bmatrix} = \frac{1}{\beta}\,\boldsymbol{\Gamma}_{cccB} - D\,\frac{\partial \mathbf{q}}{\partial T_0} \tag{3.37}$$

where $\mathbf{F} \in \mathbb{R}^{3\times 1}$ and $\boldsymbol{\tau} \in \mathbb{R}^{12\times 1}$ are forces and moments, respectively.

Figures 3.10a and 3.10b show that the forces and torques related to the first term are of $O(10^{-10})$ and $O(10^{-16})$ which are of the expected small order. Therefore the process followed in (2.15)-(2.18) produced the assumed cancellation.

The first order model assumes the first term equals zero and the velocity is found to satisfy that assumption, (3.25). The proposed approach assumes that the first term is not zero but very small, but this is a difficult assumption to impose on the model. This is accomplished by scaling down the generalized active forces so that they are small, and then using these small forces in the equations of motion. This allows retention of the mass properties; in other words, the second term in the asymptotic expansion corresponding to (2.14), which includes the second order term, must be retained. The simulation results show that the order of the coefficient of the second term, $\epsilon^1 = 4.8 \times 10^{-9}$ is comparable with the order of first term, $10^{-10} nm/ms$ and $10^{-16} nm^2/ms$ corresponding to forces and moments, respectively, which means that the velocities satisfy the proposed assumption; the electrostatic and random forces are on the order of $10^0 pN$.

3.3.2 Docking

Figure 3.11 investigates the oscillatory behavior predicted by the massive model during docking, which were observed in [200–203]. Sosa et al. in [200] have shown that there is a mobility state (rocking) in head domains of kinesin during docking which is

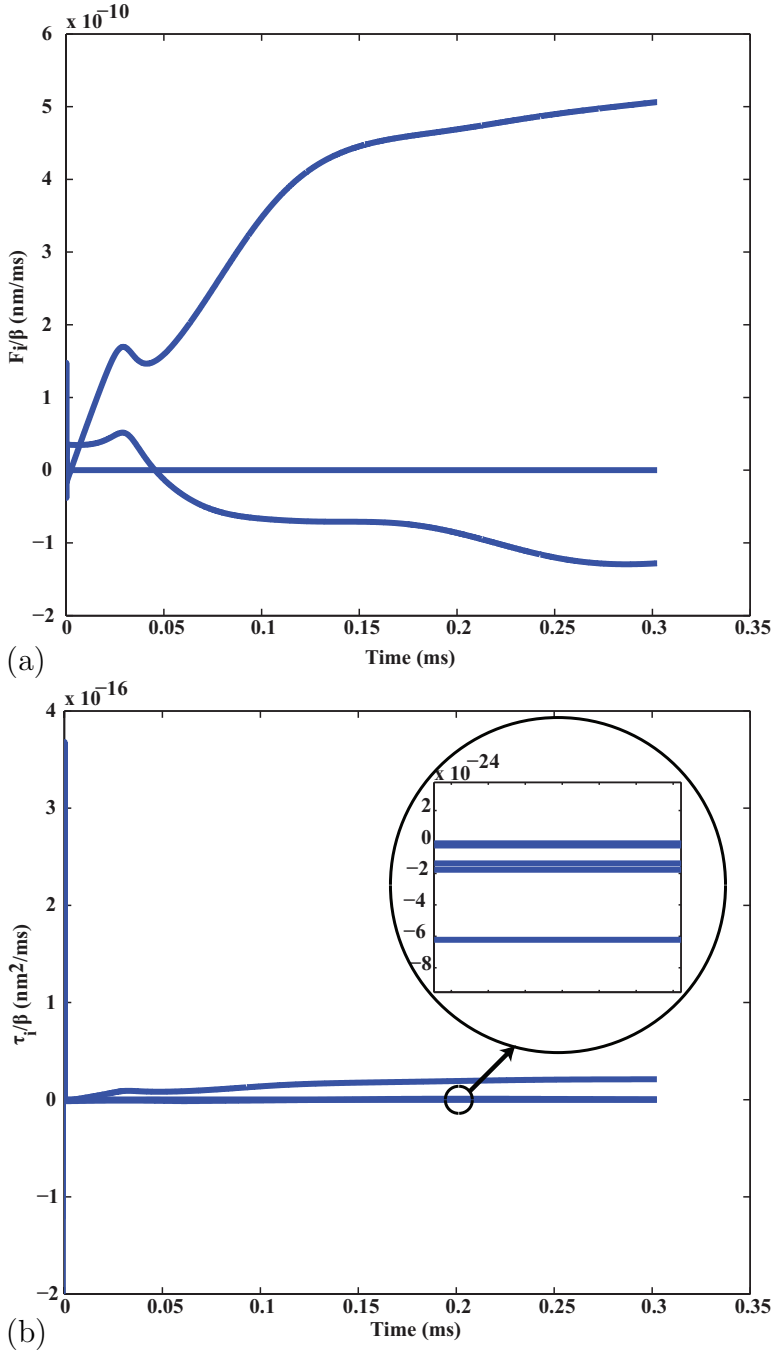

Figure 3.10. Checking the assumption of force cancellation. The small first term in the asymptotic expansion, (2.14) and (3.37), during stepping is small but not equal to zero as assumed: (a) three translational, and (b) twelve rotational terms. Note that in section (b) the rotational terms overlap each other.

induced by ADP-bound and it is not related to thermal motion. In addition, evidence

for the oscillatory behavior is present in the actomyosin system that leads to the suggestion of a common occurrence in chemomechanical cycle of motor proteins [200].

These simulations were started with the same initial conditions. Brownian motion is not included in these simulations, because of they extensive disturbance they produce in the massless model. The scaling factor, a_2, in (3.36) is adjusted to obtain the experimentally observed velocity of $1nm/ms$ for the load point, point $Load_o$ in Fig. 3.2, while, all other parameters of the two models are identical.

Docking occurs when the head's binding site falls within a $0.005nm$ cube which sits atop and is centered on the actin binding site. This small docking zone is used so that the head must achieve a particular configuration in order to dock. This mimics the actual docking of the protein which must align itself with the docking site to make a physical connection. In Fig. 3.11, the head is represented by only two lines, with the binding site at the tip, and the 3D motion is projected onto a plane in order to clearly show the oscillations.

At the beginning of the simulation, both heads are undocked but near the binding sites on the actin filament, facilitating docking. However, the heads of the massive protein oscillate, while those of the massless one do not, as shown in Fig. 3.11.

A key difference between the massive and massless models is the addition of second order behaviors, such as critically and under damped, which allow for oscillations during docking. The massless cannot predict oscillations and only allows over damped behavior. This has been a widely accepted idea based on experimental data collected for micro-sized objects in many scenarios, even attached as the load to a motor protein [34, 36, 37, 204–206]. However, some experiments visualize the motion of the heads directly and they have observed oscillatory behavior that cannot be predicted by the massless model [200–203]. The proposed massive model predicts

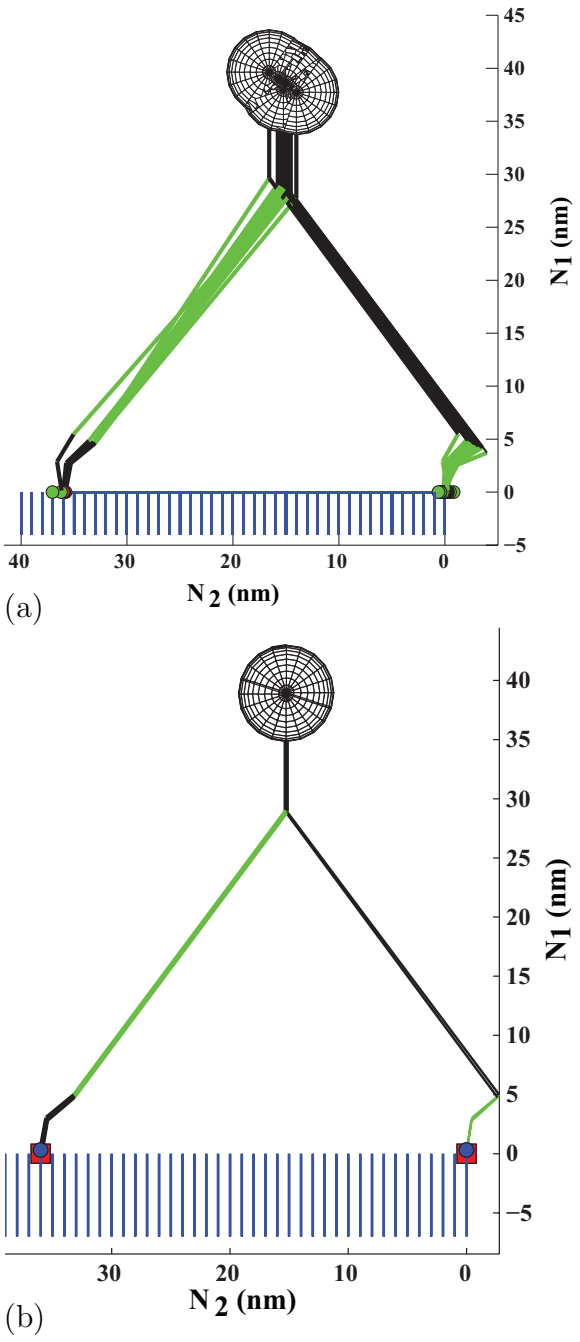

Figure 3.11. (a) Massive myosin V oscillating at the docking site versus, (b) Massless myosin V docks without oscillation.

oscillatory behavior during docking as shown in Fig. 3.11. It has been suggested that these oscillations are simply back and forth movements caused only by the diffusive motion of heads; however, near the docking site the electrostatic forces dominate and

produce these oscillations much like the behavior of a spring-mass system with low damping.

In biology, a lock-and-key model has been introduced to describe the physical connection between enzymes (motor protein's head domains) and receptors (the binding sites on the cytoskeletal filament). The back and forth movements, or oscillations, of the heads around the binding site help it to dock easily into the receptor. Interactions between the protein head's domains and the substrate at the atomic level can be interpreted as contact and impact at the molecular, nanoscale level. Therefore, contact and impact are involved in processivity of motor proteins, which use walking as their mechanism of locomotion; in fact, this work has shown that processivity is not possible without docking of the heads. Most contact models are governed by mass. Thus, the retention of the mass properties in the massive model allows the application of classical contact and impact analysis to the study of motor protein locomotion and docking. This cannot be accomplished using the massless model.

3.3.3 Deterministic Stepping

It is widely accepted that motor protein locomotion is composed of equally important random and deterministic aspects, and Figs. 3.12 and 3.13 examine only the deterministic part. After docking in Fig. 3.11, the proteins begin to step along the actin filament, as shown in Figs. 3.12 and 3.13, fueled by ATP hydrolysis. Here, the binding charge and conformational forces are activated and deactivated during each step to mimic the effect of the reactions involved in ATP hydrolysis.

As illustrated in Fig. 3.12, the trailing head of the massive protein detaches from the actin filament and moves in a hand-over-hand fashion toward the target binding site. In contrast, the massless protein remains in contact with the actin filament until midstep and then detaches, as shown in Fig. 3.13. As in Fig. 3.11a, the head of the

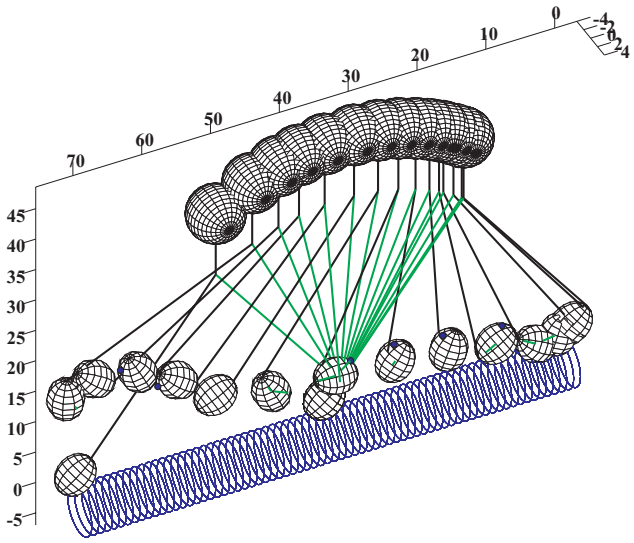

Figure 3.12. 3D massive myosin V single step. Because of more redundancy, the trailing head detach from actin filament faster than the 2D case (CPUtime = $30mins$, `AbsTol`=10^{-5}, `RelTol`=10^{-6}, $\Delta t = 0.001ms$, $v_{avg} = 1.62nm/ms$) .

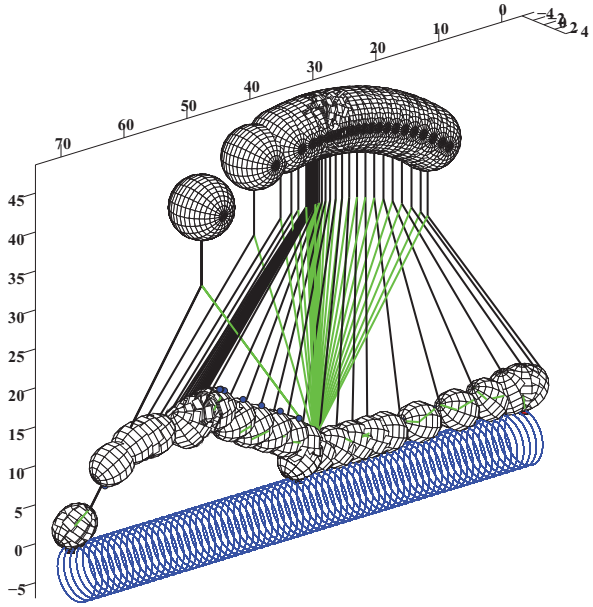

Figure 3.13. 3D massless myosin V single step. It shows same behavior as the 2D mechanical model, (CPUtime = $65mins$, `AbsTol`=10^{-5}, `RelTol`=10^{-6}, $\Delta t = 0.001ms$, $v_{avg} = 1.45nm/ms$) .

massive protein oscillates while docking. However, the massless protein has difficulty docking. These observations also hold true for the 2D massless and massive protein models examined in [1, 2].

Here the deterministic aspect of protein locomotion is examined in order to determine whether random or deterministic behavior is dominant in motor protein locomotion.

Recent experimental studies of processive motor proteins using more precise single molecule techniques have shown that they walk in a hand-over-hand fashion [34, 36, 37, 204, 207]. This is in contrast to the inchworm mechanism which had been initially suggested for locomotion of these proteins. The proposed second order model correctly replicates the observed hand-over-hand walking style, Fig. 3.12, while the locomotion of the first order model is similar to the inchworm, Fig. 3.13.

In addition, the massless model has difficulty docking. The issue here is that over damped behavior predicts that the head will approach the docking site in manner such that the distance between them decreases at an exponentially decreasing rate. This is typical of over damped systems in that they may never actually converge to the desired position, or dock. This behavior fits the classic definition of over damped behavior which is caused by the omission of the inertial properties in the first order model. The similarities and differences between the behavior predicted by the two models are the same as in the two-dimensional case discussed in [1, 2] which provides additional discussion of these phenomena.

The proposed second order model brings all the active forces into proportion with the mass-acceleration terms so the integration step size was increased from *femto second* to *micro second*. The proposed approach provides this opportunity to increase the simulated time to the same order of biological phenomena time scale *millisecond-second* along with the decrease in the simulation run time from *several*

months using atomistic models to *hours*. The reduction in run time using the new model allows theoretical exploration of a large number of biological phenomena. These include the interactions between different types of molecules including ligands, receptors, hormones, antibodies, enzymes, viruses, neurotransmitters and other molecular structures.

3.3.4 Random Stepping

Here the combination of random and deterministic behaviors is examined in Figs. 3.14 and 3.15 for a single step. Locomotion of nanoscale particles, such as motor proteins, is affected by the random forces associated with Brownian motion. In this work, random forces are modeled as Gaussian white noise and kept constant during a single time step. All forces used in the deterministic stepping are active during the simulation of random stepping.

Figures 3.14 and 3.15 show the Brownian motion of the massive and massless proteins. Both proteins display diffusion of the heads out in every direction, as has been experimentally observed [193, 208]. However, the random forces associated with Brownian motion have less of an effect on the massive protein in contrast to the large effect they have on the massless model. This allows the massive protein to complete a step and dock while the massless protein does not. This implies that random forces do not assist the massless protein in docking.

The results show a significant difference between the behavior predicted by the 3D massless and massive protein models. In several aspects, the massive model shows behavior that is more realistic. This is discussed further in the following sections.

Brownian motion plays important role in locomotion of particles at the nanoscale. Because of this, some works have suggested a pure diffusive motion to describe processivity of motor proteins, referred to as Brownian motors. These ideas are based

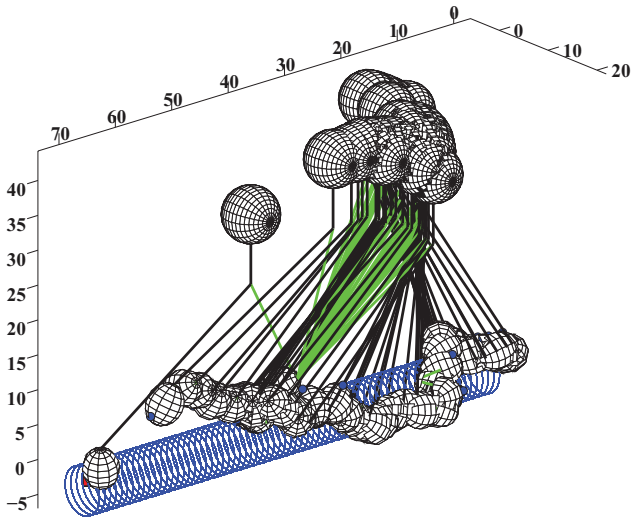

Figure 3.14. 3D massive protein and Brownian motion. The protein is directed by the inertial forces toward the next binding site and it has no difficulty docking (CPUtime $= 1.5hours$, `AbsTol` $= 10^{-5}$, `RelTol` $= 10^{-6}$, $\Delta t = 0.001ms$, $v_{avg} = 0.85nm/ms$) .

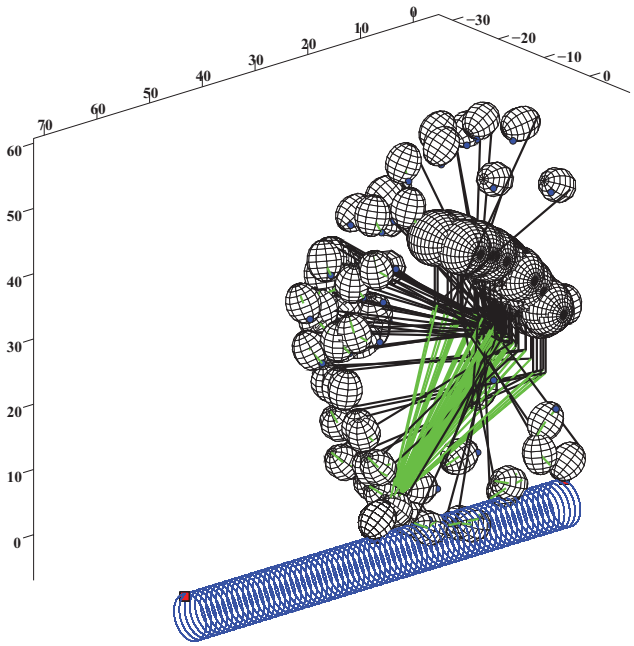

Figure 3.15. 3D massless protein under the influence of Brownian motion. The simulation was stopped because head 'C' does not approach to the target binding site (CPUtime $= 5hours$, `AbsTol` $= 10^{-5}$, `RelTol` $= 10^{-6}$, $\Delta t = 0.001ms$, $v_{avg} = 0.45nm/ms$) .

on the massless model and suggest that diffusion should cause greater movement of the protein than the deterministic motion suggests [209]. This is shown to be true for the massless model in Fig. 3.15 where the random forces nearly overwhelm the deterministic ones and cause large diffusive motions. In Fig. 3.15 random forces have such a large effect that they prevent the heads from reaching the docking site.

However, experiments show that motor proteins move slower than is predicted by the dominant diffusion driving the massless model [209]. In contrast, the massive model predicts a reduced effect of random forces yielding a motion that is nearer to the deterministic motion examined in Fig. 3.12. The widely-accepted assumption is that motor protein locomotion is a combination of random and deterministic behavior. The mass properties attenuate the effect of Brownian motion, allowing for random-deterministic locomotion which facilitates stepping and docking, as shown in Fig. 3.14. Brownian motion decreases the average velocity of the both massless and massive models, compared with the deterministic cases. In addition, adding random forces to the model increases the simulation run time, but still less than that obtained from atomistic methods or molecular dynamic simulations.

The new 3D mechanical model was developed as an extension of the 2D model discussed in previous works [1, 2]. Despite general agreement between the resulting motion of the 2D, [2], and 3D models, there are some differences between them. First, the random motion of the 3D massive protein is less perturbed than the 2D model. This is because the energy of Brownian motion is distributed in three dimensions rather than two. Second, in contrast to the 2D model, the trailing head of the random 3D massless protein does not approach toward the target binding site on the actin filament. The reason is that the 3D massless model can move in three dimensional space, one extra direction than the 2D model, making it less likely to reach the binding site. In addition, this work also showed that a 3D model can

predict significantly different behavior than a more simplified 2D model, especially with respect to Brownian motion. The 3D model is closer to reality than the 2D, so it is reasonable to assume that Brownian motion may not have that significant of an impact on processivity.

3.4 Conclusions

A key result of this work showed that the conclusions drawn from a multiscale analysis of particle dynamics, introduced in chapter 2, can be applied to a more complex rigid body model. The technique used to develop the multiscale rigid body model was based on a simpler analysis of particle dynamics and displayed behavior predicted by the particle model. This is highly advantageous because of the complexity of the 3D rigid body model. The next step involves consideration of flexibility and chemical kinetics to this model in order to obtain an even more realistic simulation of motor protein dynamics. The ultimate goal of this work is to facilitate the development of biological simulations that allow theoretical investigations of biological phenomena in a reasonable amount of time.

Chapter 4

New Multiscale Approach for Flexible Model

4.1 Introduction

This chapter presents an extension of the proposed multiscale approach, presented in chapters 2 and 3, for the case that an extra term, which represents flexibility such as spring force, is added into the equations of motion. In this case, there is an additional term with the orders of magnitude larger than other terms; thus, the original multiscale approach was modified in order to handle this extra disproportionality [6, 8, 9]. The later proposed multiscale approach will be first introduced using particle dynamics similar to chapter 2.

However the rigid model is adequate for predicting the overall dynamic behavior of motor proteins locomotion but experimental studies has shown the evidence of flexibility in the biological structure of these super molecules especially in the neck domain. Therefore, in a further step a finite segment multibody model, articulated rigid multibodies connected with flexible elements like spring, was developed in order to investigate the effect of the flexibility along side presenting more realistic behavior of these proteins. Adding flexibility into the mechanical model of motor proteins causes an extra disproportionality between terms involved in the equations of motion that needs a special treatment based on the theory derived in section 4.2. The finite segment model was developed and tested in both 3D and 2D versions as same as the rigid model in order to highlight the differences.

4.2 Multiscale Particle Dynamics with Flexible Element

Motor proteins are often modeled using a small number of particles connected with flexible elements like spring [196]. Therefore, in this section the proposed multi-scale approach in section 2.3 was extended into a new form which considers flexibility in the dynamic modeling of particles. Especially, when the order of stiffness constant, corresponding to the flexible elements in the mechanical model, is many orders of magnitude larger than the order of other terms, an extra disproportionation occurs in the equations of motion that requires a special treatment to be addressed. Herein, a modification was invoked in order to address this issue. Applying Newton's second law to a representative particle yields,

$$m\,\ddot{\mathbf{x}} \;+\; \beta\,\dot{\mathbf{x}} \;+\; k\,\mathbf{x} \;=\; \mathbf{F}_s \;+\; \mathbf{F}_l \tag{4.1}$$

where $\ddot{\mathbf{x}}$ and $\dot{\mathbf{x}}$ are vectors of acceleration and velocity, $m = 0.48\ ag = 0.48 \times 10^{-18} gr$ is the total mass of myosin V, $\beta \approx 10^{8} ag/ms$ is the coefficient of viscous friction for water, and $k = 10^{14} ag.nm^2/(ms^2.rad)$ is spring constant equivalent to elastic stiffness at the neck domains. $\mathbf{F}_s \approx O(\beta)$ and $\mathbf{F}_l \approx O(k)$ are vectors of small and large external forces, respectively. The small forces are including Brownian motion, and charge forces while the conformation force belongs to the large force category. Notice that units were chosen so that characteristic quantities would be in the order of $O(10^0)$.

Dividing both sides of (4.1) by stiffness coefficient (spring constant), k, yields,

$$\frac{m}{k}\,\ddot{\mathbf{x}} \;+\; \frac{\beta}{k}\,\dot{\mathbf{x}} \;+\; \mathbf{x} \;=\; \frac{\mathbf{F}_s}{k} \;+\; \frac{\mathbf{F}_l}{k} \tag{4.2}$$

The disproportionate size of the mass, the viscous friction and the spring constant produces a small coefficient in (4.2) when it is divided by the mass, yielding large accelerations that are difficult to numerically integrate. Reducing the time unit/scale

to picoseconds, $1ps = 10^{-12}s$, yields a coefficient of $O(10^0)$ that is easier to integrate. However, it will take a long run time, possibly a few days, to observe phenomena occurring at larger time scales. This disproportionality can be solved by omitting the small term, solving for the velocity as $\dot{\mathbf{x}} = -k\mathbf{x}/\beta + \mathbf{F}_s/\beta + \mathbf{F}_l/\beta$, and integrating to find $\mathbf{x}(t)$ [41, 42]. This *massless* and *first order* model is the basis for the well-known Langevin [44, 107, 121] and Fokker-Planck equations [117, 127].

Alternately, techniques from the *method of multiple scales* (MMS) can be used to eliminate only the large forces that create large accelerations [6, 8, 9]. The MMS allows an investigation of the model's behavior at different time scales. This process begins by determining two characteristically small numbers, $\beta/k = 1 \times 10^{-6}\ ms$ and $m/\beta = 4.8 \times 10^{-9}\ ms$ from the model in (4.2).

$$\begin{aligned} \mathbf{0} &= \epsilon_2\ \epsilon_1\ (1ms)^2\ \ddot{\mathbf{x}}\ +\ \epsilon_1\ (1ms)\ \dot{\mathbf{x}}\ +\ \mathbf{x}\ -\ \frac{\mathbf{F}_s}{k}\ -\ \frac{\mathbf{F}_l}{k} \\ &= \epsilon_2\ \epsilon_1\ \ddot{\tilde{\mathbf{x}}}\ +\ \epsilon_1\ \dot{\tilde{\mathbf{x}}}\ +\ \mathbf{x}\ -\ \frac{\mathbf{F}_s}{k}\ -\ \frac{\mathbf{F}_l}{k} \end{aligned} \tag{4.3}$$

where $\epsilon_1 = 1 \times 10^{-6}$ and $\epsilon_2 = 4.8 \times 10^{-9}$. Now, by defining a new variable $\mathbf{u}$,

$$\begin{aligned} \mathbf{u} &= \frac{\beta}{k}\dot{\mathbf{x}}\ -\ \frac{\mathbf{F}_s}{k} = \epsilon_1 \left(\dot{\tilde{\mathbf{x}}}\ -\ \frac{\mathbf{F}_s}{\beta} \right) \\ \dot{\mathbf{u}} &= \frac{\beta}{k}\ddot{\mathbf{x}}\ -\ \frac{\dot{\mathbf{F}}_s}{k} = \epsilon_1 \left(\ddot{\tilde{\mathbf{x}}}\ -\ \frac{\dot{\mathbf{F}}_s}{\beta} \right) \end{aligned} \tag{4.4}$$

Equation (4.3) can be split in two first order differential equations as follow,

$$\begin{cases} \mathbf{0} = \epsilon_1 \left(\dot{\tilde{\mathbf{x}}}\ -\ \dfrac{\mathbf{F_s}}{\beta} \right)\ -\ \mathbf{u} \\ \\ \mathbf{0} = \epsilon_2\ \dot{\mathbf{u}}\ +\ \epsilon_2\epsilon_1 \dfrac{\dot{\mathbf{F}}_s}{\beta}\ +\ \mathbf{u}\ +\ \mathbf{x}\ -\ \dfrac{\mathbf{F}_l}{k} \end{cases} \tag{4.5}$$

The small parameters ϵ_1 and ϵ_2 are used to decompose the time variable into different scales, $T_i = \epsilon_1^i t$ and $\tau_i = \epsilon_2^i t$, respectively, yielding:

$$\begin{cases} \dot{\bar{\mathbf{x}}} = \dfrac{d\bar{\mathbf{x}}}{dt} \;=\; \epsilon_1^0 \dfrac{\partial \bar{\mathbf{x}}}{\partial T_0} \;+\; \epsilon_1^1 \dfrac{\partial \bar{\mathbf{x}}}{\partial T_1} \;+\; \epsilon_1^2 \dfrac{\partial \bar{\mathbf{x}}}{\partial T_2} \;+\; \cdots \\ \\ \dot{\mathbf{u}} = \dfrac{d\mathbf{u}}{dt} \;=\; \epsilon_2^0 \dfrac{\partial \mathbf{u}}{\partial \tau_0} \;+\; \epsilon_2^1 \dfrac{\partial \mathbf{u}}{\partial \tau_1} \;+\; \epsilon_2^2 \dfrac{\partial \mathbf{u}}{\partial \tau_2} \;+\; \cdots \end{cases} \tag{4.6}$$

Substituting (4.6) into (4.5), and arranging in order of increasing power of ϵ_1 and ϵ_2 yields,

$$\begin{cases} \mathbf{0} = \epsilon_1^0 (-\mathbf{u}) + \epsilon_1^1 \left(\dfrac{\partial \bar{\mathbf{x}}}{\partial T_0} \;-\; \dfrac{\mathbf{F}_s}{\beta} \right) + \epsilon_1^2 \left(\dfrac{\partial \bar{\mathbf{x}}}{\partial T_1} \right) + \cdots \\ \\ \mathbf{0} = \epsilon_2^0 \left(\mathbf{u} + \mathbf{x} - \dfrac{\mathbf{F}_l}{k} \right) + \epsilon_2^1 \left(\dfrac{\partial \mathbf{u}}{\partial \tau_0} + \dfrac{\epsilon_1}{\beta} \dfrac{\partial \mathbf{F}_s}{\partial \tau_0} \right) + \epsilon_2^2 \left(\dfrac{\partial \mathbf{u}}{\partial \tau_1} \right) + \cdots \end{cases} \tag{4.7}$$

The difference between $\epsilon_1^0 = 1$ and $\epsilon_1^1 = 1 \times 10^{-6}$, also $\epsilon_2^0 = 1$ and $\epsilon_2^1 = 4.8 \times 10^{-9}$ are large, so it is likely that the large terms (*active forces*) in (4.1) must cancel to some extent for the sum in (4.7) to equal zero. This is accomplished by decomposing the ϵ_1^0 and ϵ_2^0 terms, into large and small parts using scaling factors a_1, a_2, b_1 and b_2,

$$\begin{cases} -\mathbf{u} \;=\; (a_1 \;+\; a_2)\,(-\mathbf{u}) \\ \mathbf{u} + \mathbf{x} - \dfrac{\mathbf{F}_l}{k} \;=\; (b_1 \;+\; b_2) \left(\mathbf{u} + \mathbf{x} - \dfrac{\mathbf{F}_l}{k} \right) \end{cases} \tag{4.8}$$

where $a_1 + a_2 = 1$, $b_1 + b_2 = 1$ and $a_1 \gg a_2$, $b_1 \gg b_2$. Substituting (4.8) back into (4.7) yields

$$\begin{cases} \mathbf{0} = (a_1 + a_2)\,(-\mathbf{u}) + \epsilon_1^1 \left(\dfrac{\partial \bar{\mathbf{x}}}{\partial T_0} - \dfrac{\mathbf{F}_s}{\beta} \right) + \epsilon_1^2 \left(\dfrac{\partial \bar{\mathbf{x}}}{\partial T_1} \right) + \cdots \\ \\ \mathbf{0} = (b_1 + b_2) \left(\mathbf{u} + \mathbf{x} - \dfrac{\mathbf{F}_l}{k} \right) + \epsilon_2^1 \left(\dfrac{\partial \mathbf{u}}{\partial \tau_0} + \dfrac{\epsilon_1}{\beta} \dfrac{\partial \mathbf{F}_s}{\partial \tau_0} \right) + \epsilon_2^2 \left(\dfrac{\partial \mathbf{u}}{\partial \tau_1} \right) + \cdots \end{cases} \tag{4.9}$$

Herein, it is assumed that the large terms, scaled by a_1 and b_1, cancel to the extend that the large forces can be removed from (4.9), yielding a set of equations of the form

$$\begin{aligned} \mathbf{0} &= a_2\left(-\mathbf{u}\right) + \epsilon_1^1\left(\frac{\partial \bar{\mathbf{x}}}{\partial T_0} - \frac{\mathbf{F}_s}{\beta}\right) + \epsilon_1^2\left(\frac{\partial \bar{\mathbf{x}}}{\partial T_1}\right) + \cdots \\ &= -a_2\ \mathbf{u} + \frac{\beta}{k}\dot{\mathbf{x}}\ -\ \frac{\mathbf{F}_s}{k} \end{aligned} \tag{4.10}$$

$$\begin{aligned} \mathbf{0} &= b_2\left(\mathbf{u} + \mathbf{x} - \frac{\mathbf{F}_l}{k}\right) + \epsilon_2^1\left(\frac{\partial \mathbf{u}}{\partial \tau_0} + \frac{\epsilon_1}{a_2\ \beta}\frac{\partial \mathbf{F}_s}{\partial \tau_0}\right) + \epsilon_2^2\left(\frac{\partial \mathbf{u}}{\partial \tau_1}\right) + \cdots \\ &= b_2\left(\mathbf{u} + \mathbf{x} - \frac{\mathbf{F}_l}{k}\right) + \frac{m}{\beta}\left(\dot{\mathbf{u}}\ +\ \frac{\dot{\mathbf{F}}_s}{a_2\ k}\right) \end{aligned} \tag{4.11}$$

assuming $\frac{d\mathbf{x}}{dt} = \frac{\partial \mathbf{x}}{\partial T_0}$, $\frac{d\mathbf{u}}{dt} = \frac{\partial \mathbf{u}}{\partial \tau_0}$, and $\frac{d\mathbf{F}_s}{dt} = \frac{\partial \mathbf{F}_s}{\partial \tau_0}$. Notice that the second term in (4.11) is modified in order to be consistent with (4.10). In addition, the scaling in (4.10) and (4.11) preserves the relative magnitudes between the constituent forces and brings them into proportion with the mass.

Now, it is desired to bring back (4.10) and (4.11) into the original form. In order to do that, it is required to replace $\mathbf{u}$ and $\dot{\mathbf{u}}$ in (4.11) by (4.10) and it's derivative, respectively; that leads to elimination of $\frac{\dot{\mathbf{F}}_s}{a_2\ k}$.

$$\frac{m}{\beta}\left(\frac{\beta}{a_2\ k}\ \ddot{\mathbf{x}}\right) + b_2\left(\frac{\beta}{a_2\ k}\ \dot{\mathbf{x}} - \frac{\mathbf{F}_s}{a_2\ k} + \mathbf{x} - \frac{\mathbf{F}_l}{k}\right) = \mathbf{0} \tag{4.12}$$

Multiplying (4.12) by $a_2 k$ yields a second order model,

$$m\ddot{\mathbf{x}}\ +\ b_2\ \beta\dot{\mathbf{x}}\ +\ a_2 b_2\ k\mathbf{x}\ =\ b_2\ \mathbf{F}_s\ +\ a_2 b_2\ \mathbf{F}_l \tag{4.13}$$

where a_2 and b_2 are found by matching the speed or other characteristics of the predicted and experimentally observed motions. Since all of the terms in (4.13) are in proportion, it can be numerically integrated in a reasonable time.

In addition to the computational advantage of the scaling technique, the proposed approach provides new physical insights into better understanding of physical and biological phenomena happened at the micro and nanoscale. First, underdamped behaviors of molecular motors witnessed in [200]. This requires the retention of inertial effect at the small length scales which is predicted correctly by keeping mass-acceleration term in (4.13). Second, a significant reduction in viscosity at the nanoscale was experimentally measured by Gapinski and Szymanski [129, 130]. This fact is reproduced theoretically in the proposed multiscale approach, corresponding to the scaled friction force in (4.13). Finally, based on the different scaled forces in the modified equations of motion, (4.13), we suggest that the regulation of external forces, applied to molecular motors, happens at different scales. For example, large forces, such as conformational and elastic forces, are mostly regulated together while small forces like charge, random and viscous friction forces are mostly canceled by each other. However the general active forces are in different orders of magnitude but one may conclude that these forces do not create significant motor protein's locomotion beyond those produced by the a_2 and b_2 scaled forces.

The second order model in (4.13) is consistence with the original one in [1–5]. It can be proved just by assuming the order of stiffness is equal to the viscous friction force that leads to the scaling factor a_2 be equal one; then (4.13) perfectly matches with the original model [1–5].

4.3 Multiscale Finite Segment Multibody Dynamics

In this section, the effect of flexibility in neck domain of motor proteins, especially myosin V, is considered. Therefore, a 3D mechanical coarse-grained model of myosin V, shown in Fig. 4.1, is developed. The mechanical model is comprised of rigid bodies corresponding to two heads, two necks, a tail and a load, which is

illustrated in Fig. 4.2a. The load and tail are modeled as a single rigid body without much detail because this would only complicate the model. The deformable necks are modeled as three rigid bodies, bodies 'A', 'C', 'E' for one of the necks and bodies 'B', 'D', 'G' for another neck, connected through spherical joints. At each joint, there is a torsional spring which attaches the two adjacent bodies, as illustrated in Fig. 4.2b, and add flexibility to the neck domains. These torsional springs act around the axis of rotations, shown in Fig. 4.2b, and imply resistance forces due to relative rotation of adjacent bodies. The heads are approximated by ellipsoids, bodies 'H' and 'K', to ensure that the head must reach a particular orientation in order to dock with the actin filament as occurs in reality. All bodies are connected by spherical joints, centered at points R, P1, P2, P3, S1, S2 and S3. The actin filament is modeled as a cylinder which is shown as a line in Fig. 4.2. The binding sites, 'B1', 'B2', and etc., are equally spaced along the actin filaments at $36nm$ intervals.

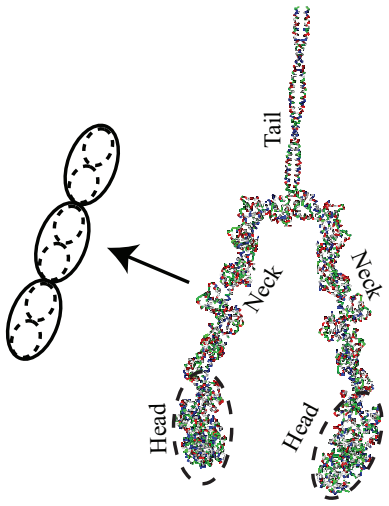

Figure 4.1. 3D structure of myosin V in ribbon presentation obtained from RCSB protein data bank (PDB ID: 2dfs) [210]. Myosin V's neck domain comprises of tandem elements called IQ motifs, drawn schematically as dash ellipses. It can be considered as three pairs, shown as solid ellipses, which can bending at junctures between them.

Similar to the 3D mechanical model in section 3.2, Euler parameters, which are shown as sets of 4-tuple generalized coordinates e.g. $\{q_4, q_5, q_6, q_7\}$ in Fig. 4.2a, are used to model the orientation of bodies in order to eliminate singularities in the description. Here a new computational strategy, developed in [5,190,191], is employed to address the extraneous coordinates involved in dynamics of the multibody model due to use of Euler parameters.

Now, the idea developed in section 4.2 can be extended to a multiscale multibody model. The equations of motion for finite segment model is developed using Kane's method and has the following form

$$\begin{cases} M(\mathbf{q})\ \ddot{\mathbf{q}} \ + \ \mathbf{C}(\dot{\mathbf{q}}, \mathbf{q}) \ + \ D(\mathbf{q})\ \dot{\mathbf{q}} \ + \ K(\mathbf{q})\ \mathbf{q} \ = \ \mathbf{\Gamma}_s + \mathbf{\Gamma}_l \\ H\dot{\mathbf{q}} = \mathbf{0} \end{cases} \tag{4.14}$$

where $\mathbf{q}$ contains the generalized coordinates, and $\dot{\mathbf{q}}$ and $\ddot{\mathbf{q}}$ are its time derivatives of generalized velocity and acceleration. The term $M(\mathbf{q})$ is the mass matrix. $\mathbf{C}(\dot{\mathbf{q}}, \mathbf{q})$ is the non-linear inertial terms including Coriolis and centrifugal terms. $D(\mathbf{q})$ and $K(\mathbf{q})$ are drag coefficient and non-linear elastic stiffness matrices, respectively. The forces on the right of (4.14), $\mathbf{\Gamma}_s \approx O(\beta)$ and $\mathbf{\Gamma}_l \approx O(k)$, are small and large generalized active forces, respectively, defined as

$$\begin{aligned} \mathbf{\Gamma}_s &= \mathbf{\Gamma}_{charge} \ + \ \mathbf{\Gamma}_{contact} \ + \ \mathbf{\Gamma}_{Brownian} \\ \mathbf{\Gamma}_l &= \mathbf{\Gamma}_{conform} \end{aligned} \tag{4.15}$$

The terms on the right hand side of (4.15) contain forces related to Coulomb point charges, contact and impact, conformational changes, and Brownian motion defined in section 3.2.1. H is the holonomic constraint matrix and $\mathbf{0}$ is a column vector of 0. In the numerical integration of (4.14), the constraint part of it will be embedded, online during simulation, into the main part in order to reduced (4.14) and eliminate extra generalized coordinates. Therefore, for the sake of simplicity the constraint

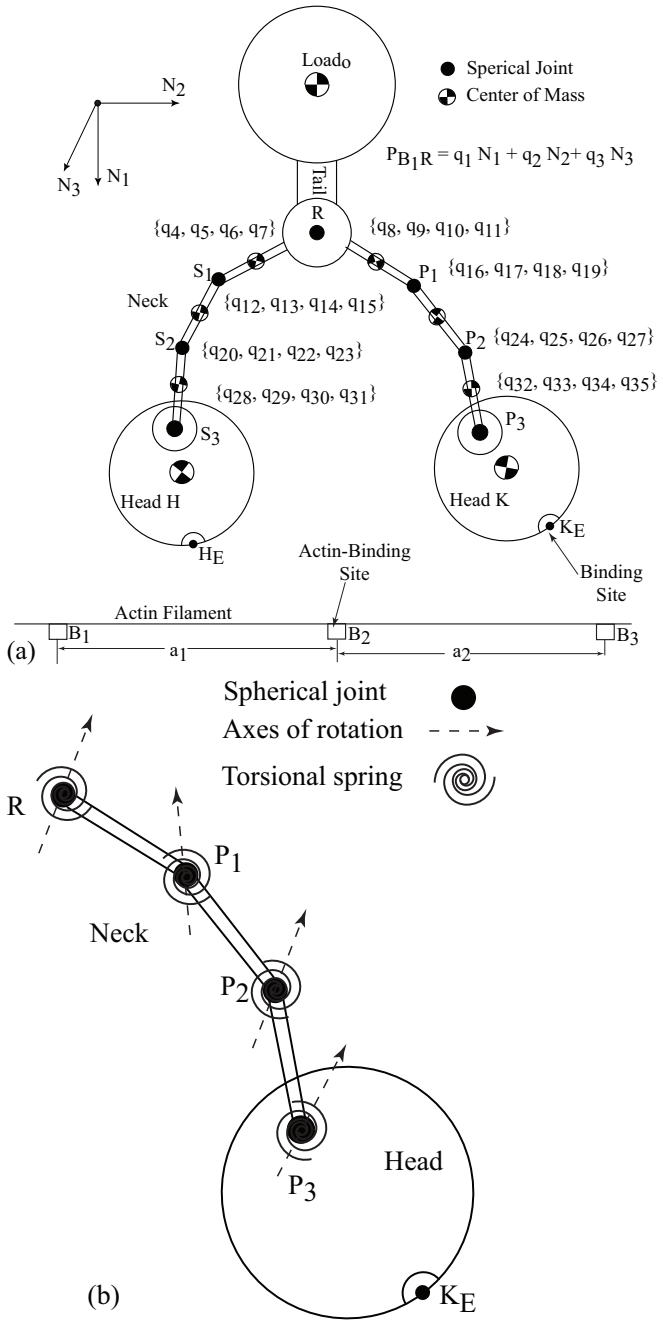

Figure 4.2. a) A schematic representation of myosin V with flexible neck, (not drawn to scale). The schematic shows the different rigid bodies in the model. b) A mechanical model of myosin V's neck (not drawn to scale). The flexibility of neck domain is modeled by rigid bodies assembled through spherical joints (black solid circle) and torsional springs (spiral shape objects). Adjacent links (bodies) have a relative motion around the axes of rotation (dashed arrow). The 3D model is shown as a planar sketch for the sake of simplicity.

equation in (4.14) will not be shown anymore in the following. The forces acting on this model are defined in detail in section 3.2.1.

By factoring the characteristic parameters including the total mass of myosin V (m), the viscous damping coefficient of surrounding fluid (β) and stiffness coefficient (spring constant) of neck domains (k) from the mass, drag, and stiffness matrices in (4.14), respectively, it can be converted to the similar form as (4.1),

$$m\bar{M}(\mathbf{q})\ \ddot{\mathbf{q}} + m\bar{\mathbf{C}}(\dot{\mathbf{q}},\mathbf{q}) + \beta\bar{D}(\mathbf{q})\ \dot{\mathbf{q}} + k\bar{K}(\mathbf{q})\ \mathbf{q} = \mathbf{\Gamma}_s + \mathbf{\Gamma}_l \tag{4.16}$$

Using the same concept developed in section 4.2 for particle dynamics, (4.16) can be written as below,

$$\epsilon_1\epsilon_2\bar{M}(\mathbf{q})\ \ddot{\mathbf{q}} + \epsilon_1\epsilon_2\bar{\mathbf{C}}(\dot{\mathbf{q}},\mathbf{q}) + \epsilon_1\bar{D}(\mathbf{q})\ \dot{\mathbf{q}} + \bar{K}(\mathbf{q})\ \mathbf{q} = \frac{\mathbf{\Gamma}_s}{k} + \frac{\mathbf{\Gamma}_l}{k} \tag{4.17}$$

Now, decomposing (4.17) in to a set of first order differential equations yields,

$$\begin{cases} \mathbf{u} \ = \ \epsilon_1 \ \left(\dot{\mathbf{q}} \ - \ \bar{D}^{-1}\dfrac{\mathbf{\Gamma}_s}{\beta}\right) \\ \epsilon_2\bar{M}(\mathbf{q})\dot{\mathbf{u}} + \epsilon_2\bar{\mathbf{C}}(\mathbf{u},\mathbf{q}) + \bar{D}(\mathbf{q})\mathbf{u} + \bar{K}\mathbf{q} \ = \ -\epsilon_1\epsilon_2\bar{M}(\mathbf{q})\bar{D}^{-1}\dfrac{\dot{\mathbf{\Gamma}}_s}{\beta} + \dfrac{\mathbf{\Gamma}_l}{k} \end{cases} \tag{4.18}$$

Then the small parameters ε_1 and ε_2 are used to decompose (4.18) into different scales using (4.6),

$$\begin{cases} \mathbf{0} = -\epsilon_1^0\mathbf{u} + \epsilon_1^1 \ \left(\dfrac{\partial\mathbf{q}}{\partial T_0} \ - \ \bar{D}^{-1}\dfrac{\mathbf{\Gamma}_s}{\beta}\right) + \epsilon_1^2\left(\dfrac{\partial\mathbf{q}}{\partial T_1}\right) + \cdots \\ \mathbf{0} = \epsilon_2^0\left(\bar{D}(\mathbf{q})\mathbf{u} + \bar{K}\mathbf{q} - \dfrac{\mathbf{\Gamma}_l}{k}\right) + \epsilon_2^1\left(\bar{M}(\mathbf{q})\dfrac{\partial\mathbf{u}}{\partial\tau_0} + \bar{\mathbf{C}}_0 + \dfrac{\epsilon_1}{\beta}\bar{M}(\mathbf{q})\bar{D}^{-1}\dfrac{\partial\mathbf{\Gamma}_s}{\partial\tau_0}\right) \ + \ \cdots \end{cases} \tag{4.19}$$

where

$$\begin{aligned} \bar{\mathbf{C}}_0 \ &= \ \frac{\partial\bar{M}(\mathbf{q})}{\partial\tau_0}\mathbf{u} \ - \ \frac{\partial}{\partial\mathbf{q}}\left(\mathbf{u}^T\bar{M}(\mathbf{q})\mathbf{u}\right) \\ \bar{\mathbf{C}}_i \ &= \ \epsilon_2^i\left(\frac{\partial\bar{M}(\mathbf{q})}{\partial\tau_i}\mathbf{u} \ - \ \frac{\partial}{\partial\mathbf{q}}\left(\mathbf{u}^T\bar{M}(\mathbf{q})\mathbf{u}\right)\right) \end{aligned} \tag{4.20}$$

Modification of (4.19) based on (4.8) to (4.11) yields

$$\begin{aligned} \mathbf{0} &= a_2(-\mathbf{u}) + \epsilon_1^1 \left(\frac{\partial \mathbf{q}}{\partial T_0} - \bar{D}^{-1} \frac{\mathbf{\Gamma}_s}{\beta} \right) + \epsilon_1^2 \left(\frac{\partial \mathbf{q}}{\partial T_1} \right) + \cdots \\ &= -a_2 \mathbf{u} + \frac{\beta}{k} \dot{\mathbf{q}} - \bar{D}^{-1} \frac{\mathbf{\Gamma}_s}{k} \end{aligned} \tag{4.21}$$

$$\begin{aligned} \mathbf{0} &= b_2 \left(\bar{D}(\mathbf{q})\ \mathbf{u} + \bar{K}\mathbf{q} - \frac{\mathbf{\Gamma}_l}{k} \right) + \epsilon_2 \left(\bar{M}(\mathbf{q}) \frac{\partial \mathbf{u}}{\partial \tau_0} + \bar{\mathbf{C}}_0 + \frac{\epsilon_1}{\beta} \bar{M}(\mathbf{q}) \bar{D}^{-1} \frac{\partial \mathbf{\Gamma}_s}{\partial \tau_0} \right) + \cdots \\ &= b_2 \left(\bar{D}(\mathbf{q})\ \mathbf{u} + \bar{K}\mathbf{q} - \frac{\mathbf{\Gamma}_l}{k} \right) + \frac{m}{\beta} \left(\bar{M}(\mathbf{q}) \dot{\mathbf{u}} + \bar{\mathbf{C}}(\mathbf{u}, \mathbf{q}) + \bar{M}(\mathbf{q}) \bar{D}^{-1} \frac{\dot{\mathbf{\Gamma}}_s}{a_2 k} \right) \end{aligned} \tag{4.22}$$

By combining (4.21) and (4.22), the multiscale equations of motion for a finite segment multibody model has the following form,

$$M(\mathbf{q})\ddot{\mathbf{q}} + \mathbf{C}(\dot{\mathbf{q}}, \mathbf{q}) + b_2 D(\mathbf{q})\dot{\mathbf{q}} + a_2 b_2 K(\mathbf{q}) = b_2 \mathbf{\Gamma}_s + a_2 b_2 \mathbf{\Gamma}_l \tag{4.23}$$

where the scaling of the generalized active forces in the rigid body model depends on the order of forces. For example, the scaling factor of the viscous friction force is indicated by the scale factor b_2, while it is $a_2 b_2$ for spring force and the other generalized active forces which are larger than the friction force.

4.4 Results

The proposed multiscale approach was examined in order to show the effectiveness of the modification applied to the original approach for handling flexibility in dynamic modeling and simulation of myosin V's locomotion. Therefore, a 3D finite segment model of myosin V, with parameters given in [9], is used to illustrate the proposed model as shown in Fig. 4.2. The model has 27 DOF described in terms of 35 *generalized coordinates* $\mathbf{q} = [\mathrm{q}_1 \cdots \mathrm{q}_{35}]^T$. Based on this, the sizes of matrices in (4.14) are $M(\mathbf{q}) \in \mathbb{R}^{35\times35}$, $C(\mathbf{q}) \in \mathbb{R}^{35\times1}$, $D(\mathbf{q}) \in \mathbb{R}^{35\times35}$, $K \in \mathbb{R}^{35\times35}$, $H \in \mathbb{R}^{8\times35}$, and $\mathbf{0} \in \mathbb{R}^{8\times1}$. The extra generalized coordinates, related to use of Euler parameters

for describing rotation of the spherical joints, are reduced by embedding of the holonomic constraint, in (4.14), based on the new strategy developed in [190, 191]. The details of the reduction procedure can be found in chapter 5. MATLAB's `ode45.m`, an adaptive numerical integrator, was used to perform the numerical integration of the equations of motion presented in (4.23).

There are two important physical characteristics, involved in motor proteins locomotion at the nanoscale, that correct prediction of them would be interested in order to compare the ability of the proposed approach with the others. The first being the significant reduction of viscosity at the nanoscale which has been observed in [129, 130]. The second being underdamped behaviors, specifically the oscillation of heads during docking to actin, which has been experimentally witnessed in [200]. The former characteristic is obviously predicted by the proposed model as the scaling factor reduces the effect of viscosity in the equations of motion. The latter characteristic could be expected by the proposed model because of retaining inertial terms in the equations of motion; that leads to a second order model which can show underdamped behaviors. However, the mostly used model, established by other approaches [41, 42, 95, 120], is based on a large viscous coefficient, result in an overdamped locomotion, which is inconsistent with the experimental observations mentioned above.

The oscillatory behavior in head domains of myosin V is examined during a docking process by using the modified mechanical model. Docking occurs when the head's binding site (points H_E and K_E in Fig. 4.2) falls within a 0.005_{nm} cube box (see Fig. 4.2) which sits atop and is centered on the actin binding site. This small docking zone is used so that the head must achieve a particular configuration in order to dock. This mimics the actual docking of the protein which must align itself with the docking site to make a physical connection. The position of binding site (points

H_E and K_E) on the heads H and K are plotted in Fig. 4.3a and b, respectively. The results show the expected oscillation in the heads during docking which is in agreement with the results obtained by the original model without flexibility in [5].

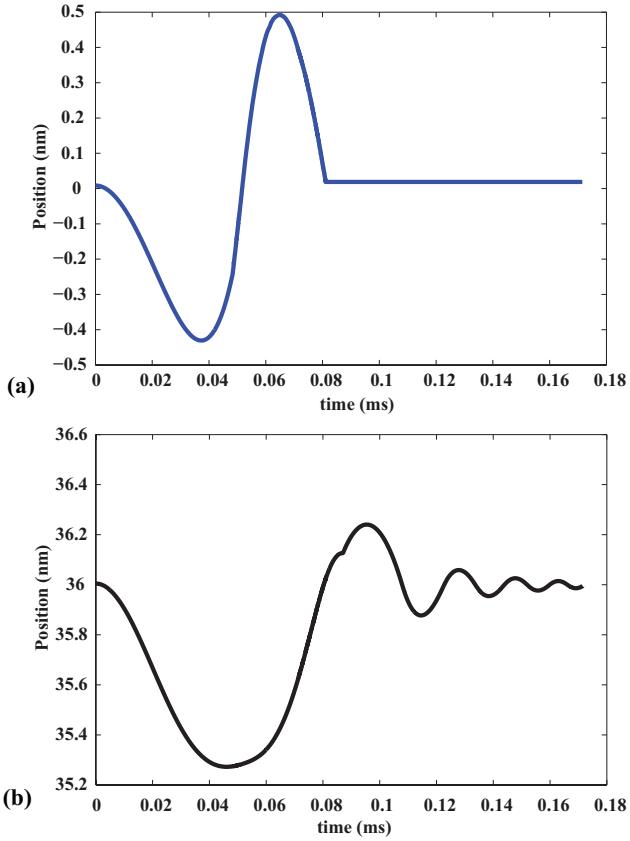

Figure 4.3. Oscillation of heads of the flexible mechanical model of myosin v during docking. At $t = 0.08ms$ the head H docks to the binding site on the substrate (point B1 in Fig. 4.2); therefore, its position is fixed after that time (a) position of the binding site (point H_E) on the head h (see Fig. 4.2), (b) position of the binding site (point K_E) on the head K (see Fig. 4.2).

Notice that the shape of these trajectories could be changed by altering the initial conditions. In this particular case, the head H docks at $t = 0.08ms$, then no more oscillation is witnessed. While, the elapsing time for the head K, to dock into the substrate, is almost two times of the head H, $t = 0.17ms$. Comparison of this

result with the time of oscillation obtained by the original model in [3,5] reveals that the flexibility of the neck domains increases oscillation of the head domains.

The overall behavior of myosin V during a single step is shown in Fig. 4.4. The random forces associated with the thermal motion at the nanoscale is ignored in this case. Experimental studies have shown that the stepping process is induced by the hydrolysis of ATP that leads to neutralize the charge and dissociation of the trailing head from the substrate. Then, the conformational change, referred to as the "power stroke", happens in myosin V that makes the trailing head goes forward to the specific binding site at 72 nm distance far from the current location (from point B_1 to B_3 in Fig. 4.2). After the trailing head passes the leading head, it is assumed that the power stroke ends, the trailing head regains its charge, and is pulled forward to the next binding site, where it attempts to dock. The 3D mechanical model with flexible necks shows the same overall behaviors as the rigid model [1–5], illustrated in Fig. 4.4. As expected, the most important difference is the bending that happens in the neck domains during stepping which was ignored in the previous rigid model [1–5].

In comparison with the results obtained by the 2D finite segment model in [6, 8, 9], illustrated in Fig. 4.5, the 3D model, as shown in Fig. 4.4a, shows two different behaviors which are: 1) bending in the leading neck before the detachment of the trailing head from actin filament, as shown in Fig. 4.6, 2) the trailing head moves upper than the load in a part of its path. *These behaviors have been experimentally observed in [211] using an electron microscopy which captured the processive movement of a single myosin V along actin filament.* Therefore, the 3D model predicts the detailed behaviors of myosin V more accurate than the 2D model. The differences can be explained by this fact that the 2D model movement was confined to a plane so it could not have enough DOF to correctly show all configurations involved in the locomotion of myosin V.

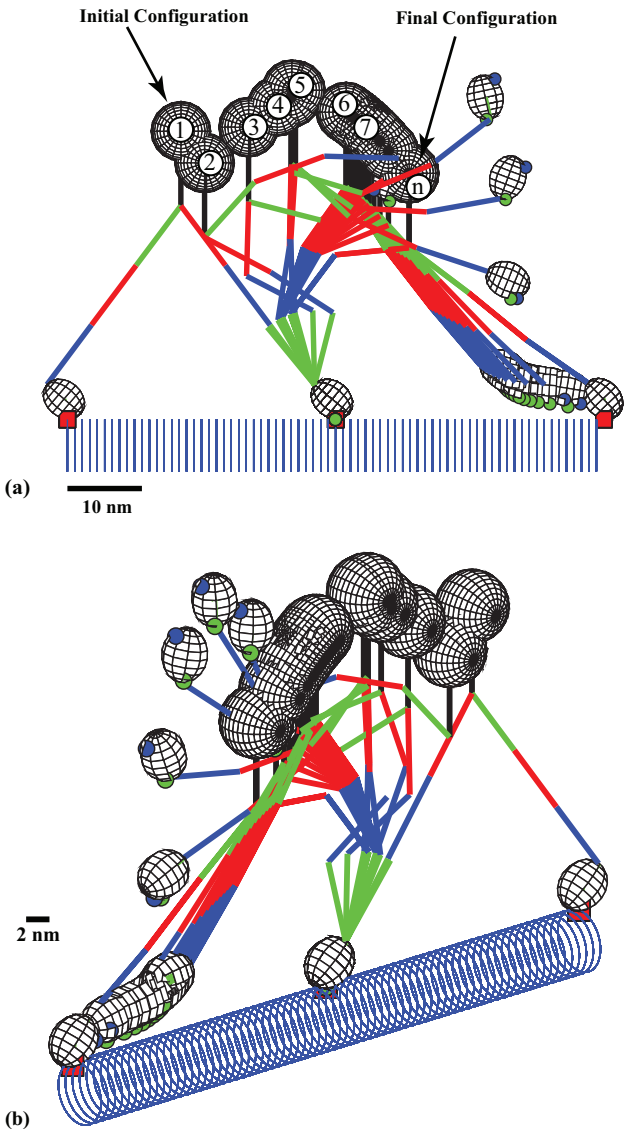

Figure 4.4. Deterministic single step locomotion of 3D mechanical model of flexible myosin V (a) 2D view (b) 3D view. The numbers show the sequence of myosin v's snapshots. The neck's segments are shown by three different colors (red, blue, and green). The blue and green circles on the heads are location of the binding site and the candidate contact point, respectively.

Brownian motion plays important role in locomotion of particles at the nanoscale. To examine the effect of the thermal motion on locomotion of myosin V, random forces

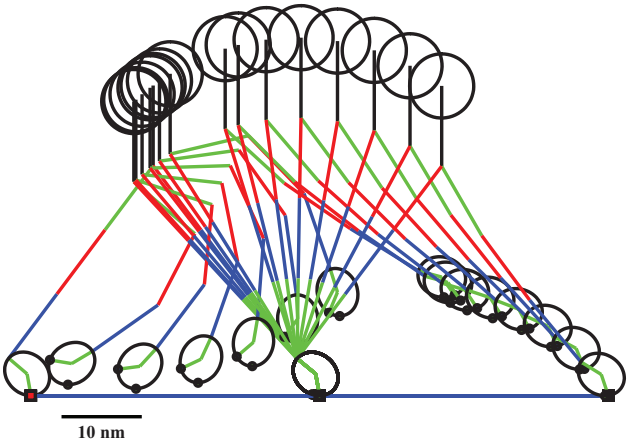

Figure 4.5. Deterministic single step locomotion of 2D mechanical model of flexible myosin V [6, 8, 9].

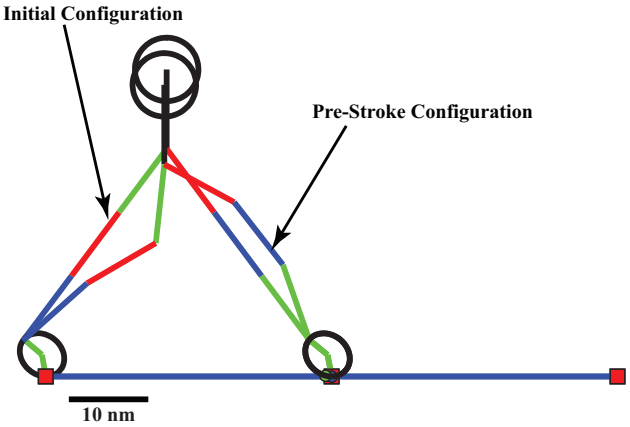

Figure 4.6. Initial and pre-stroke configurations of myosin V obtained by 3D model. The neck domains are straight at initial condition but they will bend in respond to the conformational forces. This perfectly matches with the experimental observation in [211].

are added to the model. They are modeled as Gaussian white noise and kept constant during a single time step. All forces used in the deterministic stepping are active during the simulation of random stepping. Figure 4.7 shows snapshots of the random motion of myosin V during a single step.

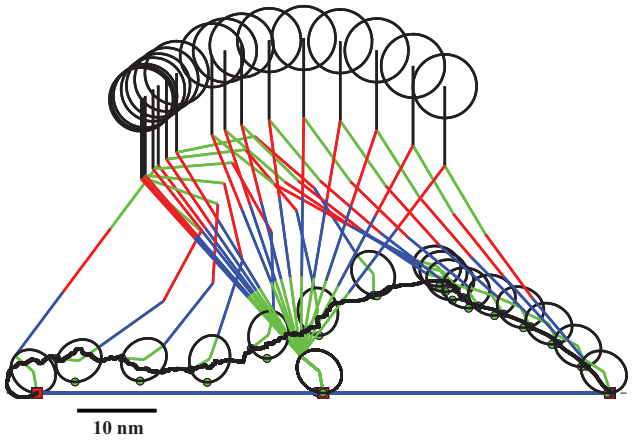

Figure 4.7. Random single step locomotion of 2D mechanical model of flexible myosin V. The black path shows the complete trajectory of the binding site (blue circle) on the trailing head during a single step.

The detailed motion of the binding site on the trailing head is shown as the black path in Fig. 4.7. The model predicts a reduced effect of random forces yielding a motion that is nearer to the deterministic motion examined in Fig. 4.5. It can be explained by this fact that the mass properties attenuate the effect of Brownian motion, allowing for random-deterministic locomotion which facilitates stepping and docking, as shown in Fig. 4.7. Indeed, this is in agreement with the widely-accepted assumption that motor protein locomotion is a combination of random and deterministic behaviors.

4.5 Conclusions

This dissertation proposes a multiscale approach for dynamic modeling and simulation of flexibility in myosin V. The proposed approach imposes a modification to the original multiscale dynamic modeling approach, developed in section 3.2 [1–5], in order to address the issue of adding flexibility to the mechanical model of molecular motors. The key result of the original approach was that the generalized active

forces can be scaled to bring them into proportion with the inertial terms; that leads to retention of the mass properties in contract to the widely used approaches which neglect them [41, 43]. In addition, the original approach correctly predicts the physical characteristics, the reduction in viscosity [129, 130] and the underdamped behavior [200], involved in dynamics of molecular motors at the nanoscale.

The current work adds an extra scaling factor to the original approach that helps to bring all generalized active forces with different orders of magnitude into proportion with inertial terms. The proposed approach was examined once using a simplified 2D finite segment model of myosin V in [6]. Herein, a 3D finite segment model is developed in order to accurately predict the movement of myosin V. There is a general agreement between the results obtained by both the original and the modified approaches. However, the flexibility of the neck domains increases the oscillation of the head domains during docking in compared with the rigid model. In addition, the neck connected to the trailing of the flexible model deforms during stepping which was ignored in the rigid model. Moreover, the 3D finite segment model shows two extra behaviors in compared with the 2D finite segment model which are the bending in the leading neck and the upper load movement of the trailing head. These behaviors have been experimentally witnessed in [211]. The unique advantage of the original approach, the reduction in the simulation run time, is still remained in the modified one even with adding flexibility to the model.

Chapter 5

Numerical Simulation

5.1 Introduction

Coarse-grained mechanical models have been developed in order to improve limitations involved in proteins model based on the classical molecular dynamics including, the huge computational efforts and simulation in limited time and space. The coarse graining process carried out by imposing configuration (holonomic) and motion (non-holonomic) constraints to the molecular dynamics of mechanical models, explicitly or implicitly, in order to eliminate degrees-of-freedom (DOF) [55]. Most of three dimensional (3D) coarse-grained models of motor proteins consider spatial position of rigid bodies in an elastic network model (ENM); however, 3D rotational properties of them are omitted or replaced by a simple rotation [38, 43, 153]. However, description of the kinematics and dynamics of a multibody systems in terms of the joint space's coordinates (rotational), instead of the spatial space's coordinates (positional), helps to reduce the number of required generalized coordinates.

In recent years, quaternions have been quite narrowly used to describe the configuration (i.e. position and orientation) of molecules, protein structures, and biopolymers [212–217]. However, quaternion-based descriptions can handle several orientation problems arise in molecular modeling [212], but the satisfaction of the normality constraint between quaternions creates difficulty during integration and simulation of dynamics of molecular models. In other words, using quaternions for describing the orientation of rigid bodies in a mechanical multibody system leads to an extra set of constraints in addition to other ones imposed to it. To avoid constraints treatment,

kinematics and dynamics of multibody systems have been developed based on the quaternions algebra that converts equations of motion from the regular 3D Cartesian space to the four dimensional (4D) quaternion space [154–156, 159–161, 218–223]. In many cases, the combination of positional and rotational generalized coordinates are required for describing kinematics of a dynamic system, therefore, the dual quaternions [162, 163, 224, 225], which includes 8 parameters with two constraints, was introduced to describe simultaneously the position and orientation of a rigid body. Modeling a super molecule, such as motor proteins, with too many degrees-of-freedom (DOF) and on the fly constraints by using quaternions or dual quaternions algebra leads to a complicated system of equations. Therefore, effective analytical and numerical techniques are required to address modeling and simulation of dynamic multibody systems subjected to different constraints. The most frequently used approaches are the method of Lagrange multiplier [162], the projecting constraints [166], and the symbolic constraint embedding [167, 168]. The two first methods are based on simultaneous solving equations of motion and constraints equations as a differential algebraic equations (DAEs). Drifting and stabilization issues involved in the DAE solvers. However, the constraints embedding method addresses these issues by reducing equations of motion into a minimal form of ordinary differential equations (ODEs) [167].

This chapter presents a new numerical technique for handling constraints involved in dynamic modeling of mechanical model of processive motor proteins using rigid multibody dynamics. The proposed model is an extension of the two dimensional (2D) mechanical model [2] into a 3D one, to reach more realistic results match with experimental data. This new model uses ball-and-socket joints between different portions of the protein's mechanical model to allow 3D rotation. Euler parameters, a unit quaternions, are used to model the orientation of bodies in order to eliminate sin-

gularities in the description. Other 3D Euler parameters models have been proposed based on quaternion algebra in [154–156]. The new mechanical model involves holonomic and on the fly non-holonomic constraints due to the extraneous coordinates in the Euler parameters and impact-contact with the substrate, respectively. The proposed computational strategy is addressed simulation of the multibody system with these changing constraints. The proposed modeling and simulation approach does not depend on quaternion algebra, but uses a numerical constraint-based algorithm to eliminate the extraneous coordinates. In order to accomplish this, the minimal form of equations of motion is obtained for a general multibody system using a numerical constraint embedding methods. The constraint-embedded form of the widely-accepted overdamped [39,40,43,44,62,67,71,76,77,83–86,90,92,95,96,99, 100,103,104,109,110,119,120,122–125] and the proposed underdamped [1–4,6,8,9] models are derived in appendix C. This is a new approach to simulating models involving Euler parameters that easily allows the inclusion of other conditions such as contact and impact, non-penetration constraints.

The overall process of simulation of a 3D mechanical model of motor proteins with changing constraints, as shown in Fig. 5.1, is presented in this section. Here it is assumed that the equations of motion, in (3.1), have been expressed as a system of first order differential equations in order to integrate them. This can be accomplished using a simple transformation such as

$$\dot{\mathbf{q}} \;=\; \mathbf{p} \qquad \ddot{\mathbf{q}} \;=\; \dot{\mathbf{p}} \tag{5.1}$$

such that

$$\dot{\mathbf{x}}(t) = \begin{bmatrix} \dot{\mathbf{q}}(t) \\ \\ \dot{\mathbf{p}}(t) \end{bmatrix} = \begin{bmatrix} \mathbf{p}(t) \\ \\ M^{-1}\left(\sum \mathbf{\Gamma} - \mathbf{C}\right) \end{bmatrix}. \tag{5.2}$$

Nominally, at each time step $\dot{\mathbf{x}}(t)$ is calculated and used to increment $\mathbf{x}(t)$ yielding $\mathbf{x}(t + \Delta t)$. The calculation of $\dot{\mathbf{x}}(t)$ is modified here to enforce the constraints. The normality condition of Euler parameters creates a holonomic constraint which must be always satisfied during simulation, while the non-penetration condition, as a non-holonomic constraint, should be considered at the contact event. The holonomic and non-holonomic constraints will be introduced in sections 5.2 and 5.3, respectively.

Herein, the idea is to enforce the constraints to be satisfied implicitly in the reduced form of equations of motion. This means that the differential form of the constraints, which relates the dependent and independent generalized speeds and accelerations, are included in the differential equations that present the dynamics of motor proteins. Numerical integration of the constrained dynamic model satisfies the differential form of the constraints spontaneously that leads to fulfillment of the algebraic form indirectly. Matlab's `ode45`, an adaptive numerical integrator, was used to perform the numerical integration of minimal form of equations of motion.

The procedure of the proposed algorithm, as shown in Fig. 5.1, includes two internal numerical constraints embedding steps. The first step belongs to addressing extraneous coordinates due to using Euler parameters. After the first reduction, the status of contact between protein's heads and the substrate is checked. Matlab's `ode45` function features an event function that was used to find the times when the head(s) came into contact with the actin filament. If any contact was detected by the event function, the simulation is stopped, then the second step of numerical reduction related to the appropriate non-penetration constraints is applied, and the simulation is restarted at the same time and position/orientation using the new velocities. Otherwise, the modified generalized speeds by the holonomic constraints directly are fed to dynamic equations. This numerical reduction helps to decrease the complications involved in the symbolic constraints embedding of huge molecular models.

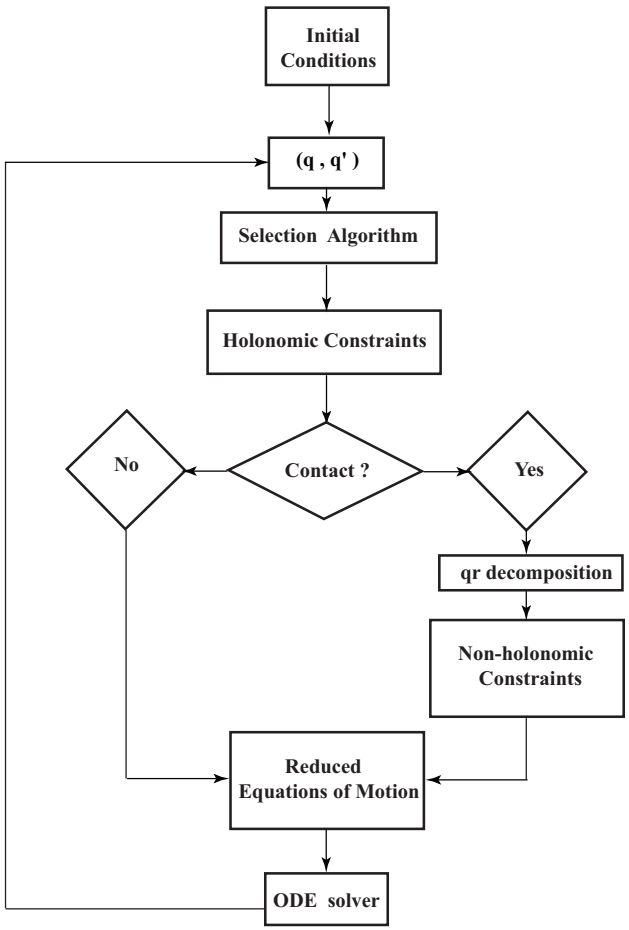

Figure 5.1. The process of simulation for the dynamic modeling of motor protein .

For the sake of simplicity, a 3D double pendulum was used, as a case-study, in order to show the effectiveness of the proposed technique. The numerical technique was tested in two different conditions, the first being implementation of the online constraint embedding of holonomic constraints for the free rotation of the double pendulum. The second being the extension of the numerical technique for the case of rotation with possibility of contact-impact as non-holonomic constraints.

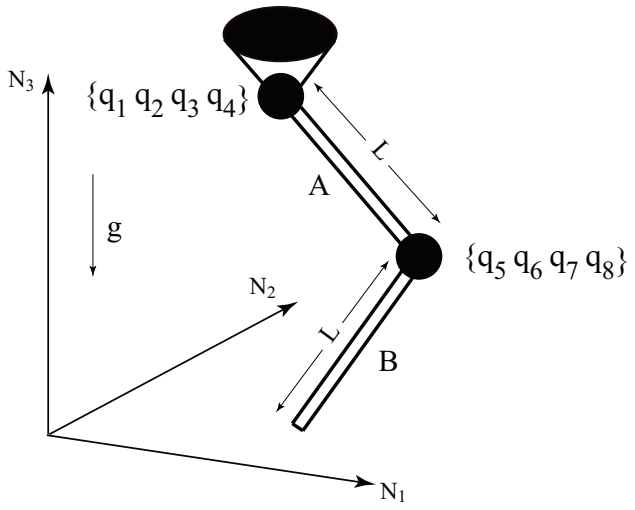

Figure 5.2. 3D double pendulum with ball-and-socket joints. The identical links are considered as a cylinder with length L, radius r, mass m, and moment of inertia $\{I_{xx}, I_{yy}, I_{zz}\}$.

5.2 Holonomic Constraints

The 3D pendulum in Fig. 5.2 can be used to illustrate the use of Euler parameters. The rotation of each frictionless, ball-and-socket joint is described using 4-tuples of coordinates, $\{q_1, q_2, q_3, q_4\}$ and $\{q_5, q_6, q_7, q_8\}$, which represent two sets of Euler parameters, even though the pendulum only has 6 DOF. The normality constraint, and its derivative, for the first set are,

$$q_1^2 + q_2^2 + q_3^2 + q_4^2 = 1 \qquad\qquad \dot{q}_1\ q_1 + \dot{q}_2\ q_2 + \dot{q}_3\ q_3 + \dot{q}_4\ q_4 = 0 \tag{5.3}$$

In order to reduce the equations of motion, this constraint is used to eliminate the generalized speed and acceleration associated with one of the Euler parameters. This is accomplished by solving for it in terms of the others, for example consider the case where q_1 is selected as the dependent coordinate:

$$\dot{q}_1 = -\frac{1}{q_1}(\dot{q}_2 q_2 + \dot{q}_3 q_3 + \dot{q}_4 q_4) \tag{5.4}$$

Extending (5.4) to all sets of 4-tuple generalized coordinates used in the model, the desired form of the constraints is obtained;

$$\dot{\mathbf{q}}_p = C_{pm}\,\dot{\mathbf{q}}_m \tag{5.5}$$

where $m+p$ equals to the total number of generalized coordinates, $C_{pm} \in \mathbb{R}^{p\times m}$ is the matrix that relates independent and dependent generalized speeds. $\dot{\mathbf{q}}_p \in \mathbb{R}^{p\times 1}$ and $\dot{\mathbf{q}}_m \in \mathbb{R}^{m\times 1}$ are vectors of dependent and independent generalized speeds, respectively, obtained by decomposing $\dot{\mathbf{q}}$ using the permutation matrix P.

$$\begin{bmatrix} \dot{\mathbf{q}}_m \\ \dot{\mathbf{q}}_p \end{bmatrix} = P^T\,\dot{\mathbf{q}} \tag{5.6}$$

Differentiating (5.5), yields;

$$\ddot{\mathbf{q}}_p = C_{pm}\ddot{\mathbf{q}}_m + \dot{C}_{pm}\dot{\mathbf{q}}_m \tag{5.7}$$

where $\ddot{\mathbf{q}}_p$ and $\ddot{\mathbf{q}}_m$ are time derivatives of the dependent and independent generalized speeds respectively, $\dot{C}_{pm}$ is time derivative of the matrix in (5.5). However, if $q_1 \to 0$ this scheme will become singular and therefore so will C_{pm}. In order to avoid this singularity problem, the dependent parameter must be chosen wisely. *Because the source of the singularity is known, a partitioning criterion can be developed that does not require extensive computations or the mass matrix inverse.* Here three methods, discussed in the next section, are considered.

5.2.1 Selection Algorithm

Here three different approaches towards choosing a dependent parameter are explored. The first method is based on selecting the parameter which has the maximum absolute value as shown in Fig. 5.3a. This prevents the denominator in (5.4) from equaling zero, but the dependent coordinate constantly switches. This causes

dynamic inconsistencies which are revealed by evaluating the work-energy theorem. A second approach, shown in Fig. 5.3b, does not switch the dependent coordinate unless the condition number of the mass matrix becomes unacceptably large, or the denominator in (5.4) approaches zero.

The third approach uses an event function to find the times when the mass matrix's condition number exceeds a predetermined threshold, as shown in Fig. 5.4. The event function then stops the numerical integration, the current dependent parameter is switched to the one with the largest absolute value, and the integration is restarted.

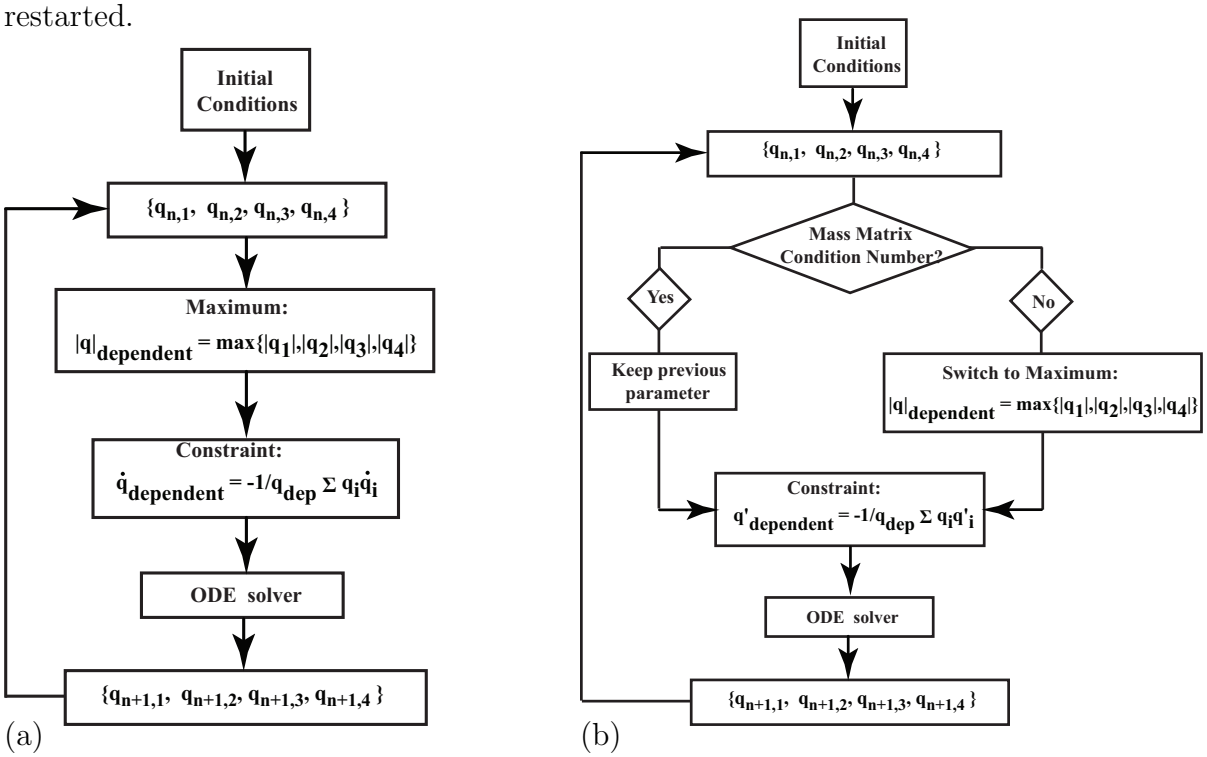

Figure 5.3. Overall process of selection of dependent parameter by (a) the first method, (b) the second method.

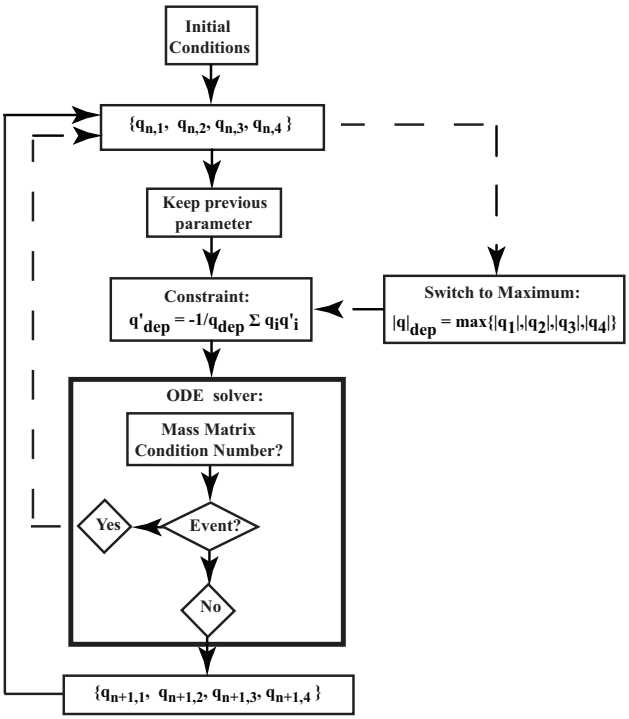

Figure 5.4. Overall process of selection of dependent parameter by the third method.

5.2.2 Error Analysis

The effect of switching on error propagation in a single time step of numerical integration, based on the fourth order Runge-Kutta (RK4) algorithm, is examined by using a simple analytical error analysis. A single time step is examined without and with switching of the dependent parameter as shown in Tables 5.1 and 5.2, respectively.

The Runge-Kutta family of ODE solvers is a popular and robust numerical integration algorithm which evaluates $\dot{q}$ at different stages and uses these values to fit a polynomial curve to the exact solution over the range of one time step [171]. For example, RK4 which is shown in (5.10), uses a weighted average of four values of the

derivative in a time step to fit a fourth order polynomial which has the general form for each q_i, for $\{i = 1, 2, 3, 4\}$, of

$$q_{n+1} = q_n + \frac{1}{6}\left(k_1 + 2k_2 + 2k_3 + k_4\right) \qquad t_{n+1} = t_n + h \tag{5.8}$$

$$k_1 = h\ \dot{q}_n(t_n, q_n) \qquad k_4 = h\ \dot{q}_n\left(t_n + h, q_n + k_3\right) \tag{5.9}$$

$$k_2 = h\ \dot{q}_n\left(t_n + \tfrac{h}{2}, q_n + \tfrac{k_1}{2}\right) \qquad k_3 = h\ \dot{q}_n\left(t_n + \tfrac{h}{2}, q_n + \tfrac{k_2}{2}\right) \tag{5.10}$$

where $q_n = q_i(t_n)$, h is the time step, and $\{k_1, k_2, k_3, k_4\}$ are changes in $q_i(t_n)$ based on the derivative at the initial, middle (two times), and final time interval points (stages). Therefore, it is possible that switching occurs several times during a single step. The error of the i^{th} Euler parameter at the stage k_j is expressed by ϵ_{ji}. This error propagates through the later stages as follows:

$$\epsilon_{j+1,i} \ = \ \varepsilon_{j+1,i} \ + \ \alpha_j\ \epsilon_{ji} \tag{5.11}$$

where $\varepsilon_{j+1,i}$ is the error due to the current stage calculation, and α_j is a positive coefficient which is less than one under the assumption that the contribution of the error from the previous step is reduced by a factor, see (5.10). The error of the dependent parameter at each stage is determined by the error in the independent parameters using (5.4). Table 5.1 is developed in order to show the propagation of error in the non-switching case. In Table 5.1, the dependent parameter (i.e. the first parameter) is fixed during the four stages; therefore, its error will be determined by the independent parameter's errors at each stage. This can be seen by examining the total error for q_1, the dependent coordinate, at the next time step, $n + 1$, designated as $\xi_{n+1,1}$:

$$\xi_{n+1,1} \ = \ \xi_{n,1} \ + \ \frac{1}{6}\left(\epsilon_{11} + 2\epsilon_{21} + 2\epsilon_{31} + \epsilon_{41}\right) \tag{5.12}$$

Table 5.1. Error Propagation in One Step-size of Integration without Switching

	k_1	k_2	k_3	k_4
q_1	$\dfrac{\epsilon_{12}+\epsilon_{13}+\epsilon_{14}}{q_1}$	$\dfrac{\epsilon_{22}+\epsilon_{23}+\epsilon_{24}}{q_1}$	$\dfrac{\epsilon_{32}+\epsilon_{33}+\epsilon_{34}}{q_1}$	$\dfrac{\epsilon_{42}+\epsilon_{43}+\epsilon_{44}}{q_1}$
q_2	ϵ_{12}	$\epsilon_{22}=\varepsilon_{22}+\alpha_2\epsilon_{12}$	$\epsilon_{32}=\varepsilon_{32}+\alpha_3\epsilon_{22}$	$\epsilon_{42}=\varepsilon_{42}+\alpha_4\epsilon_{32}$
q_3	ϵ_{13}	$\epsilon_{23}=\varepsilon_{23}+\alpha_2\epsilon_{13}$	$\epsilon_{33}=\varepsilon_{33}+\alpha_3\epsilon_{23}$	$\epsilon_{43}=\varepsilon_{43}+\alpha_4\epsilon_{33}$
q_4	ϵ_{14}	$\epsilon_{24}=\varepsilon_{24}+\alpha_2\epsilon_{14}$	$\epsilon_{34}=\varepsilon_{34}+\alpha_3\epsilon_{24}$	$\epsilon_{44}=\varepsilon_{44}+\alpha_4\epsilon_{34}$

using (5.8). Substituting the values for ϵ_{ji} from Table 5.1 into (5.12) and eliminating higher order terms yields

$$\begin{aligned}\xi_{n+1,1} \;=\; \xi_{n,1} + \tfrac{1}{6q_1}((1+2\alpha_2)(\epsilon_{12}+\epsilon_{13}+\epsilon_{14})+ \\ 2(1+\alpha_3)(\varepsilon_{22}+\varepsilon_{23}+\varepsilon_{24}) + (2+\alpha_4)(\varepsilon_{32}+\varepsilon_{33}+\varepsilon_{34}) + (\varepsilon_{42}+\varepsilon_{43}+\varepsilon_{44}))\end{aligned} \tag{5.13}$$

where the effect of the error from the independent coordinates enters through ϵ_{44}, ϵ_{34}, etc.

However, calculating the total error for a dependent coordinate, such as q_4, using (5.8) yields

$$\xi_{n+1,4} \;=\; \xi_{n,4} + \frac{1}{6}\left((1+2\alpha_2)\epsilon_{14} + 2(1+\alpha_3)\varepsilon_{24} + (2+\alpha_4)\varepsilon_{34} + \varepsilon_{44}\right) \tag{5.14}$$

which shows that the error in the independent parameter is not affected by the other parameters in the non-switching case.

Now, consider a worst-case scenario, where switching occurs at every stage, shown in Table 5.2. Every parameters' error is affected by every other, in contrast to non-switching case. Similar to (5.13) and (5.14), the total error at the end of a step can be expressed as

$$\xi_{n+1,1} = \xi_{n,1} + \frac{(1+2\alpha_2)(\epsilon_{12}+\epsilon_{13}+\epsilon_{14})}{6q_1} + \frac{2(1+\alpha_3)\varepsilon_{21} + (2+\alpha_4)\varepsilon_{31} + \varepsilon_{41}}{6} \tag{5.15}$$

Table 5.2. Error Propagation in One Step-size of Integration with Switching

	k_1	k_2	k_3	k_4
q_1	$\frac{(\epsilon_{12}+\epsilon_{13}+\epsilon_{14})}{q_1}$	$\epsilon_{21}=\varepsilon_{21}+\alpha_2\epsilon_{11}$	$\epsilon_{31}=\varepsilon_{31}+\alpha_3\epsilon_{21}$	$\epsilon_{41}=\varepsilon_{41}+\alpha_4\epsilon_{31}$
q_2	ϵ_{12}	$\frac{(\epsilon_{21}+\epsilon_{23}+\epsilon_{24})}{q_2}$	$\epsilon_{32}=\varepsilon_{32}+\alpha_3\epsilon_{22}$	$\epsilon_{42}=\varepsilon_{42}+\alpha_4\epsilon_{32}$
q_3	ϵ_{13}	$\epsilon_{23}=\varepsilon_{23}+\alpha_2\epsilon_{13}$	$\frac{(\epsilon_{31}+\epsilon_{32}+\epsilon_{34})}{q_3}$	$\epsilon_{43}=\varepsilon_{43}+\alpha_4\epsilon_{33}$
q_4	ϵ_{14}	$\epsilon_{24}=\varepsilon_{24}+\alpha_2\epsilon_{14}$	$\epsilon_{34}=\varepsilon_{34}+\alpha_3\epsilon_{24}$	$\frac{(\epsilon_{41}+\epsilon_{42}+\epsilon_{43})}{q_4}$

$$\begin{aligned}\xi_{n+1,4} &= \xi_{n,4}+\tfrac{1}{6q_4}(\varepsilon_{41}+\varepsilon_{42}+\varepsilon_{43}+\varepsilon_{34}+(1+\alpha_4)(\varepsilon_{31}+\varepsilon_{32}+\varepsilon_{23})+ \\ &\quad (1+\alpha_3+\alpha_4)(\varepsilon_{21}+\varepsilon_{24}+\epsilon_{12})+(1+\alpha_2+\alpha_3+\alpha_4)(\epsilon_{13}+\epsilon_{14}))\end{aligned} \tag{5.16}$$

However, Blajer in [165] suggests that the switching from one set of independent coordinates to another does not propagate integration errors but the analytical error analysis of the two different cases, in (5.13)-(5.16), shows that switching in the middle of one step-size increases the error of all parameters in compared with the non-switching case. This implies that the selection algorithm should reduce the amount of switching, especially in the middle of a time step, in order to produce more accurate results. It will be shown that the third approach in Fig. 5.4 produces the least amount of switching.

5.3 Non-Holonomic Constraints

Another type of constraint in the model is *non-holonomic* constraint related to contact-impact which can be interpreted as a non-penetration condition. The normal velocity of contact points must equal zero when the multibody systems contact to obstacles in order to ensure that the systems does not penetrate the obstacle. The

velocity of contact points are related to the generalized speeds through the contact Jacobian matrix,

$$\boldsymbol{\vartheta} \;=\; \begin{bmatrix} \boldsymbol{v}_c \\ \boldsymbol{\omega}_c \end{bmatrix} = J_c\, \dot{\mathbf{q}} \tag{5.17}$$

where $\boldsymbol{v}_c$ and $\boldsymbol{\omega}_c$ are linear velocity of contact points and angular velocity of its body, and J_c is the contact Jacobian matrix. Now, (5.17) is used to find an appropriate form of constraint equation, similar to (5.5), which relates the dependent generalized speeds to the independent generalized speeds. First, the holonomic constraint is used to eliminate the dependent generalized speeds associated to Euler parameters, so $PP^T = I$ is multiplied at the right hand side of (5.17).

$$\boldsymbol{\vartheta} \;=\; J_c\, PP^T\, \dot{\mathbf{q}} = \begin{bmatrix} J_{cm} & J_{cp} \end{bmatrix} \begin{bmatrix} \dot{\mathbf{q}}_m \\ \dot{\mathbf{q}}_p \end{bmatrix} = J_{cm}\, \dot{\mathbf{q}}_m + J_{cp}\, \dot{\mathbf{q}}_p \tag{5.18}$$

where $J_{cp} \in \mathbb{R}^{s\times p}$ and $J_{cm} \in \mathbb{R}^{s\times m}$ are determined by decomposition of the contact Jacobian matrix using the permutation matrix P, s is the number of contact point's velocity components which are constrained. Substitute (5.5) into (5.18), yields.

$$\boldsymbol{\vartheta} \;=\; \widetilde{J}_c\, \dot{\mathbf{q}}_m \tag{5.19}$$

where,

$$\widetilde{J}_c = J_{cm} + J_{cp}\, C_{pm}$$

qr decomposition is used to split the reduced Jacobian matrix of (5.19) corresponding to the dependent and independent generalized speeds as follow;

$$\widetilde{J}_c\, E \;=\; Q\, R \;=\; Q \begin{bmatrix} R_s & R_r \end{bmatrix} \;=\; \begin{bmatrix} \widetilde{J}_{cs} & \widetilde{J}_{cr} \end{bmatrix} \tag{5.20}$$

where $s + r = m$, $E \in \mathbb{R}^{m\times m}$ is the permutation matrix, $Q \in \mathbb{R}^{s\times s}$ is an orthogonal matrix, and $R \in \mathbb{R}^{s\times m}$ is upper-triangular matrix that includes $R_s \in \mathbb{R}^{s\times s}$ and $R_r \in \mathbb{R}^{s\times r}$. The (5.19) is rewritten using the identity matrix EE^T

$$\boldsymbol{\vartheta} \;=\; \widetilde{J}_c\,(E\,E^T)\,\dot{\mathbf{q}}_m = \left[\begin{array}{cc} \widetilde{J}_{cs} & \widetilde{J}_{cr} \end{array}\right] \left[\begin{array}{c} \dot{\mathbf{q}}_s \\ \dot{\mathbf{q}}_r \end{array}\right] \;=\; \widetilde{J}_{cs}\,\dot{\mathbf{q}}_s + \widetilde{J}_{cr}\,\dot{\mathbf{q}}_r \tag{5.21}$$

The unknown post-impact velocity $\boldsymbol{\vartheta}(t+\epsilon)$ in (5.21) is determined by using Newton's coefficient of restitution (COR) as follow;

$$\boldsymbol{\vartheta}(t+\epsilon) = -e\;\boldsymbol{\vartheta}(t) \tag{5.22}$$

where $\boldsymbol{\vartheta}(t)$ is pre-impact velocity and e is a positive number less than one, substituting (5.22) into (5.21) yields

$$-e\;\boldsymbol{\vartheta}(t) \;=\; \widetilde{J}_{cs}\,\dot{\mathbf{q}}_s(t+\epsilon) + \widetilde{J}_{cr}\,\dot{\mathbf{q}}_r(t+\epsilon) \tag{5.23}$$

Equation (5.23) just provides s equations, equal to the number of contact points, while it is less than the number of unknowns, $m = r + s$. To address this, the classical rigid body impact dynamics can be used to provide enough equations. A definite integration of the equations of motion over a tiny period of time yields,

$$\int_t^{t+\epsilon} (M_m\ddot{\mathbf{q}}_m \;+\; \mathbf{C}_m(\mathbf{q},\dot{\mathbf{q}}) \;+\; \boldsymbol{g}_m)\mathrm{d}t \;=\; \int_t^{t+\epsilon} (\widetilde{J}_c^T\;\mathbf{F} \;+\; \boldsymbol{\Gamma}_m)\mathrm{d}t \tag{5.24}$$

where only the impact forces survive

$$M_m(\dot{\mathbf{q}}_m(t+\epsilon) \;-\; \dot{\mathbf{q}}_m(t)) \;=\; \widetilde{J}_c^T\;\mathbf{p} \tag{5.25}$$

where $\mathbf{p}$ is impulse force, and by using the permutation matrix E, (5.25) is split up to the dependent and independent parts.

$$\begin{aligned} M_{rr}(\dot{\mathbf{q}}_r(t+\epsilon) - \dot{\mathbf{q}}_r(t)) + M_{rs}(\dot{\mathbf{q}}_s(t+\epsilon) - \dot{\mathbf{q}}_s(t)) \;&=\; J_{cr}^T\;\mathbf{p} \\ M_{sr}(\dot{\mathbf{q}}_r(t+\epsilon) - \dot{\mathbf{q}}_r(t)) + M_{ss}(\dot{\mathbf{q}}_s(t+\epsilon) - \dot{\mathbf{q}}_s(t)) \;&=\; J_{cs}^T\;\mathbf{p} \end{aligned} \tag{5.26}$$

eliminating the $\mathbf{p}$ between the equations in ((5.26)) yields,

$$(M_{rr} + C_{sr}^T\ M_{sr})\dot{\mathbf{q}}_r(t+\epsilon) + (M_{rs} + C_{sr}^T\ M_{ss})\dot{\mathbf{q}}_s(t+\epsilon) = \\ (M_{rr} + C_{sr}^T\ M_{sr})\dot{\mathbf{q}}_r(t) + (M_{rs} + C_{sr}^T\ M_{ss})\dot{\mathbf{q}}_s(t) \tag{5.27}$$

where

$$C_{sr} = -(\widetilde{J}_{cs})^{-1}\,\widetilde{J}_{cr}$$

By simultaneous solving (5.23) and (5.27), the unique solution of the post-impact generalized speeds is obtained. If status after impact was contact, the equations of motion should be reduced according to the non-holonomic constraints of contact that satisfies the non-penetration condition. Thus, by vanishing the contact velocity in (5.23), the dependent generalized speeds, $\dot{\mathbf{q}}_s$, are obtained in terms of the independent generalized speeds, $\dot{\mathbf{q}}_r$;

$$\dot{\mathbf{q}}_s = C_{sr}\,\dot{\mathbf{q}}_r \tag{5.28}$$

where A_{sr} is the same matrix as defined in (5.27). In addition, the time derivative of the independent generalized speeds is obtained by differentiation of (5.28)

$$\ddot{\mathbf{q}}_s = C_{sr}\,\ddot{\mathbf{q}}_r + \dot{C}_{sr}\,\dot{\mathbf{q}}_r \tag{5.29}$$

where

$$\dot{C}_{sr} = -(\widetilde{J}_{cs})^{-1}\,(\dot{\widetilde{J}}_{cs}\,C_{sr} + \dot{\widetilde{J}}_{cr})$$

By this method, here is no need to impact or contact analysis, including determination of contact forces, during contact events while the *non-holonomic* constraints are used.

5.4 Online Constraint Embedding in Dynamic Modeling and Simulation

The general form of equations of motion for multibody systems is given below,

$$\underbrace{M(\mathbf{q})\ \ddot{\mathbf{q}}\ +\ \mathbf{C}(\dot{\mathbf{q}},\mathbf{q})}_{\text{generalized inertia forces}} = \underbrace{\mathbf{\Gamma}(\dot{\mathbf{q}},\mathbf{q})}_{\text{generalized active forces}} \tag{5.30}$$

where $\mathbf{q}$ contains the generalized coordinates, and $\dot{\mathbf{q}}$ and $\ddot{\mathbf{q}}$ are its time derivatives of generalized velocity and acceleration. The term $M(\mathbf{q})$ is the mass matrix. $\mathbf{C}(\dot{\mathbf{q}}, \mathbf{q})$ is nonlinear terms including, centrifugal-Coriolis terms. $\mathbf{\Gamma}$ is the external forces acting on the model including gravity, friction, contact forces.

The matrix, C_{pm}, from (5.5) can be used to combine the dependent and independent parts of (5.30) to obtain the minimal form of the equations of motion [168],

$$\widetilde{\mathbf{F}}_m - \widetilde{\mathbf{F}}^*_m = \mathbf{F}_m - \mathbf{F}^*_m + C^T_{pm}\left(\mathbf{F}_p - \mathbf{F}^*_p\right) = \mathbf{0} \tag{5.31}$$

where F and F^* are *generalized active forces* and *generalized inertia forces*, respectively.

The permutation matrix in (5.6), P, is invoked to decompose the (5.30) into dependent and independent parts.

$$\begin{aligned} \left(P^T M P\right)\left(P^T \ddot{\mathbf{q}}\right) + P^T \mathbf{C} &= P^T \mathbf{\Gamma} \\ \begin{bmatrix} M_{mm} & M_{mp} \\ M_{pm} & M_{pp} \end{bmatrix} \begin{bmatrix} \ddot{\mathbf{q}}_m \\ \ddot{\mathbf{q}}_p \end{bmatrix} + \begin{bmatrix} \mathbf{C}_m \\ \mathbf{C}_p \end{bmatrix} &= \begin{bmatrix} \mathbf{\Gamma}_m \\ \mathbf{\Gamma}_p \end{bmatrix} \end{aligned} \tag{5.32}$$

converting matrix form of (5.32) into Kane's format yields

$$\begin{aligned} \mathbf{F}_m - \mathbf{F}^*_m &= \mathbf{\Gamma}_m - M_{mm}\,\ddot{\mathbf{q}}_m - M_{mp}\,\ddot{\mathbf{q}}_p - \mathbf{C}_m = \mathbf{0} \\ \mathbf{F_p} - \mathbf{F^*_p} &= \mathbf{\Gamma}_p - M_{pm}\,\ddot{\mathbf{q}}_m - M_{pp}\,\ddot{\mathbf{q}}_p - \mathbf{C}_p = \mathbf{0} \end{aligned} \tag{5.33}$$

Plug (5.33) into (5.31) gives

$$\widetilde{M}_m\,\ddot{\mathbf{q}}_m + \widetilde{\mathbf{C}}_m = \widetilde{\mathbf{\Gamma}}_m \tag{5.34}$$

where

$$\begin{aligned} \widetilde{M}_m &= M_{mm} + M_{mp}\,C_{pm} + C^T_{pm}\,M_{pm} + C^T_{pm}\,M_{pp}\,C_{pm} \\ \widetilde{\mathbf{C}}_m &= \mathbf{C}_m + C^T_{pm}\,\mathbf{C}_p + \left(M_{mm}\,\dot{C}_{pm} + C^T_{pm}\,M_{pp}\,\dot{C}_{pm}\right)\dot{\mathbf{q}}_m \\ \widetilde{\mathbf{\Gamma}}_m &= \mathbf{\Gamma}_m + C^T_{pm}\,\mathbf{\Gamma}_p \end{aligned}$$

Notice that the contact forces involved in $\mathbf{\Gamma}$, in (5.30), are automatically eliminated in $\widetilde{\mathbf{\Gamma}}_m$.

5.5 Results

The proposed online constraint embedding method was examined on a 3D double pendulum for two different cases including, free rotation of double pendulum, and rotation with possible contact-impact which their results are presented respectively in following.

5.5.1 Free Rotation

The overall process of simulating multibody systems with holonomic constraints is shown in Fig. 5.5. The first step is the selection algorithm, section 5.2.1. Next a matrix, that relates dependent to independent coordinates, is formed from the holonomic normality constraint. This matrix is used in the constraint embedding, equation reduction, step. The reduction is performed numerically, rather than symbolically. Numerical integration of the reduced dynamic model satisfies the differential form of the constraints spontaneously and leads to fulfillment of the algebraic form indirectly. Matlab's `ode45`, an adaptive numerical integrator, is used to perform the numerical integration of the minimal form of the equations of motion.

The values of parameters and initial conditions, which are used for simulation of the 3D double pendulum, are given in Table 5.3. In order to verify the dynamic model of the 3D double pendulum during the simulation, a check function for energy consistency is defined based on the Work-Energy theorem in (5.35).

$$\text{check}_{1_i} \;=\; T_i \;-\; (T_1 + W_{1\to i}) \tag{5.35}$$

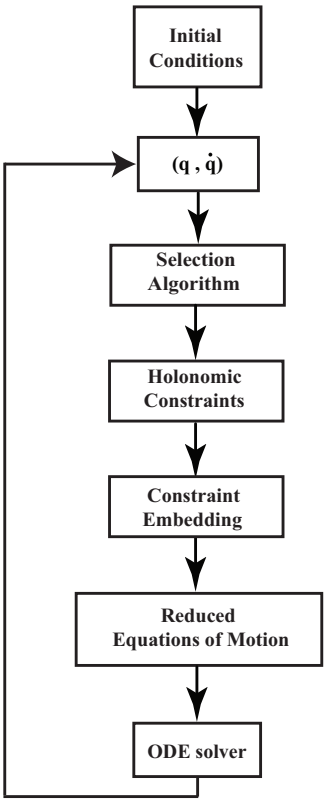

Figure 5.5. The process of simulation for the case of free rotation (just holonomic constraints).

Table 5.3. Parameters and Initial Conditions for Simulation of the 3D Double Pendulum Model in Fig. 5.2

Quantity	Value	Comment
L	$0.3\ m$	*For both links, A and B*
r	$0.05\ m$	*For both links, A and B*
g	$9.81\ \frac{m}{s^2}$	
m	$1\ kg$	*For both links, A and B*
$\{I_{xx}, I_{yy}, I_{zz}\}$	$\{0.0025, 0.0975, 0.0975\}\ kg.m^2$	*For both links, A and B*
$\{q_1, q_2, q_3, q_4\}$	$\{0.2732, 0.1815, -0.1543, 0.9320\}$	*satisfies (5.3)*
$\{q_5, q_6, q_7, q_8\}$	$\{-0.1379, 0.3589, 0.2550, 0.8872\}$	*satisfies (5.3)*
$\{\dot{q}_1, \dot{q}_2, \dot{q}_3, \dot{q}_4\}$	$\{0, 0, 0, 0\}$	*satisfies (5.3)*
$\{\dot{q}_5, \dot{q}_6, \dot{q}_7, \dot{q}_8\}$	$\{0, 0, 0, 0\}$	*satisfies (5.3)*

where T_1 and T_i are the kinetic energy at the first and the i^{th} step of integration, $W_{1\to i}$ is the work done by the generalized active forces (i.e. conservative and non-conservative) during these steps. This check function should be constant if no errors occur. Errors in the check function indicate that the amount of work done by generalized active forces is not equal to the change in kinetic energy, as stipulated by the work-energy theorem. This is a *dynamic inconsistency* generated here by switching the dependent parameter.

The results of the check function are obtained using the three different algorithms for four different time steps as shown in Fig. 5.6. The first method constantly switches, as discussed in section 5.2.1, which leads to several jumps in the check function corresponding to times when switching occurred, as shown in Fig. 5.7a. Also, the check function obtained by this algorithm is not stable against change of time step and it shifts upwards and downwards.

The switching issue is addressed by retaining the dependent parameter until the mass matrix condition number is less than a desired threshold (i.e. eliminating extra switching) in the second method as illustrated in Fig. 5.7. However, the check function's behavior is very sensitive to the time step. For example, for either very small or very large time steps, its check function's behavior is very close to the first algorithm, while for the intermediate time step, it is near to the third method. This occurs because the second algorithm still has inappropriate switching during one step of the integration.

Figure 5.6 shows that the third algorithm addresses this issue and it has the best check function results among the proposed algorithms for all time steps. The reduction of check function is caused by less switching and prevention of switching in a single step of integration as predicted by the analytical error analysis in section 5.2.1. In addition, increasing the time step, increases the check function value for all three

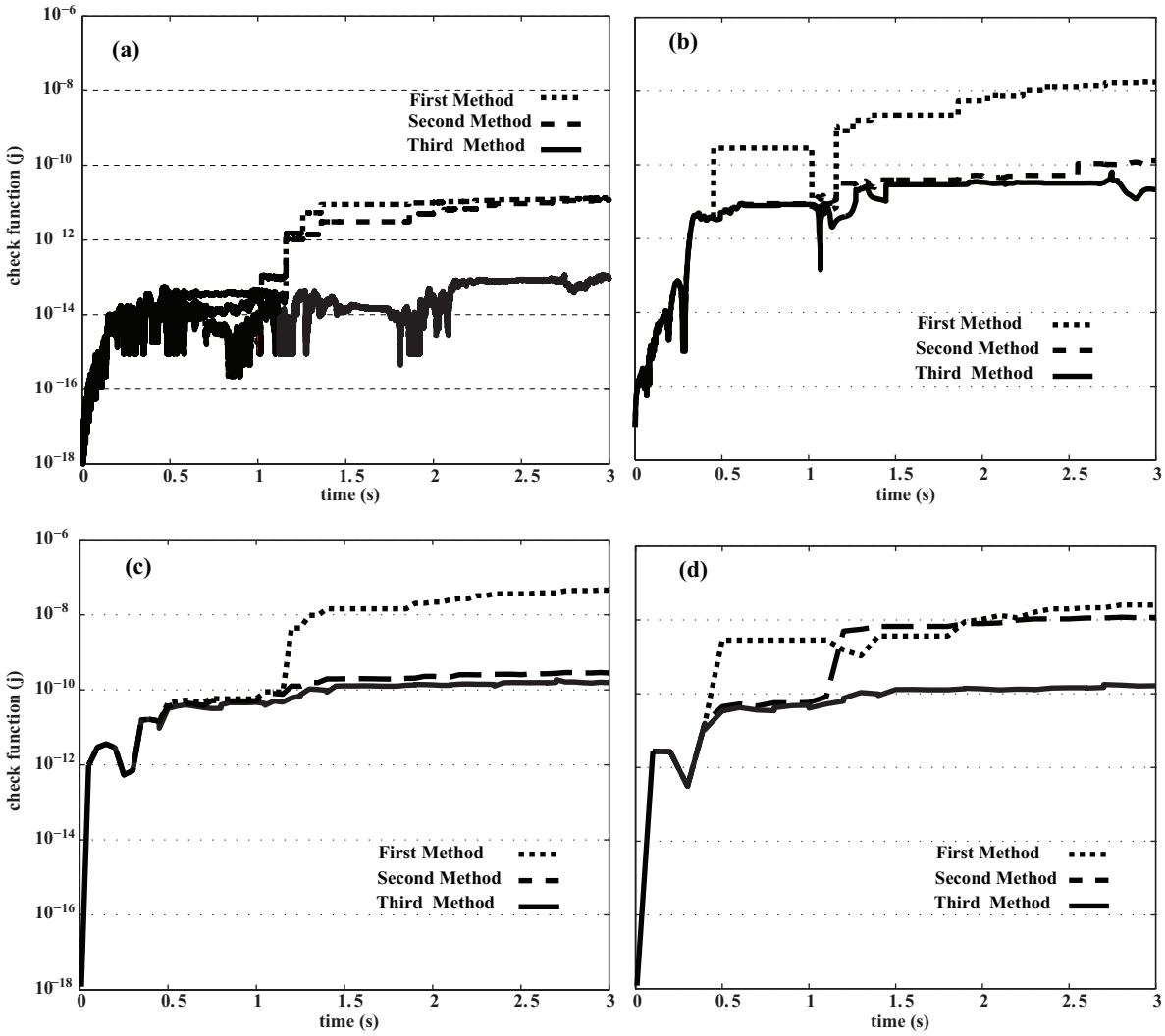

Figure 5.6. Comparison between the check functions on energy consistency obtained by the different algorithms with (a) $0.1ms$, (b) $1ms$, (c) $50ms$, and (d) $100ms$ integration time step-size and $abserr = 10^{-10}$ and $relerr = 10^{-9}$.

methods. However, the results for the third algorithm stay at an acceptable level for the different time steps whereas the other algorithms do not, which proves the robustness of the third method.

In order to compare the numerical efficiency of the proposed algorithms, the order of maximum error in energy consistency and the CPU-time of a simulation run were obtained for four integration step sizes as shown in Tables 5.4 and 5.5, respectively. A comparison of the results shows that the third method has the least

error among the proposed algorithms while its CPU-time of simulation is almost as same as the other methods. This means the third selection algorithm provides more accuracy without increasing the computational cost in compared with the other algorithms.

Table 5.4. Comparison of Order of Error in Energy Consistency of the Model Using the Proposed Algorithms

Integration step size	$\Delta t = 0.1ms$	$\Delta t = 1ms$	$\Delta t = 50ms$	$\Delta t = 100ms$
First method (J)	10^{-11}	10^{-8}	10^{-7}	10^{-7}
Second method (J)	10^{-11}	10^{-10}	10^{-10}	10^{-8}
Third method (J)	10^{-13}	10^{-11}	10^{-10}	10^{-10}

Table 5.5. Comparison of Simulation CPU-time of the Model Using the Proposed Algorithms.

Integration step size	$\Delta t = 0.1ms$	$\Delta t = 1ms$	$\Delta t = 50ms$	$\Delta t = 100ms$
First method (sec)	1114.2	115.9	14.5	13.5
Second method (sec)	1114.2	117.4	15.7	13.9
Third method (sec)	1121.1	117.4	15.9	14.0

The switching statuses of Euler parameters for the joints of the 3D pendulum using the three different selection algorithms are illustrated in Fig. 5.7. These results show that the third methods has the least switching among the selection algorithms. This is illustrated more clearly in Fig. 5.7 which shows number of times the dependent Euler parameter switched during the simulation. The solid and dashed arrows show switching for the first and second joints, respectively. The s_i labels in Fig. 5.7 indicate the chronological order of switching. The time at which s_1, $t(s_1)$, occurs is less than the time at which s_2 occurs, $t(s_2)$, or $t(s_1) < t(s_2) < t(s_3) < .... < t(s_n)$. The number

of switches in the third method, 8 and 4 times, is almost half of those in the first, 14 and 6 times, and the second, 14 and 6 times, methods.

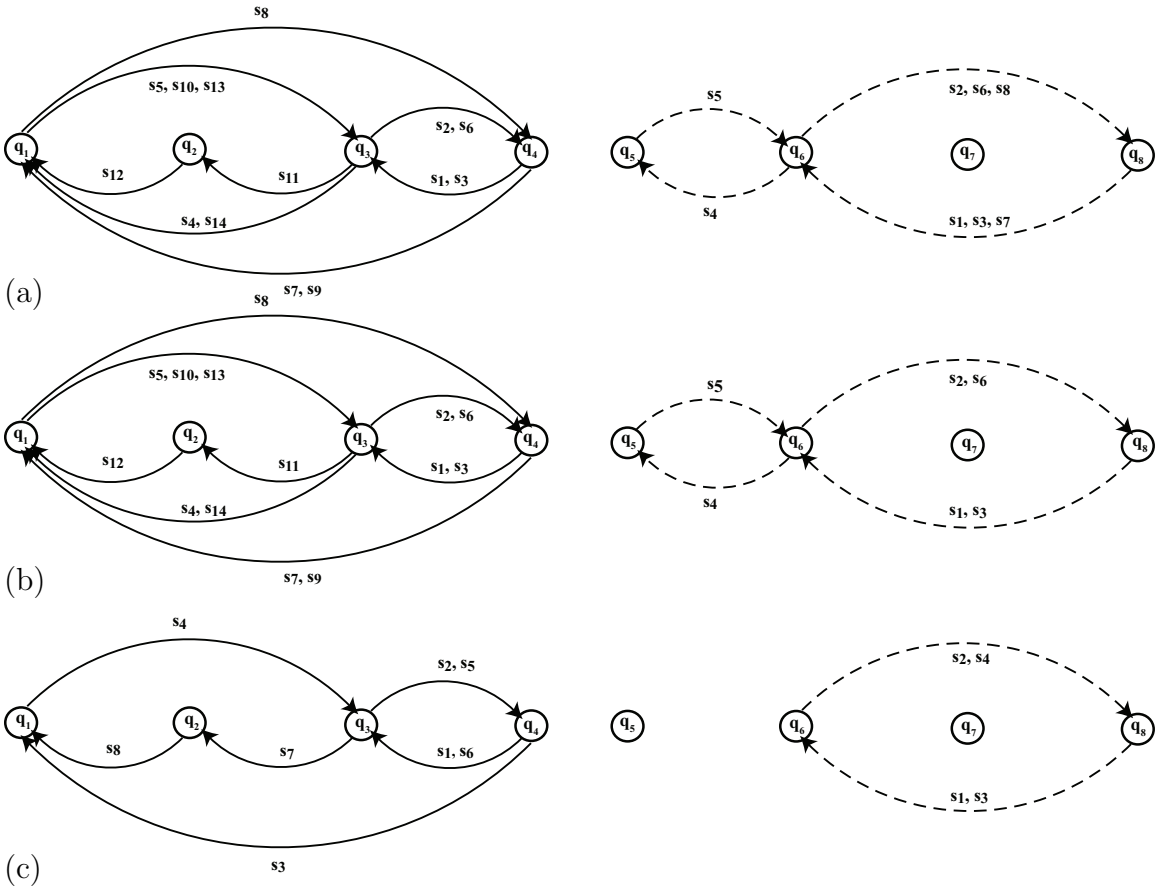

Figure 5.7. Switching graphs corresponding to the switching status obtained by (a) The first, (b) the second, and (c) the third algorithms. The solid and dashed arrows are designated for the switching status of the first and second joints, respectively.

Figure 5.8a shows snapshots of the 3D double pendulum during its motion and Fig. 5.8b shows that the pendulum's total energy remains constant throughout the simulation. Figure 5.9a and b show the trajectory of the Euler parameters for the first and second joints for three seconds simulated time. The normality condition is checked during the simulation for both joints and plotted as the solid black line

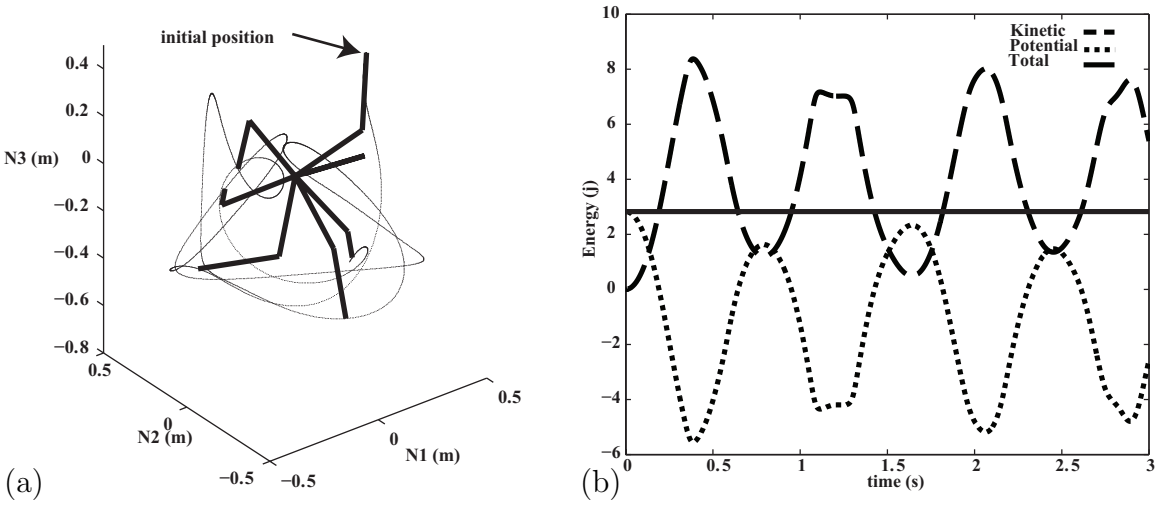

Figure 5.8. 3D pendulum simulation. (a) Snapshots of the 3D double pendulum with the path of the tip, (b) system energy.

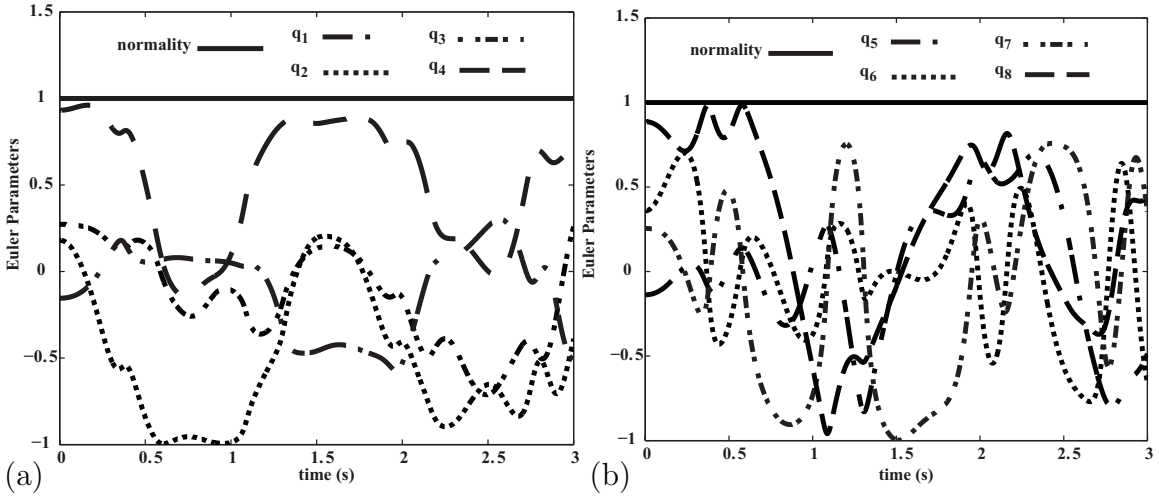

Figure 5.9. Euler parameters of (a) the first joint, (b) the second joint.

across both figures which indicates that the normality condition was satisfied during the simulation. This indicates that the solution for the Euler parameters does not drift, thus there is no need for renormalization.

5.5.2 Rotation with Contact and Impact

The proposed method is examined in a case that the double pendulum may contact the ground during the rotation. Therefore, the multibody system is imposed to an on the fly constraint because of contact and impact. In this case, the reduction of the equations of motion is done in two different steps during the numerical integration as shown in Fig. 5.1. For the non-holonomic constraints, the selection of the dependent generalized coordinates is taken place by using *qr decomposition* [167] and for the holonomic constraint the best algorithm of selection, the third algorithm in section 5.5.1, is used. Figure 5.10 shows few snapshots of the behavior of 3D double pendulum during the simulation with considering contact and impact. In this particular case, the coefficient of restitution (COR) is chosen to be 0.8 and the pendulum rebounding after impact until the kinetic energy approaches to zero.

The trajectory of Euler parameters in the first and second joints are shown in Fig. 5.11a and b, respectively, while the normality condition is satisfied for the both joints. It shows that the proposed numerical constraint embedding and the algorithm of selection work well even in presence of contact and impact.

To show the consistency of energy during contact simulation, the total energy, kinetic, and potential energy are illustrated in Fig. 5.12. It is obvious that the energy is reduced after each impact according to the specified COR.

The switching status of Euler parameters due to the holonomic constraints is shown in Fig. 5.13.

5.6 Conclusions

This chapter presented a new computational strategy to address different constraints involved in the dynamics of the new spatial rigid multibody model of motor

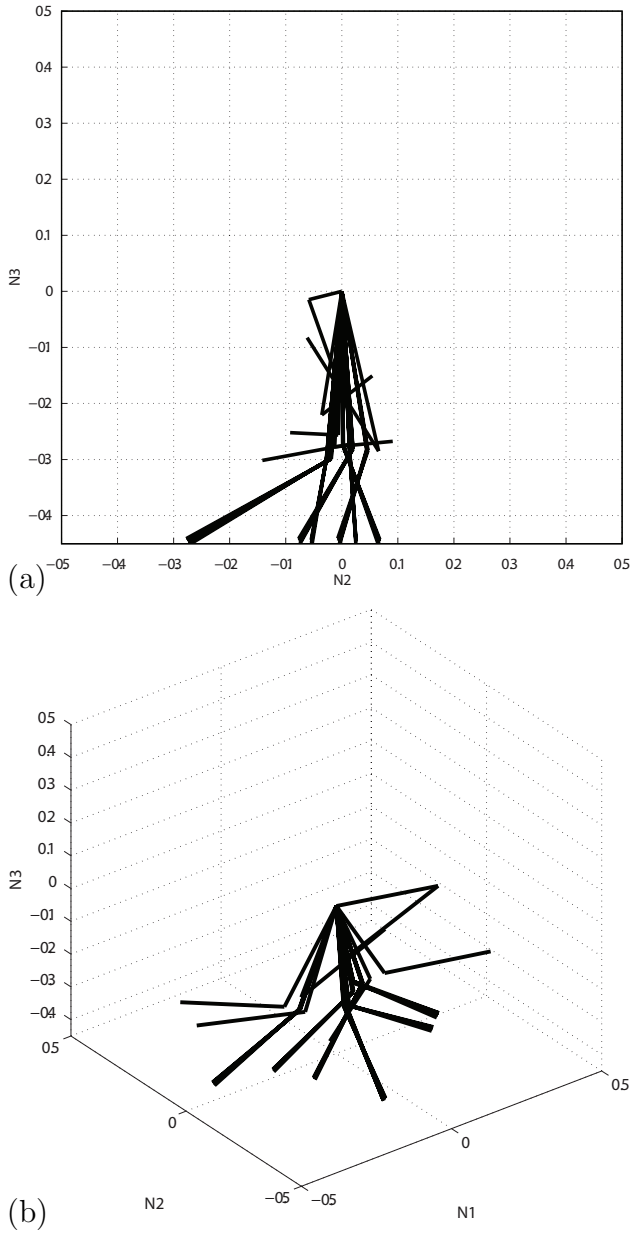

Figure 5.10. Snapshots of the 3D double pendulum's motion with contact shown in (a) 2D view, and (b) 3D view.

proteins. The constraints are holonomic, due to Euler parameters which are used to describe spatial rotation of bodies, and non-holonomic, because of contact-impact non-penetration conditions. The strategy is based on the reduction of the equations of motion into the minimal form using the numerical embedding of the holonomic and non-holonomic constraints during simulation. However, the proposed method

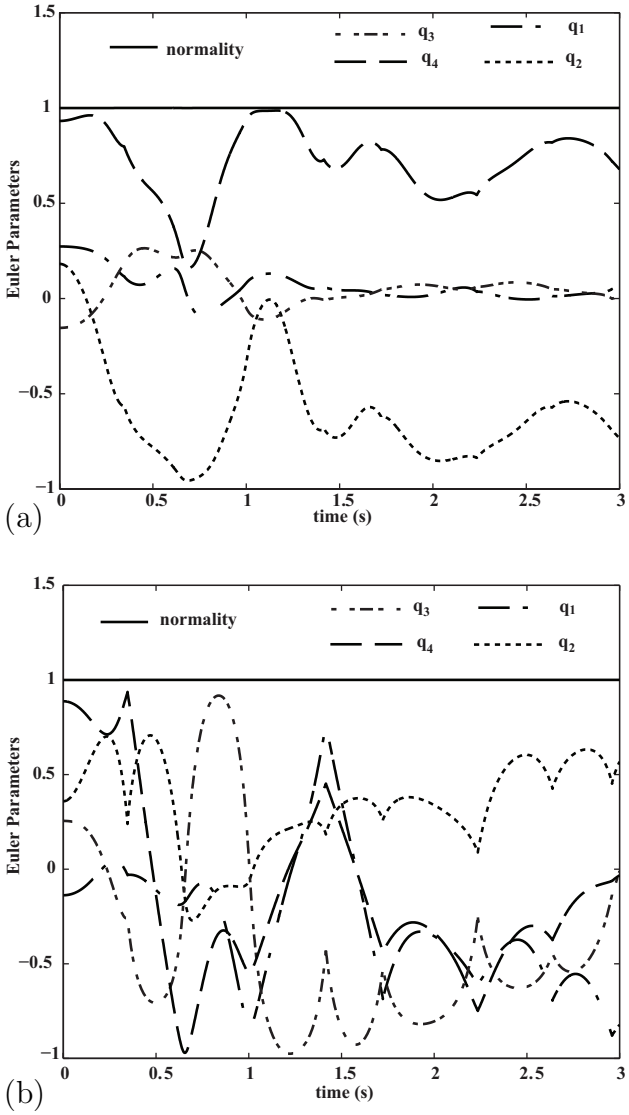

Figure 5.11. Trajectory of Euler parameters of (a) the first joint, (b) the second joint.

requires a procedure for selection of dependent parameters between Euler parameters which can create a singularity in the formulation. This singularity is avoided by switching the dependent parameter. Doing this as few times as possible maintains the dynamic consistency of the simulation while satisfying the normality constraint on the Euler parameters. In addition, calculation of post-impact velocities and contact forces [1, 2] along with the complications of quaternion algebra [154–156] are elimi-

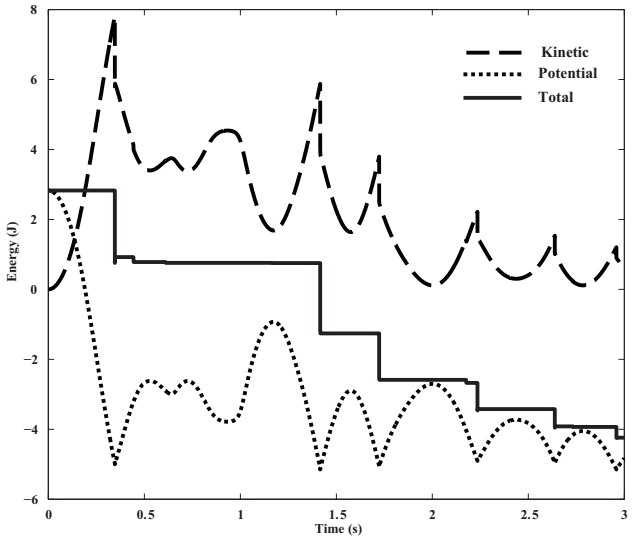

Figure 5.12. The total, kinetic, and potential energy of the double pendulum with contact.

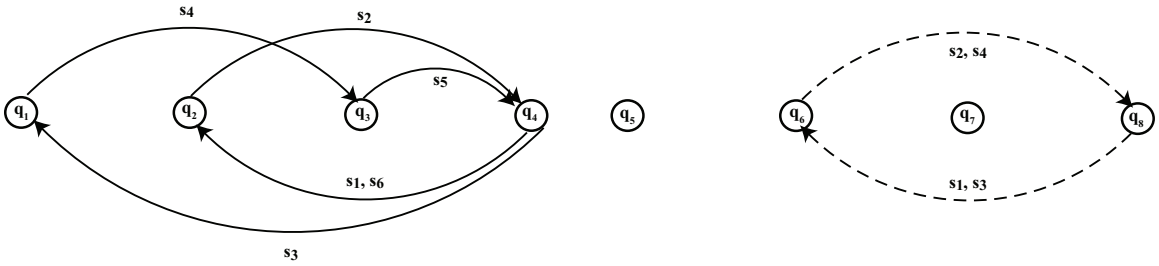

Figure 5.13. Switching graphs corresponding to the switching status obtained by the best algorithm of selection in presence of contact and impact.

nated. The effectiveness of the proposed simulation technique was tested on a 3D double pendulum for two different cases, 1) free rotation (only holonomic constraint), and 2) rotation with contact-impact (holonomic and non-holonomic constraints). The obtained results show ability of the numerical technique for handling Euler parameter constraint as well as contact-impact. the same procedure was invoked for numerical simulation of motor proteins which results were presented in chapters 2, 3 and 4.

Appendix A

Optical Tweezers: Experiment Setup and Theoretical Modeling

In this appendix, we present the setup used for the experiment of dynamic behavior of micro-nano sized bead in optical trapping process. In addition, the forces acting on the model of micro bead are presented in details.

A.1 Experimental Setup

Green-fluorescent polystyrene microspheres (Polysciences Inc) were suspended in distilled water and a small drop of this solution was placed on a coverslip. The OTs and imaging platform is shown in Fig. A.1. A Ti: Sapphire laser (MaiTai HP, Newport Spectra-Physics Inc.) beam operating in cw mode at $800nm$ was expanded using a beam expander (BE) and guided toward the sample via folding mirrors and into the rear port of an inverted optical microscope (Nikon Ti-U Eclipse). The laser beam was coupled to a 100X microscope objective (MO) (NA: 1.3, or 1.4 in some cases) through the back laser port as shown. For temporal modulation of the tweezers beam (i.e. force), the initiation and exposure duration was controlled by an external shutter (S, Uniblitz).

Samples were illuminated using a high pressure mercury lamp (Nikon) through blue/green excitation-emission filter cube in order to achieve high contrast for particle tracking. A dichroic mirror (DM1) was mounted to reflect the laser beam to the objective and to allow transmission of fluorescence excitation light (blue: BL). The fluorescent microsphere was trapped in the diffraction limited spot, and the trapping plane was matched with imaging plane by varying the divergence of the laser beam. The power of the optical trapping beam at the sample plane was estimated by multiplying the transmission factor of the objective with the laser beam power measured at the back aperture of the objective using a power meter (PM100D, Thorlabs Inc.). Fine laser power control was managed by orienting the polarizer (P). Images were collected with a reverse-cooled high speed digital camera (Hamamatsu C1140). The

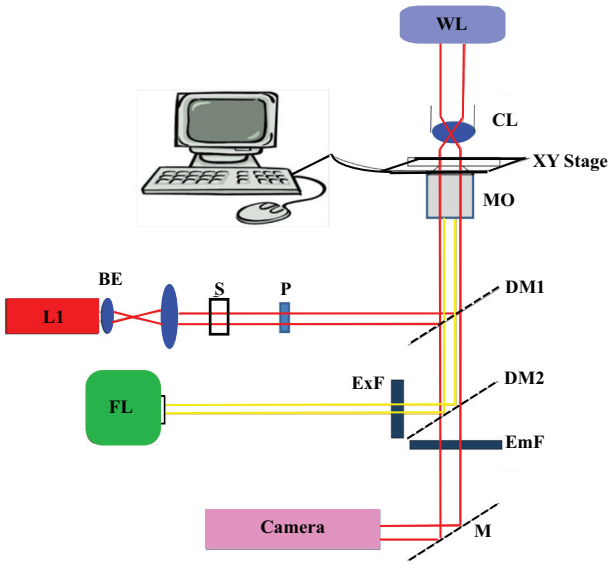

Figure A.1. Experimental setup: L1: Ti: sapphire Laser; BE: Beam Expander; S: Shutter; P: Polarizer; WL: White light; BS: Beam Splitter; FL: Fluorescence Excitation Mercury Lamp; ExF: Excitation Filter; EmF: Emission Filter; MO: Microscope Objective; CL: Condenser Lens; DM 1& 2: Dichroic Mirror; M: Mirror [10] .

images were processed using ImageJ software. An IR cut-off filter (Em. F) was used to prevent the back-scattered laser light from reaching the camera.

A.2 Forces

A.2.1 Brownian Motion

Random forces and moments in the model, representing Brownian motion, are implemented as Gaussian white noise. They act at and about the mass center of the bead, as shown in Fig. A.2. The random forces and moments shown in Fig. A.2 representing Brownian motion, are defined, for example, as

$$\begin{aligned} \mathbf{F}_{Brownian} &= C_{o1}(t)\ \widehat{\mathbf{N}}_1 + C_{o2}(t)\ \widehat{\mathbf{N}}_2 \\ \mathbf{T}_{Brownian} &= \bar{L}_S\ C_{o3}(t) \end{aligned} \tag{A.1}$$

where $\bar{L}_C$ is a characteristic length of body 'S'. The $C_{oi}(t)$ represent forces produced by randomly fluctuating thermal noise. Each component of the random force and

moment is treated independently as a normally distributed random variable [195]. They have the following *expectations*, $E[\cdot]$, or weighted average values,

$$E\,[\,C_{oi}(t)\,]\;=\;\langle\,C_{oi}(t)\,\rangle\;=\;0\;=\;\mu \tag{A.2}$$

and are governed by a fluctuation-dissipation relation expressed as

$$E\,[\,C_{oi}(t_1)\;C_{oj}(t_2)\,]=2\;\beta\;k_B\;\mathrm{T}\;\delta(t_1-t_2)\delta_{i,j} \tag{A.3}$$

where k_B and T are the Boltzmann constant and absolute temperature [195, 198]. The relation in (A.3) implies that there is no time dependency between the random process over time; the random sequence of forces does not repeat regularly.

In addition, (A.2) and (A.3) imply

$$E[C_{oi}^2(t)]\;=\;2\;\beta\;k_B\;\mathrm{T}\;=\;\mathrm{Var}(C_{oi}(t))\;=\;\sigma^2 \tag{A.4}$$

which is the variance of C_{oi}. Thus the C_{oi} can be generated using the Matlab function `normrnd`$(\mu,\sigma,\ldots)$ which generates random variables with a normal distribution.

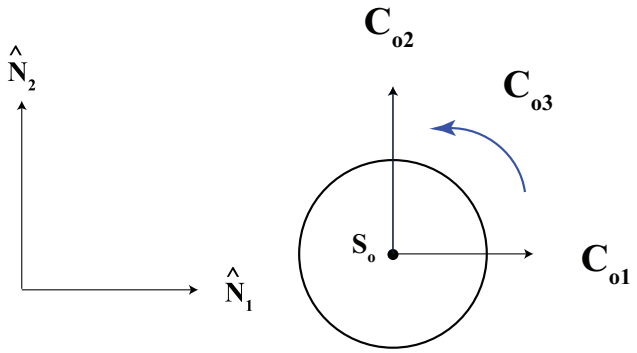

Figure A.2. Brownian motion for microbead .

The collection of random forces comprise $\mathbf{\Gamma}_{Brown}$. These randomly fluctuating discontinuous functions slow numerical integration so each random variable is held

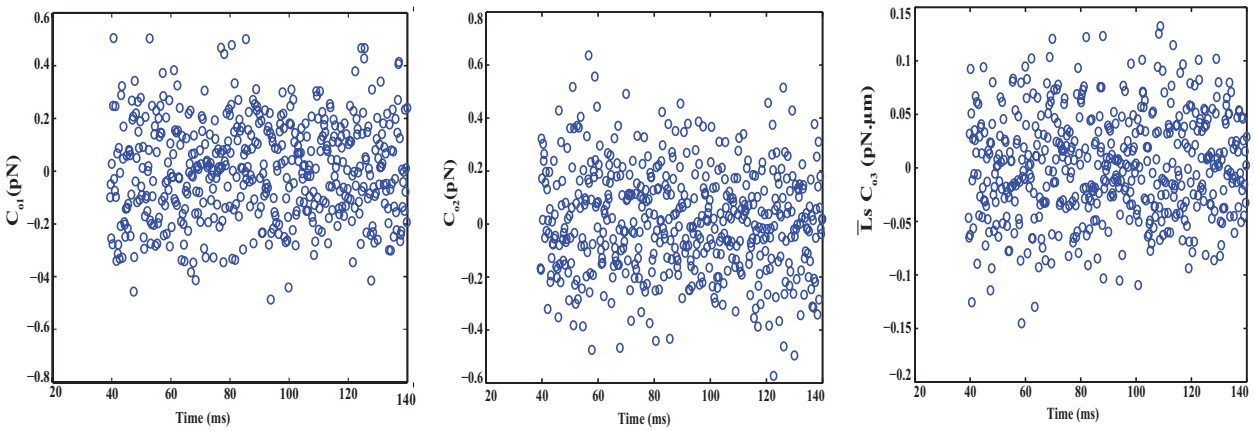

Figure A.3. Random forces acting on body 'S' in Fig. 2.1 for the $500nm$ Bead .

constant during a single integration step; the random variable is updated at the beginning of each step. Thus the value of each random variable is known before the integration step, and the decomposed value of the random force must equal it. This is accomplished by defining

$$\mathbf{\Gamma}_{Brown} = \mathrm{R}_{nd}\ \mathbf{r}_{nd} = \mathrm{R}_{nd} \begin{bmatrix} C_{o1} \\ C_{o2} \\ C_{o3} \\ \vdots \end{bmatrix} \tag{A.5}$$

where R_{nd} transforms the random forces into generalized active forces. An example of the random forces used is given in Fig. A.3.

A.2.2 Optical Force

A.2.2.1 Beam Model

There are three primary methods for modeling optical forces. In the Rayleigh regime, the particle is approximated as a point dipole within an electromagnetic field. This approach is useful when the particle radius is much less than the wavelength of

the laser. In the Mie regime, where the bead's size is comparable to the wavelength, Mie scattering theory is used. Recent developments in computational techniques based on Mie scattering theory provide a capability to extend this method to larger particles up to $100\mu m$ diameter [226]. In the ray-optics regime, the laser beam is discretized into a number of rays and geometrical optics is used to calculate the forces exerted on the particle by each ray. This approach is useful for particles of radius larger than the wavelength of laser light used. Herein a ray-optics approach is used for the sake of simplicity.

In the ray-optics approach to modeling optical tweezers, the total light beam is decomposed into individual rays, as shown in Fig. A.4, that each propagate in straight lines in a medium of uniform refractive index [134]. Each ray is assigned an appropriate intensity (I_{ray}), direction (ϕ_{ray}), and polarization state, and has the characteristics of a plane wave of zero wavelength which can change directions when it reflects, refracts, or changes polarization at dielectric interfaces according to the Fresnel formulas presented in section A.2.2.2. Diffractive effects are neglected in this regime [227].

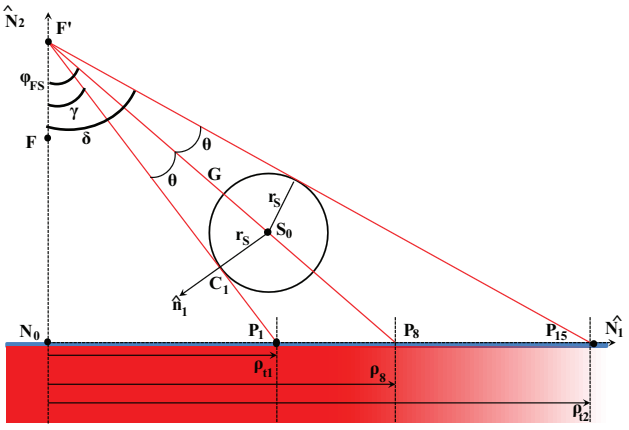

Figure A.4. Schematic showing ray-bead contact and ray radial origins .

First, the origins of each of the sample rays need to be calculated. To do this, the angle, ϕ_{FS_0}, between the central ray and $\widehat{N}_2$, as shown in Fig. A.4, needs to be found

$$\phi_{FS_0} \;=\; \arctan\frac{q_1}{\acute{f}-q_2} \tag{A.6}$$

where $\acute{f}$ is the distance between the virtual point $\acute{F}$ and the inertial frame point, N_o. The origins of the tangential rays, ρ_{t_1} and ρ_{t_2}, can then be calculated. First, calculate the angle, θ, between FS_o and the lines connecting $\acute{F}$ to ρ_{t_1} and ρ_{t_2} as shown in Fig. A.4.

$$\sin\theta = \frac{r_S}{\sqrt{q_1^2+(\acute{f}-q_2)^2}} \tag{A.7}$$

$$\cos\theta = \sqrt{1-\sin^2\theta} \tag{A.8}$$

$$\theta = \arctan\frac{\sin\theta}{\cos\theta} \tag{A.9}$$

$$\rho_{t1} = \acute{f}\ \tan(\gamma) \qquad \rho_{t2} = \acute{f}\ \tan(\delta) \tag{A.10}$$

where $\gamma = \phi_{FS_0} - \theta$ and $\delta = \phi_{FS_0} + \theta$. Next, since fifteen rays are being sampled (of the total number of rays impacting the bead at any given moment), define the distance, *span*, between ρ_{t1} and ρ_{t2}, and an interval, $\Delta\rho$, between each ray origin, ρ_k:

$$\rho_k = \rho_{t1} + (k-1)\Delta\rho \qquad k = 1, \cdots, 15 \tag{A.11}$$

where

$$\Delta\rho = \frac{span}{14} \qquad span = |\rho_{t2} - \rho_{t1}| \tag{A.12}$$

Note that *span*, as defined above, will begin to approach infinity as S_0 approaches a certain distance, r_S, from $\acute{F}$. To counteract this, arbitrarily set

$$span = 2R_{obj} \tag{A.13}$$

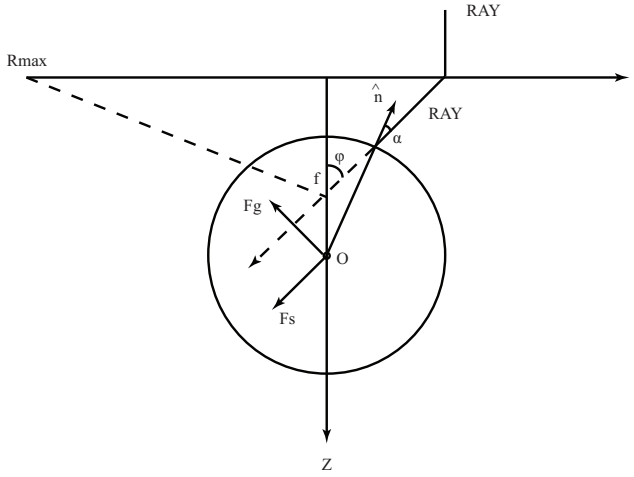

Figure A.5. Geometry of an incident ray giving rise to gradient and scattering force contributions, F_{grad} and F_{scat}. Here, θ denotes the angle of incidence, f denotes the focal line, and O denotes the sphere's center of mass .

Each ray origin will be treated as the x-coordinate (with respect to the inertial reference frame) of the point $P_k(\rho_k, 0)$, which is defined as the point of exit of the ray from the objective lens.

The simple ray-optics model of the optical tweezers used here for calculating the optical forces on a sphere of diameter $\gg \lambda$ is illustrated in Fig. A.5, adapted from [134]. The trap consists of an incident parallel beam of arbitrary mode structure and polarization that enters a high numerical-aperture (NA) microscope objective and is focused, ray-by-ray, to a focal line. Computation of the total force imparted to the sphere consists of summing the contributions of each ray entering the aperture at radius ρ_{ray} with respect to the beam axis. The effect of neglecting the finite size of the actual beam focus, which can approach the limit of $\lambda/2n_m$ [228], is negligible for spheres much larger than λ. The point-focus description of the convergent beam, in which the ray directions and momenta continue in straight lines through the focus, gives the correct incident polarization and momentum for each ray. The rays then reflect and refract at the surface of the sphere, giving rise to the optical forces.

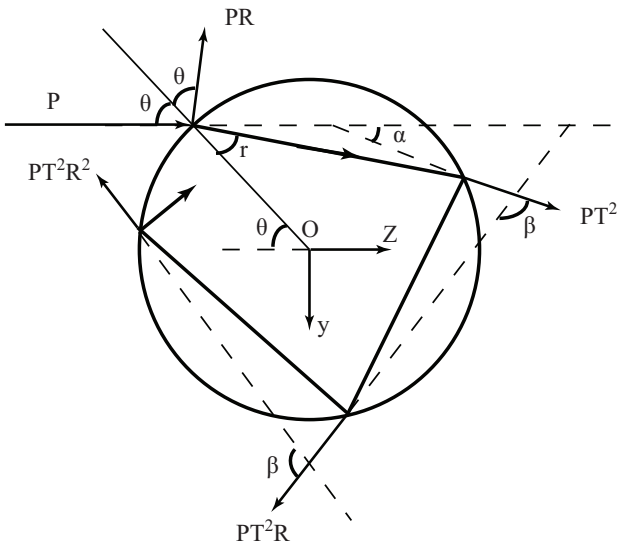

Figure A.6. Geometry for calculating the force imparted by a single incident ray. The incident ray has power P and impacts the particle surface at an angle of incidence, θ. Some of the ray is reflected off (of power PR), while the rest of the ray is infinitely refracted at an angle denoted by r (with portions of the transmitted light passing out of the particle at powers PT^2R^n) .

To illustrate the generation of optical forces, consider the force due to a single ray of power P hitting a dielectric sphere at an angle of incidence, α, with incident momentum per second $n_m P/c$, as illustrated in Figs. A.5 and A.6. The total force imparted onto the sphere by the ray is the sum of the contributions due to the reflected ray of power PR and the infinite number of emergent refracted rays of successively decreasing power PT^2, PT^2R, $\cdots$, PT^2R^n, where the quantities R and T are the Fresnel coefficients of reflection and transmission, respectively, of the sphere surface at α. The net force acting through the sphere's mass-center, S_0, can be resolved into F_{scat} and F_{grad} components as given by Roosen et al. [229] and [230], for a summary of derivation refer to section A.2.2.4

$$F_{scat} = \frac{n_m P}{c} \left[\, 1 + R \cos 2\alpha - a \, \right] \tag{A.14}$$

where

$$a = \frac{T^2\left[\cos(2\alpha - 2\beta) - R\cos(2\alpha - \pi)\right]}{1 + R^2 - 2R\cos(\pi - 2\beta)} \tag{A.15}$$

and

$$F_{grad} = \frac{n_m P}{c}\left[\ R\sin 2\alpha - \ b\ \right] \tag{A.16}$$

where

$$b = \frac{T^2\left[\sin(2\alpha - 2\beta) - R\sin(2\alpha - \pi)\right]}{1 + R^2 - 2R\cos(\pi - 2\beta)} \tag{A.17}$$

where α and β are the angle of incidence and refraction, respectively. These formulas sum over all scattered rays, and are therefore exact. The forces are polarization-dependent, since R and T are different for rays polarized perpendicular or parallel to the plane of incidence.

In (A.14), the F_{scat} component, pointing in the direction of the incident ray, is denoted as the scattering force component for this single ray as shown in Fig. A.5, and acts in a direction parallel to the incident ray. Similarly, in (A.16), the F_{grad} component, pointing in a direction perpendicular to the ray in the direction of the ray axis, is denoted as the gradient force component for the ray as illustrated in Fig.A.5. The action of each ray's gradient force is to pull to particle's mass-center onto the ray-axis. The net scattering and gradient forces of the whole beam are defined as the vector sums of the scattering and gradient force contributions of each individual ray within the beam. The result is that the particle will be puled toward the rays of higher power.

A.2.2.2 Fresnel Coefficients

Before the Fresnel coefficients can be calculated, first calculate the angle of incidence, α_k, and the angle of refraction, β_k, of each ray with the sphere.

The angles of incidence are calculated using the definitions of the Dot Product and the Cross Product

$$\cos\alpha_k = \frac{\mathbf{P}_{C_kP_k} \cdot \widehat{\mathbf{n}}_k}{||\mathbf{r}_{C_kP_k}||||\widehat{\mathbf{n}}_k||} \tag{A.18}$$

$$\sin\alpha_k = \frac{\mathbf{P}_{C_kP_k} \times \widehat{\mathbf{n}}_k}{||\mathbf{P}_{C_kP_k}||||\widehat{\mathbf{n}}_k||} \tag{A.19}$$

$$\alpha_k = \arctan\frac{\sin\alpha_k}{\cos\alpha_k} \tag{A.20}$$

The angles of refraction are calculated according to Snell's Law and the Pythagorean Theorem

$$\sin\beta_k = \frac{n_m \sin\alpha_k}{n_S} \tag{A.21}$$

$$\cos\beta_k = |\sqrt{1-\sin^2\beta_k}| \tag{A.22}$$

$$\beta_k = \arctan\frac{\sin\beta_k}{\cos\beta_k} \tag{A.23}$$

From here, calculate the Fresnel Reflection and Transmission Coefficients

$$R_k = \frac{1}{2}\left[\left[\frac{n_m\cos\alpha_k - n_S\cos\beta_k}{n_m\cos\alpha_k + n_S\cos\beta_k}\right]^2 + \left[\frac{n_m\cos\beta_k - n_S\cos\alpha_k}{n_m\cos\beta_k + n_S\cos\alpha_k}\right]^2\right] \tag{A.24}$$

$$T_k = 1 - R_k \tag{A.25}$$

A.2.2.3 Force Frames

The force exerted by a single ray can be resolved into two components: the scattering force, F_{scat}, which acts in the direction of the ray, and the gradient force, F_{grad}, which acts perpendicular to the direction of the ray, in the direction of increasing

intensity. In order to accurately model these forces, first set up so-called ray-attached frames-axes that correspond to the components of the ray.

First, calculate the angle each ray is taking (with respect to the line between N_0 and F) using the general formula:

$$\phi_k = \arctan \frac{\rho_k}{\acute{f}} \tag{A.26}$$

From these angles, formulate the general rotation matrices for each force frame:

$$\overset{\mathbf{F}_k}{\mathbf{N}}\mathbf{R} = \begin{bmatrix} \cos\phi_k & -\sin\phi_k & 0 \\ \sin\phi_k & \cos\phi_k & 0 \\ 0 & 0 & 1 \end{bmatrix} \tag{A.27}$$

These rotation matrices will determine the relationship between the force components in the ray-attached frames and the force components in the inertial reference frame.

A.2.2.4 Force Components

Start with the equation for the total force exerted by a single ray [134, 229]

$$F_{tot,k} = \frac{n_m P_k}{c}\left[1 + R_k e^{2i\alpha_k} - T_k^2 d\,\right] \tag{A.28}$$

where

$$d \;=\; \frac{e^{2i(\alpha_k-\beta_k)}}{1 - R_k e^{i(\pi-2\beta_k)}} \tag{A.29}$$

In order to eliminate imaginary terms within the denominator, so that later computations are quicker, first rationalize the fraction in the T-term:

$$\begin{aligned} d &= \frac{e^{i(2\alpha_k-2\beta_k)}}{1 - R_k e^{i(\pi-2\beta_k)}} \cdot \frac{1 - R_k e^{-i(\pi-2\beta_k)}}{1 - R_k e^{-i(\pi-2\beta_k)}} \qquad \text{(A.30)} \\ &= \frac{e^{i(2\alpha_k-2\beta_k)}\left[1 - R_k e^{-i(\pi-2\beta)}\right]}{\left[1 - R_k e^{i(2\alpha_k-2\beta_k)}\right]\left[1 - R_k e^{-i(2\alpha_k-2\beta_k)}\right]} \\ &= \frac{e^{i(2\alpha_k-2\beta_k)} - R_k e^{[i(2\alpha_k-2\beta_k)-i(\pi-2\beta_k)]}}{1 + R_k^2 - R_k\left[e^{i(\pi-2\beta_k)} + e^{-i(\pi-2\beta_k)}\right]} \\ &= \frac{e^{i2\alpha_k-2\beta_k} - R_k e^{i(2\alpha_k-\pi)}}{1 + R_k^2 - 2R_k\cos\left(\pi - 2\beta_k\right)} \qquad \text{(A.31)} \end{aligned}$$

Following [134, 229], the gradient force, $F_{grad,k}$, is taken to be the imaginary component of the total force, while the scattering force, $F_{scat,k}$, is taken to be the real component. Using Euler's Formula, $F_{tot,k}$ can be resolved into (A.14) and (A.16).

Force vectors can be generated using the ray-attached frames generated earlier

$$\mathbf{F}_{tot,k} = F_{grad,k}\widehat{\mathbf{N}}_1 + F_{scat,k}\widehat{\mathbf{N}}_2 \tag{A.32}$$

Each force will be applied to a corresponding contact point on the particle, C_k.

A.2.3 Other External Forces

The other forces accounted for are depicted in Fig. 2.1b. Weight, buoyancy, and drag force are set as:

$$\mathbf{F}_g = -m_S g_0 \, \widehat{\mathbf{N}}_2 \tag{A.33}$$

$$\mathbf{F}_B = \rho_m g_0 V_p \, \widehat{\mathbf{N}}_2 \tag{A.34}$$

$$\mathbf{F}_D = -\beta_v{}^N\mathbf{V}_{S_0} \tag{A.35}$$

where

$$\beta_v = 6\pi\mu_m r_S$$

is obtained from Stokes' Law.

A.3 Moments

There are three sources of torque in this system: the torque imparted by the beam, the viscous drag, and Brownian forces.

The moments imparted onto the particle by each of the rays is set as

$$\mathbf{M}_k = \mathbf{P}_{S_0C_k} \times \mathbf{F}_{tot,k} \tag{A.36}$$

The viscous torque is obtained from

$$T_{drag} = -\beta_\omega \dot{q}_3 \tag{A.37}$$

where

$$\beta_\omega = 8\pi\mu_m r_S^3$$

Finally, Brownian moment is,

$$T_{Brownian} = \bar{L}_S \; C_{o3}(t) \tag{A.38}$$

where $\bar{L}_S$ is a characteristic length of body 'S'.

A.4 Physical Parameters

The physical parameters used for numerical simulation of microbead under influence of Optical tweezers are presented in Table A.1.

A.5 Vertical and Rotational Coordinate

The simulation of the $500nm$ bead yields data for all three coordinates, q_1, q_2, and q_3, which can be examined. Here the data for the vertical, q_2, and rotational, q_3, coordinates are presented for the sake of completeness.

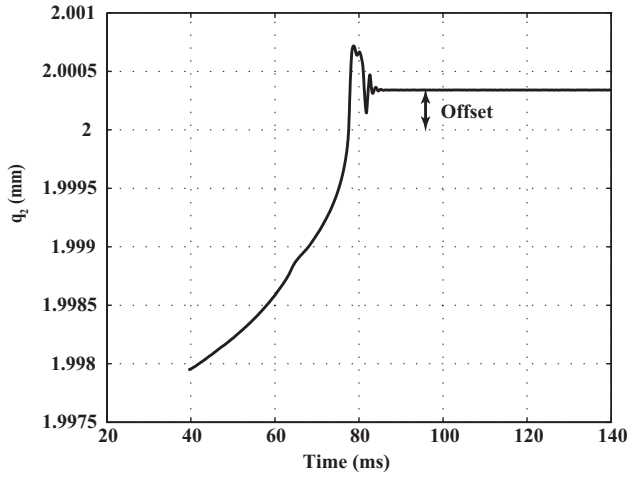

Figure A.7. Simulation data for q_2 the multiscale model $500nm$ (CPUtime=21_{mins}, `AbsTol`=10^{-8}, `RelTol`=10^{-7}, $\Delta t = 0.001_{ms}$). .

Table A.1. Definition of Quantities Used

Quantity	Definition	Units	Value Used
f	focal length	mm	2
P_0	laser beam power	$\frac{pg \cdot mm^2}{ms^3}$	156×10^9
P_{1-15}	ray powers	$\frac{pg \cdot mm^2}{ms^3}$	variable
I_0	laser beam intensity	$\frac{pg}{ms^3}$	$\approx 5.09 \times 10^{10}$
I_{1-15}	ray intensities	$\frac{pg}{ms^3}$	variable
Re	Reynolds number	$unitless$	variable
ρ_m	density of fluid medium	$\frac{pg}{mm^3}$	0.9982071×10^9
μ_m	dynamic viscosity of fluid medium	$\frac{pg}{(ms \cdot mm)}$	1002×10^3
ϕ_{FS}	the angle of the line between point F and S_0	$radians$	variable
ρ_0	the radial origin of the central ray	mm	variable
ρ_{1-15}	radial origins of ray_{1-15}	mm	variable
ϕ_{1-15}	angle of refraction of rays exiting objective	$radians$	variable
θ	angle between $\mathbf{P}_{FS_0}$ and tangential rays	$radians$	variable
r_S	microparticle radius	mm	0.0008
n_S	microparticle refraction index	$unitless$	1.496
R_{obj}	radius of objective lens	mm	2.6
NA	numerical aperture of objective	$unitless$	1.30
n_g	glass refraction index	$unitless$	1.5
n_m	refraction index of medium	$unitless$	1.330
c	speed of light in a vacuum	$\frac{mm}{ms}$	299792458
σ	beam waist length at the objective lens	mm	2.5
ω	beam waist length at the focal point	mm	3.5×10^{-3}
g_0	standard acceleration due to gravity	$\frac{mm}{ms^2}$	9.80665×10^{-3}
α_{1-15}	incident angle of ray_{1-15} with microparticle	$radians$	variable
β_{1-15}	refraction angle of ray_{1-15}	$radians$	variable
λ	wavelength of laser	mm	0.0008

$1\ N = 1\frac{kg \cdot m}{s^2} = 10^{12}\ \frac{pg \cdot mm}{ms^2}$, $1\ J = 1\ \frac{kg \cdot m^2}{s^2} = 10^{15}\ \frac{pg \cdot mm^2}{ms^2}$, $1\ W = 1\ \frac{kg \cdot m^2}{s^3} = 10^{12}\ \frac{pg \cdot mm^2}{ms^3}$

The data for the vertical directions, Fig. A.7, shows gradual movement toward the focal point in the vertical direction. However, the key thing to notice is the oscillations in the vertical direction when the bead reaches the focal line. In addition, there is a offset between the vertical position that the bead settled and the focal point

due to optical force cancellation which happens upper than the focal point [134]. Currently, work is underway to improve experimental bead tracking in the vertical direction in order to obtain a truer comparison for the simulation.

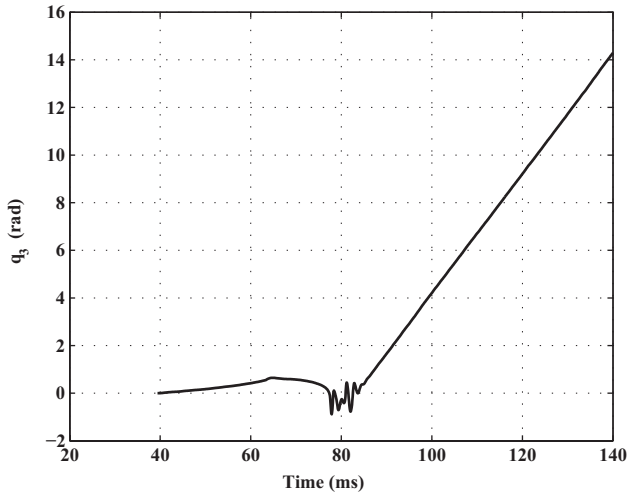

Figure A.8. Simulation data for q_3 the multiscale model $500nm$ (CPUtime=21_{mins}, `AbsTol`=10^{-8}, `RelTol`=10^{-7}, $\Delta t = 0.001_{ms}$). .

The rotational coordinate, plotted in Fig. A.8, shows that there is little rotation as the $500nm$ bead approaches the focal line. However, the oscillations at the focal line impart some rotational velocity to the bead. After reaching the focal line, the bead slowly spins thereby slowly increasing the q_3 coordinate. There is no experimental tracking of the bead's rotation for comparison at this time.

Appendix B

Motor Proteins: Model Parameters and Units

This appendix discusses in detail the elements of the proposed model and the physical parameters of the mechanical model of myosin V in chapter 3.

B.1 Physical Parameters

The physical parameters used in the numerical simulation of motor proteins, especially myosin V, are presented here.

B.2 Units

This appendix gives a brief summary of the units used in the simulation. The unit basis consists of the attogram (ag), the nanometer (nm), the millisecond (ms), and the radian (rad). With this choice the force unit becomes

$$1N = 1\frac{kg \cdot m}{s^2}\ \frac{10^{21}ag}{kg}\ \frac{10^{9}nm}{m}\ \frac{(s)^2}{(10^3ms)^2} = 10^{24}\frac{ag \cdot nm}{ms^2} \tag{B.1}$$

and the unit of work becomes

$$1\ J\ =\ 1\ \frac{kg \cdot m^2}{s^2}\ =\ 10^{33}\ \frac{ag \cdot nm^2}{ms^2}\ . \tag{B.2}$$

These values are chosen so that the masses have a value near unity and to improve the stability of the numerical integration.

Table B.1. Physical Parameters of the Myosin V Mechanical Model

Quantity	Definition	Value	Value Used	Ref.
d_1	see Fig. 3.2	0_{nm}	same	[231, 232]
d_{2-6}	see Fig. 3.2	36_{nm}	same	[231, 232]
e	the elementary or quantum charge	$1.602 \times 10^{-19}_{C}$	same	[233]
$C_{\mathrm{B}_{1-6}}$	charge on actin binding sites '$\mathrm{B_i}$', see Fig. 3.2	$-1e$	same	[41]
$C_{\mathrm{C_E}}, C_{\mathrm{D_E}}$	charge on the head binding sites, see (3.10)	$5e$	same	[41]
L_1	see Fig. 3.2	10_{nm}	same	[192]
L_2, L_3	see Fig. 3.2	15_{nm}	same	[95]
L_4, L_5	see Fig. 3.2	3_{nm}	same	[95]
L_6, L_8	see Fig. 3.2 and (3.7)	2.12_{nm}	same	
L_7, L_9	see Fig. 3.2 and (3.8)	-1.77_{nm}	same	
m_A, m_B	mass of necks, bodies 'A' and 'B', see Fig. 3.2	15_{kDa}	$15/N_A \times 10^{21}_{ag}$	[95]
m_C, m_D	mass of heads, bodies 'C' and 'D', see Fig. 3.2	80_{kDa}	$80/N_A \times 10^{21}_{ag}$	[95]
m_{LOAD}	mass of load, see Fig. 3.2	100_{kDa}	$100/N_A \times 10^{21}_{ag}$	
β	viscous damping coefficient, see (4.1)	$10^{-7}\frac{pN \cdot s}{nm}$	$10^{8}_{ag/ms}$	[195]
a_1	see (4.8)	-	0.9999999	
a_2	see (4.8)	-	1×10^{-7}	
$\bar{L}_A, \bar{L}_B$	neck characteristic length, bodies 'A' and 'B', see (3.5)	15_{nm}	same	
$\bar{L}_C, \bar{L}_D$	head characteristic length, bodies 'C' and 'D', see (3.5)	3_{nm}	same	
r_{head_1}	radial length of head, see (3.14)	3_{nm}	same	[95]
r_{head_2}	radial width of head, see (3.14)	2.5_{nm}	same	[95]
r_{head_3}	radial width of head, see (3.14)	2.5_{nm}	same	[95]
$(4\pi\epsilon_0)^{-1}$	ϵ_0=permittivity of free space, see (3.10)	$9 \times 10^{9}\frac{N \cdot m^2}{C^2}$	$9 \times 10^{51}\frac{ag \cdot nm^3}{ms^2 \cdot C^2}$	[233]
ϵ_r	relative permittivity, see (3.10)	80	same	[41]
k	inverse of the Debye length, see (3.10)	$\frac{1}{3.5nm}$	same	[41]
a	excluded volume radius, see (3.10)	1_{nm}	same	[41, 234]
k_o	charge offset, see (3.10)	-	1_{nm}	
k_B	Boltzmann constant, see (A.5)	$1.38 \times 10^{-23}\frac{J}{K}$	$1.38 \times 10^{10}\frac{ag \cdot nm^2}{ms^2 \cdot K}$	[233]
T	Room temperature, see (A.5)	300_K	same	
v_{avg}	average velocity of myosin V	$1000_{nm/s}$	$1\frac{nm}{ms}$	[235]
N_A	Avogadro's number	$6.0221215 \times 10^{23}\frac{1}{mole}$	same	[192]

C (Coloumb), kDa (kiloDalton), nm (nanometer), pN (picoNewton), ag (attogram), ms (millisecond), K (Kelvin), J (Joules)

Appendix C

Constraint Embedding

This appendix discusses a new numerical technique for handling on-fly constraints of a multibody system due to extra generalized coordinates and contact. The reduction to a minimal set is accomplished using a constraint matrix. This reduction is performed numerically during the simulation, rather than symbolically reducing the model. Holonomic and nonholonomic constraints can be included in the constraint matrix. The *holonomic* constraints represent the normality condition on the Euler parameters. The *non-holonomic* constraints are related to sticking or sliding contact or impact between the heads and the actin filament. This strategy reduces the computational cost of the impact/contact analysis which leads to a faster simulation. Finally, the general equations of motion are reduced into the minimal form for both the first and second order models.

C.1 Holonomic Constraints

Euler parameters are used to model the orientation of bodies in order to eliminate singularities in the description of orientation. Euler parameters can be referred to as a unit quaternion containing four dependent parameters which must satisfy a normality constraint. Considering $\{q_4, q_5, q_6, q_7\}$ in Fig. 3.2, the normality constraint has the form,

$$q_4^2 + q_5^2 + q_6^2 + q_7^2 = 1 \tag{C.1}$$

Equation (C.1) is differentiated to obtain a linear constraint in terms of the generalized speeds,

$$\dot{q}_4\ q_4 + \dot{q}_5\ q_5 + \dot{q}_6\ q_6 + \dot{q}_7\ q_7 = 0 \tag{C.2}$$

and likewise for all sets of Euler parameters. The collection of these constraints can be expressed as a matrix

$$\mathbf{0} \ = \ C_H\ \dot{\mathbf{q}} \tag{C.3}$$

C.2 Non-Holonomic Constraints

Nonholonomic constraints are used to represent sticking or sliding contact or impact between the heads and the actin filament. The normal velocity of contact points must equal zero when the heads contact to the actin filament in order to ensure that the head does not penetrate the filament. It is assumed that the heads do not rebound after an impact with the substrate. When the heads dock the tangential velocity of the contact points and the angular velocity of the heads must equal zero.

The velocity of contact points are related to the generalized speeds through the contact Jacobian matrix

$$\boldsymbol{\vartheta} \;=\; \begin{bmatrix} \boldsymbol{v}_c \\ \boldsymbol{\omega}_c \end{bmatrix} = J_c\ \dot{\mathbf{q}} \tag{C.4}$$

where $\boldsymbol{v}_c$ and $\boldsymbol{\omega}_c$ are the translational linear velocity of contact points and the angular velocity of heads respectively, J_c is the the contact Jacobian matrix. Equation (C.4) can be presented in matrix form similar to (C.3). When the velocity of contact points are equal to zero

$$\mathbf{0} \;=\; C_N\ \dot{\mathbf{q}} \tag{C.5}$$

C.3 Reduction

C.3.1 Reduced Second Order Model

There are different techniques for deriving the equations of motion for constrained multibody systems such as the method of Lagrange Multipliers, projecting the unconstrained equations, and symbolic constraint-embedding. Formulating the equations of motion using the constraint-embedding approach leads to a minimum number of *ordinary differential equations* which are passed to an ODE solver. Also, constraint embedding addresses issues related to drift and stabilization of DAE solvers during numerical integration of the equations of motion formulated by the other tech-

niques [167]. Here, constraint-embedding is used to reduce the equations of motion in (3.1).

$$\mathbf{0} \;=\; C\;\dot{\mathbf{q}} \;=\; \begin{bmatrix} C_H \\ C_N \end{bmatrix} \dot{\mathbf{q}} \tag{C.6}$$

qr decomposition is used to split the general constraint matrix of C.6 into portions corresponding to dependent and independent generalized speeds:

$$C\;E = Q\;R = Q\,[\;R_p \quad R_m\;] = [\;C_p \quad C_m\;] \tag{C.7}$$

where $m + p = n$, $E \in \mathbb{R}^{n\times n}$ is the permutation matrix, $Q \in \mathbb{R}^{p\times p}$ is an orthogonal matrix, and $R \in \mathbb{R}^{p\times n}$ is upper-triangular matrix that includes $R_p \in \mathbb{R}^{p\times p}$ and $R_m \in \mathbb{R}^{p\times m}$. C_p and C_m are constraint matrices corresponding to the dependent and independent generalized speeds, respectively. Equation (C.6) is rewritten using the identity matrix $EE^T = I$

$$\mathbf{0} \;=\; C(E\;E^T)\;\dot{\mathbf{q}} \;=\; C_p\;\dot{\mathbf{q}}_p \;+\; C_m\;\dot{\mathbf{q}}_m \tag{C.8}$$

Solving (C.8) for the dependent generalized speeds in terms of the independent generalized speeds yields

$$\dot{\mathbf{q}}_p \;=\; C_{pm}\;\dot{\mathbf{q}}_m \;=\; C_p^{-1}\;C_m\;\dot{\mathbf{q}}_m \tag{C.9}$$

The dependent generalized accelerations are obtained by differentiation of (C.9) with respect to time.

$$\ddot{\mathbf{q}}_p \;=\; \dot{C}_{pm}\;\dot{\mathbf{q}}_m \;+\; C_{pm}\;\ddot{\mathbf{q}}_m \tag{C.10}$$

The constraint matrix, C_{pm}, can be used to combine the dependent and independent parts of (3.1) through (C.11), as suggested in [168], to get the minimal form of equations of motion.

$$\widetilde{\mathbf{F}}_m - \widetilde{\mathbf{F}}^*_m \;=\; \mathbf{F}_m - \mathbf{F}^*_m + C^T_{pm}\,(\mathbf{F}_p - \mathbf{F}^*_p) = \mathbf{0} \tag{C.11}$$

where $\widetilde{F}$ and $\widetilde{F}^*$ are the reduced *generalized active forces* and *generalized inertia forces*, respectively.

The permutation matrix, E, is invoked to decompose (3.36) into dependent and independent parts.

$$(E^T\, M\, E)\,(E^T\, \ddot{\mathbf{q}}) + E^T\, \mathbf{b} \;=\; a_2\; E^T\, \mathbf{\Gamma} \tag{C.12}$$

Equation (C.12) can be written in a matrix form

$$\begin{bmatrix} M_{pp} & M_{pm} \\ M_{mp} & M_{mm} \end{bmatrix} \begin{bmatrix} \ddot{\mathbf{q}}_p \\ \ddot{\mathbf{q}}_m \end{bmatrix} + \begin{bmatrix} \mathbf{b}_p \\ \mathbf{b}_m \end{bmatrix} \;=\; a_2 \begin{bmatrix} \mathbf{\Gamma}_p \\ \mathbf{\Gamma}_m \end{bmatrix} \tag{C.13}$$

Separating (C.13) into the dependent and independent portions yields

$$\begin{aligned} \mathbf{0} \;&=\; \mathbf{F}_m - \mathbf{F}^*_m \;=\; a_2\; \mathbf{\Gamma_m} \;-\; M_{mm}\, \ddot{\mathbf{q}}_m \;-\; M_{mp}\, \ddot{\mathbf{q}}_p - \mathbf{b}_m \\ \mathbf{0} \;&=\; \mathbf{F_p} - \mathbf{F^*_p} \;=\; a_2\; \mathbf{\Gamma}_p \;-\; M_{pm}\, \ddot{\mathbf{q}}_m - M_{pp}\, \ddot{\mathbf{q}}_p - \mathbf{b}_p \end{aligned} \tag{C.14}$$

Plugging (C.14) into (C.11) gives the equations of motion in minimal form

$$\widetilde{M}_m\, \ddot{\mathbf{q}}_m + \widetilde{\mathbf{b}}_m \;=\; a_2\; \widetilde{\mathbf{\Gamma}}_m \tag{C.15}$$

where

$$\widetilde{M}_m \;=\; M_{mm} + M_{mp}\, C_{pm} + C^T_{pm}\, M_{pm} + C^T_{pm}\, M_{pp}\, C_{pm} \tag{C.16}$$

$$\widetilde{\mathbf{b}}_m \;=\; \mathbf{b}_m + C^T_{pm}\, \mathbf{b}_p + (M_{mm}\, \dot{C}_{pm} + C^T_{pm}\, M_{pp}\, \dot{C}_{pm})\, \dot{\mathbf{q}}_m \tag{C.17}$$

$$\widetilde{\mathbf{\Gamma}}_m \;=\; \mathbf{\Gamma}_m + C^T_{pm}\, \mathbf{\Gamma}_p \tag{C.18}$$

C.3.2 Reduced First Order Model

Here the equations of motion for the first order model, (3.26), recalled in order to show the procedure of reduction.

$$\frac{1}{\beta}\, \hat{\mathbf{\Gamma}} - D\, \dot{\mathbf{q}} \;=\; \mathbf{0} \tag{C.19}$$

the permutation matrix P related to constraint is invoked to decompose (C.19)) into the dependent and independent parts of it, yields

$$\frac{1}{\beta} P^T \hat{\mathbf{\Gamma}} - (P^T D P)(P^T \dot{\mathbf{q}}) = \mathbf{0}$$

$$\frac{1}{\beta} \begin{bmatrix} \hat{\mathbf{\Gamma}}_m \\ \hat{\mathbf{\Gamma}}_p \end{bmatrix} - \begin{bmatrix} D_{mm} & D_{mp} \\ D_{pm} & D_{pp} \end{bmatrix} \begin{bmatrix} \dot{\mathbf{q}}_m \\ \dot{\mathbf{q}}_p \end{bmatrix} = \mathbf{0} \tag{C.20}$$

From (C.20), the dependent and independent parts of generalized active forces corresponding to the Kane's method are obtained as

$$\begin{aligned} \mathbf{F}_m &= \frac{1}{\beta} \hat{\mathbf{\Gamma}}_m - D_{mm} \dot{\mathbf{q}}_m - D_{mp} \dot{\mathbf{q}}_p = \mathbf{0} \\ \mathbf{F}_p &= \frac{1}{\beta} \hat{\mathbf{\Gamma}}_p - D_{pm} \dot{\mathbf{q}}_m - D_{pp} \dot{\mathbf{q}}_p = \mathbf{0} \end{aligned} \tag{C.21}$$

wherein, the generalized inertia forces are omitted for the first order model. Equation (5.31) could be modified for the first order model by vanishing the inertial terms and plug in the constraint matrix, C_{pm},

$$\widetilde{\mathbf{F}}_m = \mathbf{F}_m + C_{pm}^T \mathbf{F}_p = \mathbf{0} \tag{C.22}$$

substitute (C.21) into (C.22) gives

$$\widetilde{D}_m \dot{\mathbf{q}}_m = \frac{1}{\beta} \widetilde{\mathbf{\Gamma}}_m \tag{C.23}$$

where

$$\begin{aligned} \widetilde{D}_m &= D_{mm} + D_{mp} C_{pm} + C_{pm}^T D_{pm} + C_{pm}^T D_{pp} C_{pm} \\ \widetilde{\mathbf{\Gamma}}_m &= \mathbf{\Gamma}_m + C_{pm}^T \mathbf{\Gamma}_p \end{aligned}$$

Appendix D

Kane's Method

This appendix discusses the derivation of equations of motion for a system of rigid multibody using Kane's method. Despite popularity of the classical methods like Newton-Euler, Lagrange, and Hamilton, but they are not efficient for dynamic modeling of complicated and large multibody systems. Therefore, computationally efficient and computer-oriented methods like Kane has been developed in order to address the drawbacks of the classical methods.

D.1 Partial Velocities

The key concept underlying Kane's method is the use of partial velocities, including linear (translational) and angular versions, described below in details. Lets consider n time-varying translational and angular coordinates, $q_r(r = 1, \cdots, n)$, called *generalized coordinates* for describing configuration, positions and orientations, of rigid bodies. Time derivatives of these generalized coordinates, called *generalized speeds* can be formulated as below

$$u_r = \sum_{s=1}^{n} Y_{rs}\dot{q}_s + Z_r \qquad (r = 1, \cdots, n) \tag{D.1}$$

where Y_{rs} and Z_r are functions of q_1, q_2, ..., q_n, and time. Equations (D.1) are called *kinematical differential equations* which must yield unique solutions for $\dot{q}_1$, $\dot{q}_2$, ..., $\dot{q}_n$ as a function of u_1, u_2, ..., u_n [168].

Now, linear and angular velocities of a multibody systems can be described by these generalized speeds which has the form of

$$\begin{cases} \mathbf{v} = \sum_{s=1}^{n} \mathbf{v}_r u_r + \mathbf{v}_t \\ \boldsymbol{\omega} = \sum_{s=1}^{n} \boldsymbol{\omega}_r u_r + \boldsymbol{\omega}_t \end{cases} \tag{D.2}$$

where ω_r and $\mathbf{v}_r$ are r^{th} partial angular and linear velocities defined as

$$\begin{cases} \mathbf{v}_r = \sum_{s=1}^{n} \dfrac{\partial \mathbf{v}}{\partial \dot{q}_s} W_{sr} & (r = 1, \cdots, n) \\ \boldsymbol{\omega}_r = \sum_{s=1}^{n} \dfrac{\partial \boldsymbol{\omega}}{\partial \dot{q}_s} W_{sr} \end{cases} \tag{D.3}$$

where W_{sr} is defined by the inversion of (D.1),

$$\dot{q}_s = \sum_{r=1}^{n} W_{sr} u_r + X_s \qquad (s = 1, \cdots, n) \tag{D.4}$$

Principally, partial angular velocities should be calculated only for those rigid bodies subjected to torques or possessing inertia, while partial linear velocities are only needed for those points subjected to external forces or possessing mass.

D.2 Generalized Forces

In this section, expressions of generalized forces that play an important role in connection with dynamical equations of motion, namely, *generalized active forces* and *generalized inertia forces* will be formed. Generalized active force come to play whenever the particles of a system are subjected to the action of contact and/or distance forces. The quantities are formed by dot product of partial linear and angular velocities with forces, and torques, respectively. For a multibody system with p bodies and n degrees-of-freedom described by u_1, u_2, ..., u_n, there are n generalized active forces, F_1, F_2, ..., F_n defined

$$F_r = \sum_{i=1}^{p} \left(\mathbf{v}_r^i \cdot \mathbf{R}_i + \boldsymbol{\omega}_r^i \cdot \mathbf{T}_i \right) \qquad (r = 1, \cdots, n) \tag{D.5}$$

where $\mathbf{v}_r^i$ and $\boldsymbol{\omega}_r^i$ are respectively partial liner velocity of the center of mass and partial angular velocity of i^{th} rigid body in the system. $\mathbf{R}_i$ and $\mathbf{T}_i$ are the resultant forces and moments acting on and around the mass center of i^{th} rigid body, respectively.

Generalized inertia forces depend on both the motion and mass distribution of a system. These forces are formed by dot product of partial linear and angular velocities with mass-acceleration and the time derivative of angular momentum respectively as follow,

$$F_r^* = \sum_{i=1}^{p} \left(\mathbf{v}_r^i \cdot m_i \mathbf{a}_i + \boldsymbol{\omega}_r^i \cdot \dot{\mathbf{H}}_i \right) \qquad (r = 1, \cdots, n) \tag{D.6}$$

where m_i is the mass, and $\mathbf{a}_i$ is the acceleration of the mass center of i^{th} rigid body of the system. $\dot{\mathbf{H}}_i$ is the time derivative of the angular moment of i^{th} body about its center of mass defined as

$$\dot{\mathbf{H}}_i = I_i \boldsymbol{\omega}^i + \boldsymbol{\omega}^i \times I_i \boldsymbol{\omega}^i \tag{D.7}$$

where I_i is the moment of inertia of i^{th} body around its center of mass.

D.3 Formulation of Equations of Motion

Finally, it can be shown [168] that the equations of motion for a multibody system with n degrees-of-freedom is obtained by

$$F_r - F_r^* = 0 \qquad (r = 1, \cdots, n) \tag{D.8}$$

This method is developed from Newton's second law and Euler's equation using the Principle of Virtual Work and D'Alembert's Principle. For more details refer to [168].

Appendix E

Method of Multiple Scales

This appendix discusses the method of multiple scales (MMS) using singular perturbation [57].

E.1 Parameter Perturbation

Physical and engineering problems are usually represented by a differential equations $L(f, x, t) = 0$ subjected to boundary $B(f, t) = 0$ and/or initial $I(f, x) = 0$ conditions. Many of them involving a small parameter, ϵ, which in general cannot be solved exactly in the form of $f(x, t, \epsilon)$. However, the solution can be written as an asymptotic series in powers of ϵ as below

$$f(x, \epsilon) = \epsilon^0 f_0(x) + \epsilon^1 f_1(x) + \epsilon^2 f_2(x) + \cdots \tag{E.1}$$

where f_i is independent of ϵ and $f_0(x)$ is the solution of the problem for $\epsilon = 0$. Now in order to find $f_i(x)$, (E.1) is substituted into $L(f, x, \epsilon) = 0$, expanded for small ϵ, and then the coefficients of each power of ϵ are collected. Since these equations must hold for all values of ϵ and sequences of power of ϵ are linearly independent; therefore, each coefficients must be vanished.

E.1.1 Example

Let us consider a linear second order differential equation involving a small ϵ

$$\frac{d^2u}{dt^2} + \epsilon\frac{du}{dt} + u = 0 \tag{E.2}$$

To determine an improved approximation to the solution of (E.2), a perturbation expansion (straight forward expansion) is seek which has the form

$$u(t, \epsilon) = \epsilon^0 u_0(t) + \epsilon^1 u_1(t) + \epsilon^2 u_2(t) + \cdots \tag{E.3}$$

The first and second derivatives of (E.3) are obtained by differentiation as follow

$$\begin{aligned} \frac{du}{dt} &= \epsilon^0 \frac{du_0}{dt} + \epsilon^1 \frac{du_1}{dt} + \epsilon^2 \frac{du_2}{dt} + \cdots \\ \frac{d^2u}{dt^2} &= \epsilon^0 \frac{d^2u_0}{dt^2} + \epsilon^1 \frac{d^2u_1}{dt^2} + \epsilon^2 \frac{d^2u_2}{dt^2} + \cdots \end{aligned} \tag{E.4}$$

Substituting (E.3) and (E.4) into (E.2) yields

$$\begin{aligned} 0 = & \left(\frac{d^2u_0}{dt^2} + \epsilon^1 \frac{d^2u_1}{dt^2} + \epsilon^2 \frac{d^2u_2}{dt^2} + \cdots \right) + \\ & \epsilon \left(\frac{du_0}{dt} + \epsilon^1 \frac{du_1}{dt} + \epsilon^2 \frac{du_2}{dt} + \cdots \right) + \\ & \left(u_0(t) + \epsilon^1 u_1(t) + \epsilon^2 u_2(t) + \cdots \right) \end{aligned} \tag{E.5}$$

Arranging (E.5) in the order of increasing power of ϵ gives

$$\left(\frac{d^2u_0}{dt^2} + u_0 \right) + \epsilon^1 \left(\frac{d^2u_1}{dt^2} + \frac{du_0}{dt} + u_1 \right) + \epsilon^2 \left(\frac{d^2u_2}{dt} + \frac{du_1}{dt} + u_2 \right) + \cdots = 0 \tag{E.6}$$

Now by vanishing coefficients of each power of ϵ we have

$$\epsilon^0 : \quad \frac{d^2u_0}{dt^2} + u_0 = 0 \tag{E.7}$$

$$\epsilon^1 : \quad \frac{d^2u_1}{dt^2} + \frac{du_0}{dt} + u_1 = 0 \tag{E.8}$$

$$\epsilon^2 : \quad \frac{d^2u_2}{dt} + \frac{du_1}{dt} + u_2 = 0 \tag{E.9}$$

Solving (E.7) leads to $u_0 = a\cos(t+\phi)$, then substituting u_0 back into (E.8) yields

$$\frac{d^2u_1}{dt^2} + u_1 = a\sin(t+\phi) \rightarrow u_1 = b\cos(t+\phi) - \frac{a}{2} t\cos(t+\phi) \tag{E.10}$$

With u_1 known, one can solve (E.9) to find u_2 in a similar fashion. Finally, By substituting u_i where $i = 0, 1, 2, \cdots$ back into (E.3), the solution for $u(t, \epsilon)$ has the form of

$$u(t,\epsilon) = \epsilon^0 \left(a\cos(t+\phi) \right) + \epsilon^1 \left(b\cos(t+\phi) - \frac{a}{2} t\cos(t+\phi) \right) + \cdots \tag{E.11}$$

E.2 Singular Perturbation Expansion

In parameter perturbations, section E.1, the asymptotic expansion of the desired quantities, $f(t,\epsilon)$, can be developed in the general form of [57]

$$f(t,\epsilon) \sim \sum_{i=0}^{\infty} a_i(t)\delta_i(\epsilon) \qquad as \qquad \epsilon \to 0 \tag{E.12}$$

where t is scalar or vector variable independent of ϵ, the coefficients a_i are functions of t only, and $\delta_i(\epsilon)$ is the asymptotic sequence. This expansion, (E.12) is said to be *uniformly valid* if

$$\begin{cases} f(t,\epsilon) = \sum_{i=0}^{N-1} a_i(t)\delta_i(\epsilon) + R_N(t,\epsilon) \\ R_N(t,\epsilon) = O[\delta_N(\epsilon)] \qquad \text{for all x of interest} \end{cases} \tag{E.13}$$

Otherwise it is said to be *nonuniformly valid* and break down in regions called regions of nonuniformity. Some of the sources of nonuniformity are, infinite domain, small parameter multiplying the highest derivative, type change of a partial differential equation, and presence of singularities [57]. In the case of small parameter multiplying to the highest derivative, which is our interest in this dissertation, boundary and initial conditions cannot be satisfied by (E.12). The issue in the singular case is that the ratio of two consecutive terms a_i/a_{i-1} does not approach zero by increasing m; therefore, the series diverges and the truncation of the series, as an approximation, is not valid for all t.

The MMS has been developed in order to address this issue [57]. MMS suggests that $f(t,\epsilon)$ depends explicitly on t, ϵt, $\epsilon^2 t$, ..., as well as ϵ itself. Thus, in order to determine a valid truncation of expansion for all t up to $O(\epsilon^N)$, where N is a positive integer, the dependency of t on the $N+1$ different time scales T_0, T_1, ..., T_N, where

$$T_i = \epsilon^i \; t \qquad i = 0, \cdots, N \tag{E.14}$$

must be determined. In general $T_i < T_{i-1}$ and (E.13) can be written as

$$f(t,\epsilon) = \tilde{f}(T_0, T_1, \cdots, T_N, \epsilon) = \sum_{i=0}^{N-1} \epsilon^i f_i(T_0, T_1, \cdots, T_N) + O(\epsilon T_N) \tag{E.15}$$

Notice that the error, the last term, in (E.15) dictates that the expansion is valid for times up to $O(\epsilon^N)$, and beyond this time, other time scales must be added in order to keep expansion uniformly valid.

Substitution of (E.14) and (E.15) into a general ordinary differential equation causes the conversion of the ordinary one into partial differential equations using

$$\begin{cases} \dfrac{d}{dt} = \dfrac{\partial}{\partial T_0} + \epsilon \dfrac{\partial}{\partial T_1} + \epsilon^2 \dfrac{\partial}{\partial T_2} + \cdots \\ \\ \dfrac{d^2}{dt^2} = \displaystyle\sum_{i=0}^{N} \sum_{j=0}^{N} \epsilon^i \epsilon^j \frac{\partial^2}{\partial T_i \partial T_j} \end{cases} \tag{E.16}$$

Equating coefficients of like powers of ϵ yields a set of equations for determining f_0, f_1,...,f_N which contains arbitrary function of the time scales T_i. These functions are valid if

$$\frac{f_i}{f_{i-1}} < \infty \qquad \text{for all} \qquad T_0, T_1, \cdots, T_N$$

Equations (E.14) to (E.16) are a variation of MMS called many-variable version [57].

References

[1] A. Bowling and A. F. Palmer, "The small mass assumption applied to the multibody dynamics of motor proteins," vol. 42, no. 9, pp. 1218–1223, June 2009. [Online]. Available: http://www.jbiomech.com/issues

[2] A. Bowling, A. F. Palmer, and L. Wilhelm, "Contact and impact in the multibody dynamics of motor protein locomotion," *Langmuir*, vol. 25, no. 22, pp. 12 974–12 981, Nov. 2009. [Online]. Available: http://pubs.acs.org/toc/langd5/0/0

[3] A. Bowling and M. Haghshenas-Jaryani, "Spatial multibody dynamics of nanoscale motor protein locomotion," in *Proceedings of the 1st International Conference on Bionics and Biomechanics (ICABB)*, October 14-16 2010.

[4] M. Haghshenas-Jaryani and A. Bowling, "Spatial multibody dynamics of motor proteins," in *Proceedings of Multibody Dynamics 2011, An ECCOMAS Thematic Conference*, July 4-7 2011.

[5] ——, "Multiscale dynamic modeling of processive motor proteins," in *Proceedings of the IEEE International Conference Robotics and Biomimetics (ROBIO)*, December 7-11 2011, pp. 1403–1408.

[6] ——, "Multiscale dynamic modeling of flexibility in myosin v using a planar mechanical model," in *Proceedings of the IEEE International Conference Robotics and Biomimetics (ROBIO)*, December 11-14 2012, pp. 366–371.

[7] M. Haghshenas-Jaryani, J. Drake, N. Tran, A. Bowling, and S. Mohanty, "Multiscale modeling and simulation of a microbead in an optical trapping process," in *Proceedings of the ASME 2nd Global Congress on Nanoengineering for*

Medicine and Biology (NEMB2013), February 4-6 2013, pp. V001T05A003, 2 pages.

[8] M. Haghshenas-Jaryani and A. Bowling, "Multiscale dynamic modeling flexibility in myosin v," in *Proceedings of the ASME International Design Engineering Technical Conferences (IDETC) and Computers and Information in Engineering Conference (CIE)*, August 4-6 2013, pp. V07AT10A008, 9 pages.

[9] ——, "Modeling flexibility in myosin v using a multiscale articulated multi-rigid body approach," *ASME Journal of Computational and Nonlinear Dynamics*, 2014, in press.

[10] M. Haghshenas-Jaryani, B. Black, S. Ghaffari, J. Drake, A. Bowling, and S. Mohanty, "Dynamics of microscopic objects in optical tweezers: Experimental determination of underdamped regime and numerical simulation using multiscale analysis," *Nonlinear Dynamics*, pp. 1–18, 2014, in press.

[11] T. Korten, A. Mansson, and S. Diez, "Towards the application of cytoskeletal motor proteins in molecular detection and diagnostic devices," *Current opinion in biotechnology*, vol. 21, no. 4, pp. 477–488, Aug 2010.

[12] C. Montemagno and G. Bachand, "Constructing nanomechanical devices powered by biomolecular motors," p. 225, 1999. [Online]. Available: http://stacks.iop.org/0957-4484/10/i=3/a=301

[13] Y. Hiratsuka and S. Takeuchi, "Towards a microrotary motor driven by motor proteins," in *Micro Electro Mechanical Systems, 2007. MEMS. IEEE 20th International Conference on*, 2007, pp. 695–698.

[14] A. Mansson, M. Sundberg, R. Bunk, M. Balaz, I. A. Nicholls, P. Omling, J. O. Tegenfeldt, S. Tagerud, and L. Montelius, "Actin-based molecular motors for cargo transportation in nanotechnology potentials and challenges," *Advanced Packaging, IEEE Transactions on*, vol. 28, no. 4, pp. 547–555, 2005.

[15] R. D. Vale and R. R. Milligan, "The way things move: Looking under the hood of molecular motor proteins," *Science*, vol. 288, no. 5463, pp. 88–95, April 2000.

[16] A. Agarwal and H. Hess, "Biomolecular motors at the intersection of nanotechnology and polymer science," *Progress in Polymer Science*, vol. 35, no. 1-2, pp. 252–277, 2 2010.

[17] E. Bagga, K. Kumari, L. M. Bharadwaj, and R. P. Bajpai, "Myosin motor-a future nanomachine," in *Intelligent Sensing and Information Processing, 2004. Proceedings of International Conference on*, 2004, pp. 227–232.

[18] A. Cavalcanti, L. Rosen, L. C. Kretly, M. Rosenfeld, and S. Einav, "Nanorobotic challenges in biomedical applications, design and control," in *Electronics, Circuits and Systems, 2004. ICECS 2004. Proceedings of the 2004 11th IEEE International Conference on*, 2004, pp. 447–450.

[19] A. Dubey, G. Sharma, C. Mavroidis, S. M. Tomassone, K. Nikitczuk, and M. L. Yarmush, "Dynamics and kinematics of viral protein linear nano-actuators for bio-nano robotic systems," in *Robotics and Automation, 2004. Proceedings. ICRA '04. 2004 IEEE International Conference on*, vol. 2, 2004, pp. 1628–1633 Vol.2.

[20] M. Hamdi, G. Sharma, A. Ferreira, and C. Mavroidis, "Molecular mechanics simulation of bio-nanorobotic components using force feedback," in *Robotics and Biomimetics (ROBIO). 2005 IEEE International Conference on*, 2005, pp. 105–110.

[21] S. Hiyama, Y. Moritani, T. Suda, T. Shima, and K. Sutoh, "An autonomous molecular transport system using dnas and motor proteins in molecular communication," in *Bio-Inspired Models of Network, Information and Computing Systems, 2007. Bionetics 2007. 2nd*, 2007, pp. 135–138.

[22] J. Huai-wei, W. Shi-gang, X. Wei, Z. Zhi-zhou, and H. Lin, "Construction of medical nanorobot," in *Robotics and Biomimetics (ROBIO). 2005 IEEE International Conference on*, 2005, pp. 151–154.

[23] J. R. D. et. al., "Molecular shuttles: directed motion of microtubules along nanoscale kinesin tracks," p. 232, 1999. [Online]. Available: http://stacks.iop.org/0957-4484/10/i=3/a=302

[24] M. A. Riegelman and J. R. Sellers, "Looped actin structures for testing processive molecular motors," in *Life Science Systems and Applications Workshop, 2006. IEEE/NLM*, 2006, pp. 1–2.

[25] A. A. G. Requicha, "Nanorobots, nems, and nanoassembly," *Proceedings of the IEEE*, vol. 91, no. 11, pp. 1922–1933, 2003.

[26] M. Shwetha, M. Suchitra, C. S. Vasavi, K. U. Radhagayathri, N. P. K. Krishnan, and D. Gopakumar, "Computational modeling and simulation of biomolecular motors," in *Advances in Computing, Control, and Telecommunication Technologies, 2009. ACT '09. International Conference on*, 2009, pp. 130–134.

[27] M. C. Tarhan, R. Yokokawa, L. Jalabert, D. Collard, and H. Fujita, "Biomotor-based nanotransport system constructed by pick-and-place assembly of individual molecules," in *Intelligent Robots and Systems (IROS), 2010 IEEE/RSJ International Conference on*, 2010, pp. 5628–5633.

[28] S. Tung and J. W. Kim, "Microscale hybrid devices powered by biological flagellar motors," *Automation Science and Engineering, IEEE Transactions on*, vol. 3, no. 3, pp. 260–263, 2006.

[29] S. K. Vashist, R. Tewari, I. Kaur, R. P. Bajpai, and L. M. Bharadwaj, "Smart-drug delivery system employing molecular motors," in *Intelligent Sensing and Information Processing, 2005. Proceedings of 2005 International Conference on*, 2005, pp. 441–446.

[30] A. G. Warrier, D. M. Barani, O. M. Deepak, N. P. K. Krishnan, S. S. Sujan, and G. L. SaiRam, "Biomolecular motor proteins as targets for cancer treatment-a computational study." in *Students' Technology Symposium (TechSym), 2010 IEEE*, 2010, pp. 17–20.

[31] R. Ballardini, V. Balzani, A. Credi, M. T. Gandolfi, and M. Venturi, "Artificial molecular-level machines: which energy to make them work?" *Accounts of Chemical Research*, vol. 34, no. 6, pp. 445–455, Jun 2001.

[32] V. V. Balzani, A. Credi, F. M. Raymo, and J. F. Stoddart, "Artificial molecular machines," *Angewandte Chemie (International ed.in English)*, vol. 39, no. 19, pp. 3348–3391, Oct 2 2000.

[33] T. Hugel and C. Lumme, "Bio-inspired novel design principles for artificial molecular motors," *Current opinion in biotechnology*, vol. 21, no. 5, pp. 683–689, 10 2010.

[34] S. M. Block, "Kinesin motor mechanics: Binding, stepping, tracking, gating, and limping," vol. 92, no. 9, pp. 2986–2995, May 2007.

[35] R. D. Vale, J. A. Spudich, and E. R. Griffis, "Dynamics of myosin, microtubules, and kinesin-6 at the cortex during cytokinesis in drosophila s2 cells," *Journal of Cell Biology*, vol. 186, no. 5, pp. 727–738, 2009.

[36] C. Veigel, F. Wang, M. L. Bartoo, J. R. Sellers, and J. E. Molloy, "The gated gait of the processive molecular motor, myosin v," *Nature Cell Biology*, vol. 4, no. 1, pp. 59–65, January 2002.

[37] G. Cappello, P. Pierobon, C. Symonds, L. Busoni, J. C. Gebhardt, M. Rief, and J. Prost, "Myosin v stepping mechanism," *Proceedings of the National Academy of Sciences of the United States of America*, vol. 104, no. 39, pp. 15 328–15 333, Sep 25 2007.

[38] D. Parker, Z. Bryant, and S. L. Delp, "Coarse-grained structural modeling of molecular motors using multibody dynamics," *Cellular and Molecular Bioengineering*, vol. 2, no. 3, pp. 366–374, September 2009.

[39] M. E. Fisher and A. B. Kolomeisky, "Simple mechanochemistry describes the dynamics of kinesin molecules." *Proceedings of the National Academy of Sciences of the United States of America*, vol. 98, no. 14, pp. 7748–7753, July 2001.

[40] A. B. Kolomeisky and M. E. Fisher, "Molecular motors: a theorist's perspective." *Annual Review of Physical Chemistry*, vol. 58, pp. 675–695, 2007.

[41] A. Ciudad, J. M. Sancho, and G. P. Tsironis, "Kinesin as an electrostatic machine," vol. 32, no. 5, pp. 455–463, November 2006.

[42] J. C. Chen and A. S. Kim, "Brownian dynamics, molecular dynamics, and monte carlo modeling of colloidal systems," *Advances in Colloid and Interface Science*, vol. 112, no. 1-3, pp. 159–173, December 2004.

[43] E. M. Craig and H. Linke, "Mechanochemical model for myosin v," *Proceedings of the National Academy of Sciences of the United States of America*, vol. 106, no. 43, pp. 18 261–18 266, 2009.

[44] H. Rafii-Tabar, Y. Jamali, and A. Lohrasebi, "Computational modelling of the stochastic dynamics of kinesin biomolecular motors," *Physica A*, vol. 381, pp. 239–254, July 2007.

[45] G. S. Ayton, W. G. Noid, and G. A. Voth, "Multiscale modeling of biomolecular systems: in serial and in parallel," *Current opinion in structural biology*, vol. 17, no. 2, pp. 192–198, Apr 2007.

[46] R. Chang, G. S. Ayton, and G. A. Voth, "Multiscale coupling of mesoscopic- and atomistic-level lipid bilayer simulations," *The Journal of chemical physics*, vol. 122, no. 24, p. 244716, Jun 22 2005.

[47] W. Zheng, "Multiscale modeling of structural dynamics underlying force generation and product release in actomyosin complex," *Proteins*, vol. 78, no. 3, pp. 638–660, Feb 15 2010.

[48] J. W. Chu, G. S. Ayton, S. Izvekov, and G. A. Voth, "Emerging methods for multiscale simulation of biomolecular systems," *Molecular Physics*, vol. 105, no. 2-3, pp. 167–175, 2007.

[49] M. Karplus and G. A. Petsko, "Molecular dynamics simulations in biology," *Nature*, vol. 347, no. 6294, pp. 631–639, 10/18 1990. [Online]. Available: http://dx.doi.org/10.1038/347631a0

[50] F. F. Abraham, J. Q. Broughton, N. Bernstein, and E. Kaxiras, "Spanning the continuum to quantum length scales in a dynamic simulation of brittle fracture," *EPL (Europhysics Letters)*, vol. 44, no. 6, p. 783, 1998. [Online]. Available: http://stacks.iop.org/0295-5075/44/i=6/a=783

[51] K. Anderson, M. Poursina, and K. D. Bhalerao, "On adaptive multiscale modeling of biomolecular systems with application in RNA," in *Proceedings of the Joint International Conference on Multibody System Dynamics*, Lappeenranta, Finland, May 2010.

[52] R. E. Rudd and J. Q. Broughton, "Coarse-grained molecular dynamics and the atomic limit of finite elements," *Phys. Rev. B*, vol. 58, no. 10, pp. R5893–R5896, Sep 1998.

[53] R. Miller and E. Tadmor, "The quasicontinuum method: Overview, applications and current directions," *Journal of Computer-Aided Materials Design*, vol. 9, pp. 203–239, 2002. [Online]. Available: http://dx.doi.org/10.1023/A:1026098010127

[54] S. P. Xiao and T. Belytschko, "A bridging domain method for coupling continua with molecular dynamics," *Computer Methods in Applied Mechanics and Engineering*, vol. 193, no. 17-20, pp. 1645–1669, 5/7 2004.

[55] R. M. Mukherjee, P. S. Crozier, S. J. Plimpton, and K. S. Anderson, "Substructured molecular dynamics using multibody dynamics algorithms," vol. 43, no. 10, pp. 1040–1055, December 2008.

[56] A. D. Schuyler and G. S. Chirikjian, "Efficient determination of low-frequency normal modes of large protein structures by cluster-nma," vol. 24, no. 1, pp. 46–58, May 2005.

[57] A. H. Nayfeh, *Perturbation Methods*. John Wiley & Sons, 1973.

[58] G. A. Pavliotis and A. M. Stuart, "Periodic homogenization for inertial particles," *Physica D: Nonlinear Phenomena*, vol. 2004, no. 3-4, pp. 161–187, May 2005.

[59] J. D. Coe, B. G. Levine, and T. J. Martinez, "Ab initio molecular dynamics of excited-state intramolecular proton transfer using multireference perturbation theory," vol. 111, no. 44, pp. 11 302–11 310, 2007.

[60] J. L. Mateos, "Walking on ratchets with two brownian motors," *Fluctuation and Noise Letters*, vol. 4, no. 1, pp. L161–L170, 2004.

[61] A. Aksimentiev, I. A. Balabin, R. H. Fillingame, and K. Schulten, "Insights into the molecular mechanism of rotation in the fo sector of atp synthase," *Biophysical journal*, vol. 86, no. 3, pp. 1332–1344, Mar 2004.

[62] P. J. Atzberger and C. S. Peskin, "A brownian dynamics model of kinesin in three dimensions incorporating the force-extension profile of the coiled-coil cargo tether," *Bulletin of mathematical biology*, vol. 68, no. 1, pp. 131–160, Jan 2006.

[63] R. H. Austin, "Nanoscale hydrodynamics in the cell: balancing motorized transport with diffusion," *HFSP journal*, vol. 2, no. 5, pp. 262–265, Oct 2008.

[64] E. M. Aydt, G. Wolff, and I. Morano, "Molecular modeling of the myosin-s1(a1) isoform," *Journal of structural biology*, vol. 159, no. 1, pp. 158–163, Jul 2007.

[65] I. Ben-Ari, K. Boushaba, A. Matzavinos, and A. Roitershtein, "Stochastic analysis of the motion of dna nanomechanical bipeds," *Bulletin of mathematical biology*, Nov 9 2010.

[66] D. R. Bevan, J. F. Garst, C. K. Osborne, and A. M. Sims, "Application of molecular modeling to analysis of inhibition of kinesin motor proteins of the bimc subfamily by monastrol and related compounds," *Chemistry and biodiversity*, vol. 2, no. 11, pp. 1525–1532, Nov 2005.

[67] V. Bierbaum and R. Lipowsky, "Chemomechanical coupling and motor cycles of myosin v," *Biophysical journal*, vol. 100, no. 7, pp. 1747–1755, Apr 6 2011.

[68] R. A. Bockmann and H. Grubmuller, "Nanoseconds molecular dynamics simulation of primary mechanical energy transfer steps in f1-atp synthase," *Nature structural biology*, vol. 9, no. 3, pp. 198–202, Mar 2002.

[69] S. Bouzat and F. Falo, "The influence of direct motor-motor interaction in models for cargo transport by a single team of motors," *Physical biology*, vol. 7, no. 4, p. 046009, Nov 22 2010.

[70] C. Bustamante, D. Keller, and G. Oster, "The physics of molecular motors," *Accounts of Chemical Research*, vol. 34, no. 6, pp. 412–420, Jun 2001.

[71] N. J. Cordova, B. Ermentrout, and G. F. Oster, "Dynamics of single-motor molecules: the thermal ratchet model," *Proceedings of the National Academy of Sciences of the United States of America*, vol. 89, no. 1, pp. 339–343, Jan 1 1992.

[72] A. Cressman, Y. Togashi, A. S. Mikhailov, and R. Kapral, "Mesoscale modeling of molecular machines: cyclic dynamics and hydrodynamical fluctuations," *Physical review.E, Statistical, nonlinear, and soft matter physics*, vol. 77, no. 5 Pt 1, p. 050901, May 2008.

[73] E. N. Cytrynbaum, V. Rodionov, and A. Mogilner, "Computational model of dynein-dependent self-organization of microtubule asters," *Journal of cell science*, vol. 117, no. Pt 8, pp. 1381–1397, Mar 15 2004.

[74] I. Derenyi and T. Vicsek, "The kinesin walk: A dynamic model with elastically coupled heads," *Proceedings of the National Academy of Sciences of the United States of America*, vol. 93, pp. 6775–79, Juner 1996.

[75] R. E. L. DeVille and E. Vanden-Eijnden, "Regular gaits and optimal velocities for motor proteins," *Biophysical Journal*, vol. 95, no. 6, pp. 2681–91, September 2008.

[76] T. Duke and S. Leibler, "Motor protein mechanics: a stochastic model with minimal mechanochemical coupling," *Biophysical journal*, vol. 71, no. 3, pp. 1235–1247, Sep 1996.

[77] E. Eisenberg and T. L. Hill, "A cross-bridge model of muscle contraction," *Progress in biophysics and molecular biology*, vol. 33, no. 1, pp. 55–82, 1978.

[78] D. Fan, W. Zheng, R. Hou, F. Li, and Z. Wang, "Modeling motility of the kinesin dimer from molecular properties of individual monomers," *Biochemistry*, vol. 47, no. 16, pp. 4733–4742, Apr 22 2008.

[79] A. M. Ferreira and D. Bashford, "Model for proton transport coupled to protein conformational change: application to proton pumping in the bacteriorhodopsin photocycle," *Journal of the American Chemical Society*, vol. 128, no. 51, pp. 16 778–16 790, Dec 27 2006.

[80] J. Fricks, H. Wang, and T. C. Elston, "A numerical algorithm for investigating the role of the motor-cargo linkage in molecular motor-driven transport," *Journal of theoretical biology*, vol. 239, no. 1, pp. 33–48, Mar 7 2006.

[81] Y. Q. Gao, W. Yang, R. A. Marcus, and M. Karplus, "A model for the cooperative free energy transduction and kinetics of atp hydrolysis by f1-atpase," *Proceedings of the National Academy of Sciences of the United States of America*, vol. 100, no. 20, pp. 11 339–11 344, Sep 30 2003.

[82] M. K. Gardner, D. J. Odde, and K. Bloom, "Kinesin-8 molecular motors: putting the brakes on chromosome oscillations," *Trends in cell biology*, vol. 18, no. 7, pp. 307–310, Jul 2008.

[83] M. J. Greenberg and J. R. Moore, "The molecular basis of frictional loads in the in vitro motility assay with applications to the study of the loaded mechanochemistry of molecular motors," *Cytoskeleton (Hoboken, N.J.)*, vol. 67, no. 5, pp. 273–285, May 2010.

[84] W. O. Hancock and J. Howard, "Kinesin's processivity results from mechanical and chemical coordination between the atp hydrolysis cycles of the two motor domains," *Proceedings of the National Academy of Science*, vol. 96, no. 23, pp. 13 147–13 152, November 1999.

[85] A. Hendricks, B. Epureanu, and E. Meyhfer, "Mechanistic mathematical model of kinesin under time andspace fluctuating loads," *Nonlinear Dynamics*, vol. 53, no. 4, pp. 303–320, 2008.

[86] Y. Jamali, M. E. Foulaadvand, and H. Rafii-Tabar, "Computational modelling of the collective stochastic motion of kinesin nano motors," *Journal of Theoretical and Computational Nano Sciences*, vol. 7, pp. 146–152, 2010.

[87] F. Julicher, A. Ajdari, and J. Prost, "Modeling molecular motors," *Rev.Mod.Phys.*, vol. 69, no. 4, pp. 1269–1282, Oct 1997.

[88] F. Julicher and J. Prost, "Spontaneous oscillations of collective molecular motors," *Phys.Rev.Lett.*, vol. 78, no. 23, pp. 4510–4513, Jun 1997.

[89] M. Karplus and J. A. McCammon, "Molecular dynamics simulations of biomolecules," *Nature structural biology*, vol. 9, no. 9, pp. 646–652, Sep 2002.

[90] D. N. Kim, C. T. Nguyen, and M. Bathe, "Conformational dynamics of supramolecular protein assemblies," *Journal of structural biology*, vol. 173, no. 2, pp. 261–270, Feb 2011.

[91] T. Kim, M. T. Kao, E. F. Hasselbrink, and E. Meyhofer, "Nanomechanical model of microtubule translocation in the presence of electric fields," *Biophysical journal*, vol. 94, no. 10, pp. 3880–3892, May 15 2008.

[92] A. B. Kolomeisky and M. E. Fisher, "A simple kinetic model describes the processivity of myosin-v," *Biophysical Journal*, vol. 84, pp. 1642–1650, March 2003.

[93] C. B. Korn, S. Klumpp, R. Lipowsky, and U. S. Schwarz1, "Stochastic simulations of cargo transport by processive molecular motors." *The Journal OF Chemical Physics*, vol. 131, no. 24, p. 245107, 2009.

[94] A. V. Kuznetsov, A. A. Avramenko, and D. G. Blinov, "Numerical modeling of molecular-motor-assisted transport of adenoviral vectors in a spherical cell," *Computer methods in biomechanics and biomedical engineering*, vol. 11, no. 3, pp. 215–222, Jun 2008.

[95] G. Lan and S. X. Sun, "Dynamics of myosin-v processivity," *Biophysical Journal*, vol. 88, no. 2, pp. 999–1008, February 2005.

[96] ——, "Flexible light-chain and helical structure of f-actin explain the movement and step size of myosin-vi." *Biophysical Journal*, vol. 91, pp. 4002–4013, December 2006.

[97] S. Leibler and D. A. Huse, "Porters versus rowers: a unified stochastic model of motor proteins," *The Journal of cell biology*, vol. 121, no. 6, pp. 1357–1368, Jun 1993.

[98] C. T. Lin, E. Meyhofer, and K. Kurabayashi, "Predicting the stochastic guiding of kinesin-driven microtubules in microfabricated tracks: a statistical-mechanics-based modeling approach," *Physical review.E, Statistical, nonlinear, and soft matter physics*, vol. 81, no. 1 Pt 1, p. 011919, Jan 2010.

[99] R. Lipowsky and S. Liepelt, "Chemomechanical coupling of molecular motors: Thermodynamics, network representations, and balance conditions," *Journal of Statistical Physics*, vol. 130, no. 1, pp. 39–67, 2008.

[100] A. Lohrasebi, Y. Jamali, and H. Rafii-Tabar, "Modeling the effect of external electric field and current on the stochastic dynamics of atpase nano-biomolecular motors," *Physica A: Statistical Mechanics and its Applications*, vol. 387, pp. 5466–5476, September 2007.

[101] T. Masuda, "A simulation model of the conventional kinesin based on the driven-by-detachment mechanism," *Bio Systems*, vol. 97, no. 2, pp. 121–126, Aug 2009.

[102] F. E. Mullner, S. Syed, P. R. Selvin, and F. J. Sigworth, "Improved hidden markov models for molecular motors, part 1: basic theory," *Biophysical journal*, vol. 99, no. 11, pp. 3684–3695, Dec 1 2010.

[103] C. S. Peskin, G. M. Odell, and G. F. Oster, "Cellular motions and thermal fluctuations: the brownian ratchet," *Biophysical journal*, vol. 65, no. 1, pp. 316–324, Jul 1993.

[104] C. S. Peskin and G. Oster, "Coordinated hydrolysis explains the mechanical behavior of kinesin," *Biophysical journal*, vol. 68, no. 4 Suppl, pp. 202S–210S; discussion 210S–211S, Apr 1995.

[105] X. Ping, D. Shuo-Xing, and W. Peng-Ye, "A model for processivity of molecular motors," *Chinese Physics*, vol. 13, no. 9, pp. 1569–2863, September 2004.

[106] M. Rief, R. S. Rock, A. D. Mehta, M. S. Mooseker, R. E. Cheney, and J. A. Spudich, "Myosin-v stepping kinetics: A molecular model for processivity," *Proceedings of the National Academy of Sciences*, vol. 97, no. 17, pp. 9482–9486, August 15 2000.

[107] F. Reif, *Fundamentals of Statistical and Thermal Physics*. McGraw Hill New York, 1965.

[108] P. Reimann, "Brownian motors: noisy transport far from equilibrium," *Physics Reports*, vol. 361, no. 2-4, pp. 57–265, 4 2002.

[109] W. R. Schief and J. Howard, "Conformational changes during kinesin motility," *Current opinion in cell biology*, vol. 13, no. 1, pp. 19–28, Feb 2001.

[110] Q. Shao and Y. Q. Gao, "On the hand-over-hand mechanism of kinesin," *Proceedings of the National Academy of Sciences of the United States of America*, vol. 103, no. 21, pp. 8072–8077, May 23 2006.

[111] S. M. Simon, C. S. Peskin, and G. F. Oster, "What drives the translocation of proteins?" *Proceedings of the National Academy of Sciences*, vol. 89, no. 9, pp. 3770–3774, May 01 1992.

[112] M. P. Singh, R. Mallik, S. P. Gross, and C. C. Yu, "Monte carlo modeling of single-molecule cytoplasmic dynein," *Proceedings of the National Academy of Sciences of the United States of America*, vol. 102, no. 34, pp. 12 059–12 064, Aug 23 2005.

[113] K. I. Skau, R. B. Hoyle, and M. S. Turner, "A kinetic model describing the processivity of myosin-v." *Biophysical Journal*, vol. 91, pp. 2475–2489, 2006.

[114] D. Tsygankov and M. E. Fisher, "Kinetic models for mechanoenzymes: Structural aspects under large loads," *Journal of Chemistry Physics*, vol. 128, no. 1, p. 015102, January 2008.

[115] S. Walcott and D. M. Warshaw, "Modeling smooth muscle myosin's two heads: long-lived enzymatic roles and phosphorylation-dependent equilibria," *Biophysical journal*, vol. 99, no. 4, pp. 1129–1138, Aug 9 2010.

[116] H. Wang, "Mathematical theory of molecular motors and a new approach for uncovering motor mechanism," *IEE proceedings.Nanobiotechnology*, vol. 150, no. 3, pp. 127–133, Dec 2003.

[117] H. Wang and T. C. Elston, "Mathematical and computational methods for studying energy transduction in protein motors," *Journal of Statistical Physics*, vol. 128, no. 1-2, pp. 35–76, July 2007.

[118] Y. Wu, Y. Q. Gao, and M. Karplus, "A kinetic model of coordinated myosin v," *Biochemistry*, vol. 46, pp. 6318–6330, 2007.

[119] A. Vilfan, "Elastic lever-arm model for myosin v," *Biophysical Journal*, vol. 88, pp. 3792–3805, June 2005.

[120] ——, "Five models for myosin v," *Frontiers in Bioscience*, vol. 14, pp. 2269–2284, January 2009.

[121] J. Yu, T. Ha, and K. Schulten, "Structure-based model of the stepping motor of PcrA helicase," *Biophysical Journal*, vol. 91, no. 6, pp. 2097–2114, September 2006.

[122] H. Yu, L. Ma, Y. Yang, and Q. Cui, "Mechanochemical coupling in the myosin motor domain. ii. analysis of critical residues," *PLoS computational biology*, vol. 3, no. 2, p. e23, Feb 16 2007.

[123] ——, "Mechanochemical coupling in the myosin motor domain. i. insights from equilibrium active-site simulations," *PLoS computational biology*, vol. 3, no. 2, p. e21, Feb 9 2007.

[124] P. Xie, "Stepping behavior of two-headed kinesin motors," *Biochimica et Biophysica Acta (BBA) - Bioenergetics*, vol. 1777, no. 9, pp. 1195–1202, 9 2008.

[125] J. Xing, H. Wang, and G. Oster, "From continuum fokker-planck models to discrete kinetic models," *Biophysical journal*, vol. 89, no. 3, pp. 1551–1563, Sep 2005.

[126] J. Zhang, W. Li, J. Wang, M. Qin, L. Wu, Z. Yan, W. Xu, G. Zuo, and W. Wang, "Protein folding simulations: from coarse-grained model to all-atom model," *IUBMB life*, vol. 61, no. 6, pp. 627–643, Jun 2009.

[127] K. B. Zeldovich, J. F. Joanny, and J. Prost, "Motor proteins transporting cargos," *European Physical Journal E*, vol. 17, no. 2, pp. 155–163, June 2005.

[128] W. Zheng and S. Doniach, "A comparitive study of motor-protein motions by using a simple elastic-network model," *Proceedings of the National Academy of Sciences*, vol. 100, no. 23, pp. 13 253–13 258, November 2003.

[129] J. Gapinski, J. Szymanski, A. Wilk, J. Kohlbecher, A. Patkowski, and R. holyst, "Size and shape of micelles studied by means of sans, pcs, and fcs," *Langmuir*, vol. 26, no. 12, pp. 9304–9314, March 2010.

[130] J. Szymanski, A. Patkowski, A. Wilk, P. Garstecki, and R. Holyst, "Diffusion and viscosity in a crowded environment: from nano- to macroscale," *Physical Chemistry Letters B*, vol. 110, pp. 25 593–25 597, November 2006.

[131] S. T. Wereley and C. D. Meinhart, "Recent advances in micro-particle image velocimetry," *Annual Review of Fluid Mechanics*, vol. 42, pp. 557–576, 2010.

[132] I. G. Currie, *Foundamental Mechanics of Fluids*, 3rd ed. Accel developement, 2007.

[133] A. Ashkin, J. Dziedzic, J. Bjorkholm, and S. Chu, "Observation of a single-beam gradient force optical trap for dielectric particles," *Optics Letters*, vol. 11(5), p. 288, 1986.

[134] A. Ashkin, "Forces of a single-beam gradient laser trap on a dielectric sphere in the ray-optics regime," *Biophysics Journal*, vol. 61, pp. 569–582, February 1992.

[135] S. K. Mohanty, K. S. Mohanty, and M. W. Berns, "Manipulation of mammalian cells using a single-fiber optical microbeam," *Journal of Biomedical Optics*, vol. 13, no. 5, p. 054049, 2008.

[136] K. S. Mohanty, C. Liberale, S. Mohanty, and V. Degiorgio, "In depth fiber optic trapping of low-index microscopic objects," *Applied Physics Letters*, vol. 92, no. 15, p. 151113, 2008.

[137] S. K. Mohanty, A. Uppal, and P. K. Gupta, "Optofluidic stretching of RBCs using single optical tweezers," *Journal of Biophotonics*, vol. 1, no. 6, p. 522, 2008.

[138] J. Finer, R. Simmons, and J. Spudich, "Single myosin molecule mechanics: Piconoewton forces and nanometre steps," *Nature*, vol. 368(6467), pp. 113–119, 1994.

[139] K. Svoboda, C. Schmidt, B. Schnapp, and S. Block, "Direct observation of kinesin stepping by optical trapping interferometry," *Nature*, vol. 365(6448), pp. 721–727, 1993.

[140] R. Yasuda, H. Noji, J. K. Kinosita, and M. Yoshida, "F1-atpase is a highly efficient molecular motor that rotates with discrete 120-degree steps," *Cell*, vol. 93(7), pp. 1117–1124, 1998.

[141] Y. Harada, O. Ohara, A. Takatsuki, H. Itoh, N. Shimamoto, and K. Kinosita, "Direct observation of dna rotation during transcription by escherichia coli rna polymerase," *Nature*, vol. 409(6816), pp. 113–115, January 2001.

[142] S. Kasas, N. Thomson, B. Smith, H. Hansma, X. Zhu, M. Guthold, C. Bustamante, E. Kool, M. Kashlev, and P. Hansma, "Escherichia coli rna polymerase activity observed using atomic force microscopy," *Biochemistry*, vol. 36(3), pp. 461–468, January 1997.

[143] S. K. Mohanty, "Optically-actuated translational and rotational motion at the microscale for microfluidic manipulation and characterization," *Lab Chip*, vol. 12, pp. 3624–3636, January/February 2012.

[144] F. M. Fazal and S. M. Block, "Optical tweezers study life under tension," *Nat Photon*, vol. 5, no. 6, pp. 318–321, 2011. [Online]. Available: http://dx.doi.org/10.1038/nphoton.2011.100

[145] Q. Xing, F. Mao, L. Chai, and Q. Wang, "Numerical modeling and theoretical analysis of femtosecond laser tweezers," *Optics and Laser Technology*, vol. 36, no. 8, pp. 635 – 639, 2004.

[146] M. Padgett and R. Di Leonardo, "Holographic optical tweezers and their relevance to lab on chip devices," *Lab Chip*, vol. 11, pp. 1196–1205, 2011. [Online]. Available: http://dx.doi.org/10.1039/C0LC00526F

[147] Y. Cao, A. B. Stilgoe, L. Chen, T. A. Nieminen, and H. Rubinsztein-Dunlop, "Equilibrium orientations and positions of non-spherical particles in optical traps," *Opt. Express*, vol. 20, no. 12, pp. 12 987–12 996, Jun 2012. [Online]. Available: http://www.opticsexpress.org/abstract.cfm?URI=oe-20-12-12987

[148] E. M. Purcell, "Life at low reynolds number," *American Journal of Physics*, vol. 45, no. 1, pp. 3–11, January 1977.

[149] G. N. Stratopoulos, T. E. Dialynas, and G. P. Tsironis, "Directional newtonian motion and reversals of molecular motors," *Physics Letters A*, vol. 252, no. 3-4, pp. 151–156, February 1999.

[150] H. M. Chun, C. E. Padilla, D. N. Chin, M. Watanabe, V. I. Karlov, H. E. Alper, K. Soosaar, K. B. Blair, O. M. Becker, L. S. D. Caves, R. Nagle, D. N. Haney, and B. L. Farmer, "MBO(N)D: A multibody method for long-time molecular dynamics simulations," vol. 21, no. 3, pp. 159–184, February 2000.

[151] A. D. Schuyler and G. S. Chirikjian, "Normal mode analysis of proteins: A comparison of rigid cluster modes with c_α coarse graining," vol. 22, no. 3, pp. 183–193, May 2004.

[152] C. D. Schwieters and G. M. Clore, "A physical picture of atomic motions within the dickerson dna dodecamer in solution derived from joint ensemble refinement against nmr and large-angle x-ray scattering data," *Biochemistry*, vol. 46, no. 5, pp. 1152–1166, 2007.

[153] H. Flechsig and A. S. Mikhailov, "Tracing entire operation cycles of molecular motor hepatitis c virus helicase in structurally resolved dynamical simulations," *Proceedings of the National Academy of Sciences of the United States of America*, vol. 107, no. 49, pp. 20 875–20 880, December 2010.

[154] P. E. Nikravesh and I. S. Chung, "Application of euler parameters to the dynamic analysis of three dimensional constrained mechanical systems," *The Journal of Mech. Des.*, vol. 104, pp. 785–791, 1982.

[155] S. R. Vadali, "On the euler parameter constraint," *The Journal of Astronaut Science*, vol. 36, pp. 259–265, 1988.

[156] H. S. Morton, "Hamiltonian and lagrangian formulations of rigid body rotational dynamics based on euler parameters," *The Journal of Astronaut Science*, vol. 41, pp. 561–591, 1993.

[157] R. Cheney, M. O'Shea, J. Heuser, M. Coelho, J. Wolenski, E. Espreafico, P. Forscher, R. Larson, and M. Mooseker, "Brain myosin-v is a two-headed unconventional myosin with motor activity." *Cell*, vol. 75, no. 1, pp. 13–23, October 1993.

[158] M. Terrak, G. Rebowski, R. Lu, Z. Grabarek, and R. Dominguez, "Structure of the light chain-binding domain of myosin v." *Proceedings of the National Academy of Sciences of the United States of America*, vol. 102, no. 36, pp. 12 718–23, September 2005.

[159] J. C. K. Chou, "Quaternion kinematic and dynamic differential equations," *Robotics and Automation, IEEE Transactions on*, vol. 8, no. 1, p. 53, feb 1992.

[160] E. A. Coutsias and L. Romero, "The quaternions with applications to rigid body dynamics," Sandia National Laboratories, Tech. Rep., 2004.

[161] D. Andreis and E. S. Canuto, "Orbit dynamics and kinematics with full quaternions," in *American Control Conference, 2004. Proceedings of the 2004*, vol. 4, 30 2004-july 2 2004, p. 3660.

[162] J. R. Dooley and J. M. McCarthy, "Spatial rigid body dynamics using dual quaternion components," in *Robotics and Automation, 1991. Proceedings., 1991 IEEE International Conference on*, apr 1991, p. 90.

[163] B. Ravani and B. Roth, "Mappings of spatial kinematics," *ASME Journal of Transmissions, and Automation in Design*, vol. 106, 1984.

[164] W. R.A. and H. E.J., "Generalized coordinate partitioning for dimension reduction in analysis of constrained dynamic systems," *Journal of Mechanical Design*, vol. 104, no. 1, pp. 247–255, 1982.

[165] W. Blajer, W. Schiehlen, and W. Schirm, "A projective criterion to the coordinate partitioning method for multibody dynamics," *Archive of Applied*

Mechanics, vol. 64, pp. 86–98, 1994, 10.1007/BF00789100. [Online]. Available: http://dx.doi.org/10.1007/BF00789100

[166] R. P. Singh and P. W. Likins, "Singular value decomposition for constrained dynamical systems," *Journal of Applied Mechanics*, vol. 52, no. 4, pp. 943–948, 1985. [Online]. Available: http://link.aip.org/link/?AMJ/52/943/1

[167] R. B. Gillespie, V. Patoglu, I. I. Hussein, and E. R. Westervelt, "On-line symbolic constraint embedding for simulation of hybrid dynamical systems," *Multibody System Dynamics*, vol. 14, no. 3-4, pp. 387–417, Nov. 2005.

[168] T. R. Kane and D. A. Levinson, *Dynamics: Theory and Applications*, 1st ed. McGraw-Hill Book Company, 1985.

[169] O. A. Bauchau and A. Laulusa, "Review of Contemporary Approaches for Constraint Enforcement in Multibody Systems," *Journal of Computational and Nonlinear Dynamics*, vol. 3, no. 1, pp. 011 005+, 2008.

[170] A. Laulusa and O. A. Bauchau, "Review of Classical Approaches for Constraint Enforcement in Multibody Systems," *Journal of Computational and Nonlinear Dynamics*, vol. 3, no. 1, pp. 011 004+, 2008.

[171] M. Kleppmann, "Simulation of colliding constrained rigid bodies," University of Cambridge, Tech. Rep. 683, April 2007.

[172] J. G. de Jalón, J. Unda, A. Avello, and J. M. Jiménez, "Dynamic analysis of three-dimensional mechanisms in "natural" coordinates," *Journal of Mechanisms Transmissions and Automation in Design*, vol. 109, no. 4, pp. 460–465, 1987. [Online]. Available: http://link.aip.org/link/?JMT/109/460/1

[173] C. G. Liang and G. M. Lance, "A differentiable null space method for constrained dynamic analysis," *Journal of Mechanisms, Transmissions and Automation in Design*, vol. 109, pp. 405–411, 1987.

[174] F. A. Potra and J. Yen, "Implicit numerical integration for euler-lagrange equations via tangent space parametrization*," *Mechanics of Structures and Machines*, vol. 19, no. 1, pp. 77–98, 1991. [Online]. Available: http://www.tandfonline.com/doi/abs/10.1080/08905459108905138

[175] W. Blajer, "Elimination of constraint violation and accuracy aspects in numerical simulation of multibody systems," *Multibody System Dynamics*, vol. 7, pp. 265–284, 2002, 10.1023/A:1015285428885. [Online]. Available: http://dx.doi.org/10.1023/A:1015285428885

[176] A. F. Josep Mas, J. Cuadros, I. Juvells, and A. Carnicer, "Understanding optical trapping phenomenon: A simulation for undergraduates," *IEEE Transactions on Education*, vol. 54, pp. 133–140, February 2011.

[177] R. DiLeonardo, "The trap forces applet." [Online]. Available: http://glass.phys.uniroma1.it/dileonardo/

[178] PHET, "The physics education technology project: Optical tweezers and application." [Online]. Available: http://phet.colorado.edu/en/simulation/optical-tweezers

[179] U. Lei, C. Y. Yang, and K. C. Wu, "Viscous torque on a sphere under arbitrary rotation," *Applied Physics Letters*, vol. 89, no. 18, p. 181908, 2006. [Online]. Available: http://link.aip.org/link/?APL/89/181908/1

[180] J. H. Kim, G. W. Mulholland, and D. Y. H. Kukuck, S. R.and Pui, "Slip correction measurements of certified psl nanoparticles using a nanometer differential mobility analyzer (nano-dma) for knudsen number from 0.5 to 83." *Journal of Research of the National Institute of Standards and Technology*, vol. 110, no. 1, pp. 31–54, January/February 2005.

[181] R. C. Gauthier and A. Frangioudakis, "Theoretical investigation of the optical trapping properties of a micro-optic cubic glass structure," *Applied*

Optics, vol. 39, no. 18, pp. 3060–3070, Jun 2000. [Online]. Available: http://ao.osa.org/abstract.cfm?URI=ao-39-18-3060

[182] Y. Deng, J. Bechhoefer, and N. R. Forde, "Brownian motion in a modulated optical trap," *Journal of Optics A: Pure and Applied Optics*, vol. 9, pp. S256–S263, 2007.

[183] M. Praprotnik, L. D. Site, and K. Kremer, "Adaptive resolution molecular-dynamics simulation: Changing the degrees of freedom on the fly," *JOURNAL OF CHEMICAL PHYSICS*, vol. 123, no. 22, DEC 8 2005.

[184] M. Poursina, K. D. Bhalerao, S. C. Flores, K. S. Anderson, and A. Laederach, "Strategies for articulated multibody-based adaptive coarse grain simulation of rna," *Methods in enzymology*, vol. 487, pp. 73–98, 2011.

[185] M. Poursina and K. S. Anderson, "Efficient coarse-grained molecular simulations in the multibody dynamics scheme," *Multibody Dynamics*, vol. 28, pp. 147–172, 2013.

[186] ——, "Canonical ensemble simulation of biopolymers using a coarse-grained articulated generalized divide-and-conquer scheme," *Computer Physics Communications*, vol. 184, no. 3, pp. 652–660, 3 2013.

[187] N. Vaidehi, A. Jain, and W. A. Goddard, "Constant temperature constrained molecular dynamics: the newtoneuler inverse mass operator method," *The Journal of physical chemistry*, vol. 100, no. 25, pp. 10 508–10 517, 01/01; 2013/01 1996. [Online]. Available: http://dx.doi.org/10.1021/jp953043o

[188] A. Jain, N. Vaidehi, and G. Rodriguez, "A fast recursive algorithm for molecular dynamics simulation," *Journal of Computational Physics*, vol. 106, no. 2, pp. 258–268, 6 1993.

[189] R. Rossi, M. Isorce, S. Morin, J. Flocard, K. Arumugam, S. Crouzy, M. Vivaudou, and S. Redon, "Adaptive torsion-angle quasi-statics: a general simulation

method with applications to protein structure analysis and design," *Bioinformatics*, 2007.

[190] M. Haghshenas-Jaryani and A. Bowling, "A new switching strategy for addressing euler parameters in dynamic modeling and simulation of rigid multibody systems," *Multibody System Dynamics*, vol. 30, no. 2, pp. 185–197, August 2013. [Online]. Available: http://dx.doi.org/10.1007/s11044-012-9333-8

[191] ——, "A new numerical strategy for handling quaternions in dynamic modeling and simulation of rigid multibody systems," in *Proceedings of the 2nd Joint International Conference on Multibody System Dynamics (IMSD)*, May 29 - June 1 2012.

[192] C. Pratt and K. Cornely, *Essential Biochemistry*. John Wiley & Sons, 2004.

[193] K. Shiroguchi and K. Kinosita, "Myosin v walks by lever action and brownian motion," *Science*, vol. 316, no. 5828, pp. 1208–1212, May 2007.

[194] W. H. Mather and R. F. Fox, "Kinesin's biased stepping mechanism: Amplification of neck linker zippering," *Biophysical Journal*, vol. 91, no. 7, pp. 2416–2426, October 2006.

[195] Y. Jamali, A. Lohrasebi, and H. Rafii-Tabar, "Computational modelling of the stochastic dynamics of kinesin biomolecular motors," *Physica A: Statistical Mechanics and its Applications*, vol. 381, pp. 239–254, July 2007.

[196] M. Bier, "Processive motor protein as an overdamped brownian stepper," *Physical Review Letters*, vol. 91, no. 14, pp. 148 104–1–148 104–4, October 2003.

[197] ——, "Modelling processive motor proteins: Moving on two legs in the microscopic realm," *Contemporary Physics*, vol. 46, no. 1, pp. 41–51, January-February 2005.

[198] K. Hayashi and M. Takano, "Violation of the fluctuation-dissipation theorem in a protein system," *Biophysical Journal*, vol. 93, no. 3, pp. 895–901, August 2007.

[199] R. M. Bulatovic, "A note on the damped vibrating systems," *Theoretical Applied Mechanics*, vol. 33, no. 63, pp. 213–221, 2006.

[200] H. Sosa, E. J. G. Peterman, W. E. Moerner, and L. S. B. Goldstein, "Adp-induced rocking of the kinesin motor domain revealed by single-molecule fluorescence polarization microscopy," *Nature Structural Biology*, vol. 8, no. 6, pp. 540–544, June 2001.

[201] M. D. Yamada, S. Maruta, S. Yasuda, K. Kondo, H. Maeda, and T. Arata, "Conformational dynamics of loops l11 and l12 of kinesin as revealed by spin-labeling epr," *Biochemical and Biophysical Research Communications*, vol. 364, no. 3, pp. 620–626, December 2007.

[202] W. Hwang and M. J. Lang, "Mechanical design of translocating motor proteins," *Cell Biochemistry and Biophysics*, vol. 54, no. 1-3, pp. 11–22, July 2009.

[203] A. B. Asenjo and H. Sosa, "A mobile kinesin-head intermediate during the atp-waiting state," *Proceedings of the National Academy of Sciences of the United States of America*, vol. 106, no. 14, pp. 5657–5662, April 2009.

[204] R. D. Vale, "Myosin v motor proteins: marching stepwise towards a mechanism," *The Journal of cell biology*, vol. 163, no. 3, pp. 445–450, Nov 10 2003.

[205] T. J. Purcell, H. L. Sweeney, and J. A. Spudich, "A force-dependent state controls the coordination of processive myosin v," *Proc. Natl. Acad. Sci.*, vol. 102, no. 39, pp. 13 873–13 878, 2005.

[206] S. E. Rice, T. J. Purcell, and J. A. Spudich, "Building and using optical traps to study properties of molecular motors," *Methods Enzymol.*, vol. 361, pp. 112–133, 2003.

[207] A. Yildiz, M. Tomishige, R. D. Vale, and P. R. Selvin, "Kinesin walks hand-over-hand," *Langmu*, vol. 20, no. 12, pp. 4892–4897, June 2004.

[208] A. R. Dunn and J. A. Spudich, "Dynamics of the unbound head during myosin v processive translocation," *Nature Structural & Molecular Biology*, vol. 14, no. 3, pp. 246–248, March 2007.

[209] J. Howard, "Motor proteins as nanomachines: The role of thermal fluctuations in generating force and motion," *12th Poincare Seminar*, pp. 33–44, January 2009.

[210] J. Liu, D. W. Taylor, E. B. Krementsova, K. M. Trybus, and K. A. Taylor, "Three-dimensional structure of the myosin v inhibited state by cryoelectron tomography," *Nature*, vol. 442, no. 13, pp. 208–211, July 2006.

[211] M. L. Walker, S. A. Burgess, J. R. Sellers, F. Wang, J. A. Hammer, J. Trinick, and P. J. Knight, "Two-headed binding of a processive myosin to f-actin," *Nature*, vol. 405, no. 6788, pp. 804–807, 06/15 2000. [Online]. Available: http://dx.doi.org/10.1038/35015592

[212] E. A. Coutsias, C. Seok, and K. A. Dill, "Using quaternions to calculate rmsd," *Journal of computational chemistry*, vol. 25, no. 15, pp. 1849–1857, Nov 30 2004.

[213] H. P. Fritzer, "Molecular symmetry with quaternions," *Spectrochimica Acta Part A: Molecular and Biomolecular Spectroscopy*, vol. 57, no. 10, pp. 1919–1930, 9/1 2001.

[214] R. M. Hanson, D. Kohler, and S. G. Braun, "Quaternion-based definition of protein secondary structure straightness and its relationship to ramachandran angles," *Proteins: Structure, Function, and Bioinformatics*, vol. 79, no. 7, pp. 2172–2180, 2011.

[215] C. F. F. Karney, "Quaternions in molecular modeling," *Journal of Molecular Graphics and Modelling*, vol. 25, no. 5, pp. 595–604, 1 2007.

[216] D. C. Rapaport, "Molecular dynamics simulation using quaternions," *Journal of Computational Physics*, vol. 60, no. 2, pp. 306–314, 9/15 1985.

[217] T. F. M. III, M. Eleftheriou, P. Pattnaik, A. Ndirango, D. Newns, and G. J. Martyna, "Symplectic quaternion scheme for biophysical molecular dynamics," *The Journal of chemical physics*, vol. 116, no. 20, pp. 8649–8659, 2002. [Online]. Available: http://link.aip.org/link/?JCP/116/8649/1

[218] P. Betsch, "On the use of euler parameters in multibody dynamics," *PAMM*, vol. 6, no. 1, pp. 85–86, 2006.

[219] R. Siebert and P. Betsch, "Numerical integration of rigid body dynamics in terms of quaternions," *PAMM*, vol. 8, no. 1, pp. 10 139–10 140, 2008.

[220] B. K. P. Horn, "Closed-form solution of absolute orientation using unit quaternions," *Journal of the Optical Society of America A*, vol. 4, no. 4, pp. 629–642, 1987.

[221] R. Shivarama and E. P. Fahrenthold, "Hamilton's equations with euler parameters for rigid body dynamics modeling," *Journal of Dynamic Systems, Measurement, and Control*, vol. 126, no. 1, pp. 124–130, 2004. [Online]. Available: http://link.aip.org/link/?JDS/126/124/1

[222] R. E. Roberson, "On the practical use of euler-rodrigues parameters in multibody system dynamic simulation," *Archive of Applied Mechanics*, vol. 55, no. 2, pp. 114–123, 1985, 10.1007/BF00536828. [Online]. Available: http://dx.doi.org/10.1007/BF00536828

[223] N. A. F. Senan and O. M. O'Reilly, "On the use of quaternions and euler rodrigues symmetric parameters with moments and moment potentials," *International Journal of Engineering Science*, vol. 47, no. 4, pp. 595–609, 4 2009.

[224] A. Perez and J. M. McCarthy, "Dual quaternion synthesis of constrained robotic systems," *Journal of Mechanical Design*, vol. 126, no. 3, pp. 425–435, 2004. [Online]. Available: http://link.aip.org/link/?JMD/126/425/1

[225] D. Han, Q. Wei, and Z. Li, "A dual-quaternion method for control of spatial rigid body," in *Networking, Sensing and Control, 2008. ICNSC 2008. IEEE International Conference on*, april 2008, p. 1.

[226] A. Ungut, G. Grehan, and G. Gouesbet, "Comparisons between geometrical optics and lorenz-mie theory," *Appl. Opt.*, vol. 20, no. 17, pp. 2911–2918, Sep 1981. [Online]. Available: http://ao.osa.org/abstract.cfm?URI=ao-20-17-2911

[227] M. Born and E. Wolf, *Principles of Optics*, 7th ed. Cambridge University Press, 1999.

[228] S. Mansfield and G. Kino, "Solid immersion microscope," *Applied Physics Letters*, vol. 57, pp. 2615–2616, 1990.

[229] G. Roosen, "Optical levitation of spheres," *Canadian Journal of Physics*, vol. 57, pp. 1260–1279, 1979.

[230] G. Roosen and C. Imbert, "Optical levitation by means of 2 horizontal laser beams: Theoretical and experimental study," *Physics Letters*, vol. 59A, pp. 6–8, 1976.

[231] A. Clemen, M. Vilfan, J. Jaud, J. Zhang, M. Barmann, and M. Rief, "Force-dependent stepping kinetics of myosin-v," vol. 88, pp. 4402–4410, June 2005.

[232] D. M. Warshaw, G. G. Kennedy, S. S. Work, E. B. Krementsova, and S. Beck, "Differential labeling of myosin v heads with quantum dots allows direct visualization of hand-over-hand processivity," *Biophysical Journal*, vol. 88, no. 5, pp. L30–L32, May 2005.

[233] F. J. Bueche, *Introduction to Physics for Scientists and Engineers*, 3rd ed. McGraw-Hill Book Company, 1979.

[234] Y. Levin, "Dynamics of myosin-v processivity," *Reports on Progress in Physics*, vol. 65, no. 11, pp. 1577–1632, November 2002.

[235] A. R. Hodges, E. B. Krementsova, and K. M. Trybus, "Engineering the processive run length of myosin v," *Journal of Biological Chemistry*, vol. 282, no. 37, pp. 27 192–27 197, September 2007.

Biographical Information

Mahdi Haghshenas-Jaryani was born in Tehran, Iran, in 1983. He received his B.S. degree from University of Tehran, Iran, in 2005, his M.S. degree from Sharif University of Technology, Iran, in 2009, and Ph.D. degree from The University of Texas at Arlington in 2014, respectively, all in Mechanical Engineering. His current research interest is in the area of computational modeling and simulation of mechanical and biomechanical systems. He is a member of ASME, IEEE, and APS societies.